OPERATIONAL LIGHTNING FORECASTING TECHNIQUE DEVELOPMENT AND TESTING UTILIZING C-BAND DUAL-POLARIMETRIC RADAR

by

CRYSTAL J. WOODARD

A THESIS

Submitted in partial fulfillment of the requirements
for the degree of Master of Science
in
The Department of Atmospheric Science
to
The School of Graduate Studies
of
The University of Alabama in Huntsville

HUNTSVILLE, ALABAMA

2011

UMI Number: 1507429

UMI

Dissertation Publishing

UMI 1507429

ProQuest®

ProQuest LLC.
789 East Eisenhower Parkway
P.O. Box 1346
Ann Arbor, MI 48106 - 1346

In presenting this thesis in partial fulfillment of the requirements for a master's degree from The University of Alabama in Huntsville, I agree that the Library of this University shall make it freely available for inspection. I further agree that permission for extensive copying for scholarly purposes may be granted by my advisor or, in his/her absence, by the Chair of the Department or the Dean of the School of Graduate Studies. It is also understood that due recognition shall be given to me and to The University of Alabama in Huntsville in any scholarly use which may be made of any material in this thesis.

_____   9/27/2011
(student signature)   (date)

THESIS APPROVAL FORM

Submitted by Crystal J. Woodard in partial fulfillment of the requirements for the degree of Master of Science in Atmospheric Science and accepted on behalf of the Faculty of the School of Graduate Studies by the thesis committee.

We, the undersigned members of the Graduate Faculty of The University of Alabama in Huntsville, certify that we have advised and/or supervised the candidate on the work described in this thesis. We further certify that we have reviewed the thesis manuscript and approve it in partial fulfillment of the requirements for the degree of Master of Science in Atmospheric Science.

Kevin Knapp   8/15/2011 Committee Chair
(Date)

_____

_____

_____

Sundar. A. C. _____ Department Chair

_____ College Dean

Rhonda Kay Gaede   12/5/11 Graduate Dean

ABSTRACT
The School of Graduate Studies
The University of Alabama in Huntsville

Degree <u>Master of Science</u>   College/Dept. <u>Science/Atmospheric Science</u>

Name of Candidate <u>   Crystal J. Woodard</u>

Title <u>Operational Lightning Forecasting Technique Development and Testing Utilizing</u>
<u>C-Band Dual-Polarimetric Radar</u>

Operational forecasting algorithms for lightning initiation have been well studied using radar reflectivity, but similar research has not been conducted using dual-polarimetric (DP) radar. To determine if DP observations improve lightning (cloud-to-ground and total lightning) initiation forecasting, a series of algorithms is developed and tested. A fuzzy-logic DP radar algorithm is used to identify the first instance of hydrometeors that are required for significant charging (e.g., graupel, hail or their antecedent particles such as supercooled raindrops). These tests also consider traditional reflectivity methods and Z_{DR} columns for the presence of supercooled drops. Based on an analysis of fifty ordinary convective cells, it is found that the use of DP variables can provide a small benefit of increased skill and/or lead time relative to the radar reflectivity benchmark, depending on the user's needs. More research is required to evaluate these small benefits relative to the increased cost in complexity.

Abstract Approval: Committee Chair   _Keith Knupp_

                          Department Chair   _Sundar. A.C._

                          Graduate Dean   _Rhonda Kay Gaede_

ACKNOWLEDGMENTS

TABLE OF CONTENTS

Page

LIST OF FIGURES

LIST OF TABLES

CHAPTER I

INTRODUCTION

Lightning is one of Earth's natural dangers, destructive not only to life but also

physical property. Every day approximately 50,000 thunderstorms occur across the globe

(Ahrens 2007). Of the continental United States, on average Florida has the highest

occurrence of thunderstorms with seventy to a hundred storm days per year (NWS

2011a). Kennedy Space Center (KSC), located in Cape Canaveral, FL, is particularly

aware of the common occurrence of thunderstorms to their geographical location (Weems

et al. 2001; Roeder et al. 2005). KSC space launch facilities are vulnerable to electrical

storms. A single lightning strike to a Space Shuttle prone on the launch pad laden with

fuel and equipment could cause numerous injuries and fatalities as well as damage

estimates of billions of dollars (Roeder et al. 2005). According to the National Weather

Service (NWS), there is currently an average of fifty-five lightning fatalities each year,

and over 300 related injuries (NWS 2011b). Over the past seventy years this number has

drastically improved from a peak of over 430 fatalities per year to less than thirty

lightning related deaths today (NWS 2011c). This may be due, in part, to better health

and medical practices; however, a large influence in this decrease is better awareness of

the dangers of lightning as well as improved thunderstorm warning capabilities. With

advanced warning of lightning initiation, both industry and civilian personnel will have

additional time to prepare and respond with safety measures. The ability to forecast

lightning is critical to both military and civilian operations for safety of personnel.

Many researchers have developed and tested different radar methods and tools of

first flash indications (e.g., Larson and Stansbury 1974; Marshall and Radhakant 1978;

Dye et al. 1986, 1988, 1989; Goodman et al. 1988; Buechler and Goodman 1990; Hondl

and Eilts 1994; Zipser and Lutz 1994; Jameson et al. 1996; Carey and Rutledge 1996,

2000; Roeder and Pinder 1998; Gremillion and Orville 1999; Vincent et al. 2003; Wolf

2006; Lund et al. 2009; Yang and King 2010; Mosier et al. 2011); nevertheless, few have

done so using dual-polarimetric radar variables and products on an operational basis.

Researchers have previously observed reflectivity and temperature thresholds (Reynolds

and Brooks 1956; Larson and Stansburty 1974; Dye et al. 1986, 1989; Buechler and

Goodman 1990; Michimoto 1991; Rutledge et al. 1992; Carey and Rutledge 1996, 2000;

Petersen et al. 1996, 1999; Roeder and Pinder 1998; Gremillion and Orville 1999;

Vincent et al. 2003; Wolf 2006; Yang and King 2010) plus derived features such as

vertically integrated ice (VII) (Carey and Rutledge 2000; D'Arcangelo 2000; Hoeth et al.

2011; Mosier et al. 2011). Most of these studies were conducted to study physical

processes and document correlations between radar and cloud electricity observations

leading to first flash. While these studies can, and have, led to the development of

forecasting methods, there has yet to be a study that compares the operational use of

polarimetric variables with that of basic radar variables for first flash forecasting. This

comparison is important in order to determine the exact advantages and disadvantages, if

there are any, of dual-polarimetric variables in first flash forecasting. For these reasons,

the research objective of this study is to improve algorithms for the short-term prediction

of lightning initiation through development and testing of operational techniques that rely on parameters observed and diagnosed using C-band dual-polarimetric radar.

NASA Marshall Spaceflight Center (MSFC) assisted in funding this research for the utilization of the newly installed C-band dual-polarimetric radar at Cape Canaveral Air Force Station (CCAFS) and KSC (Roeder et al. 2009, 2011). A NOAA Collaborative Science, Technology, and Applied Research (CSTAR) award, whose objective is to study lightning initiation forecasting using radar, provided additional support. The NWS, under NOAA, is currently in the process of converting the single polarized NEXRAD network, a network of 159 WSR-88D radars, to dual-polarimetric radars. This research could provide insight to the NWS on the usefulness of dual-polarimetric variables and first flash forecasting.

In support of their goals, the objective of this study is to improve lightning watch and warning performance for operational uses at locations such as NASA KSC, CCAFS, and NWS stations to enhance personnel safety and reduce costs. An improved operational forecasting technique would provide the NWS with a tool that could be used with confidence to warn local sports programs and other large outdoor venue public events about precise areas in danger of lightning. This would enable large events outdoor to then take safety measures for public safety.

CHAPTER II

BACKGROUND

The phenomenon lightning is rich in global history and research. The first

documented researcher of atmospheric electricity is Benjamin Franklin, who designed the

first lightning sensor. The first atmospheric electricity instrument was comprised of

two hollow metal half spheres and a metal ball as depicted in Figure 2.1. One sphere half

is supported by a rod that extends through the roof to be exposed to the environment

above Franklin's home. The other half sphere is elevated to the same level as the

suspended sphere by a rod extending from the floor of his home, effectively grounding

the sphere and rod. The metal ball is attached to a string and positioned between the

two half spheres, allowing it to swing freely between the sphere halves. This instrument

responds to the electrical fields produced by electrified clouds causing the metal ball to

transfer charges from one sphere half to the other, ringing out a warning of present

thunderclouds (McGorman and Rust 1998). Lightning detection has come a long way

since 1700. Today electric field sensors, such as electric field mills, are more accurate

and can record the strength of the field sensed. Such instruments are used as nowcasting

tools for the detection of an electric field associated with an electrically charged storm

(Murphy et al. 2008). The geographical coverage of these instruments has been thus far

constricted to areas accessible to operators and maintenance personnel. Recently, the

4

employment of satellites has allowed a global view of lightning activity even in the most

remote regions of South America and the ocean. An optical sensor, Geostationary

Lightning Mapper (GLM), equipped on Geostationary Operational Environmental

Satellite R-Series (Goes-R) is capable of detecting lightning from near-IR signatures

associated with total lightning activity (Goes-R 2011). Satellite infrared (IR)

observations are also being tested in algorithms for lightning initiation forecasting

(Mecikalski 2005) by associating cloud top properties indicative of convective

development with dynamics of charging accumulation. Studies of first flash forecasting

with radar algorithms will be discussed in the following sections.
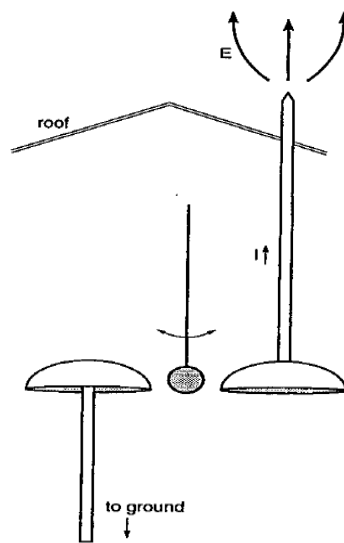
Figure 2.1   Diagram of Benjamin Franklin's atmospheric electricity warning system.
A bell and ball warning system for the detection of electrical fields
associated with atmospheric electricity of thunderstorms.
[Image credits to MacGorman and Rust (1998).]

To understand how to better predict the onset of lightning, we need to first

understand the physical nature of a thunderstorm leading up to the first discharge. How

does a cloud develop a violent bolt of energy, and what research has lead to our current

understanding and warning systems? Thus, the focus of this discussion will be on the

microphysical and dynamical process of electrification leading to first flash.
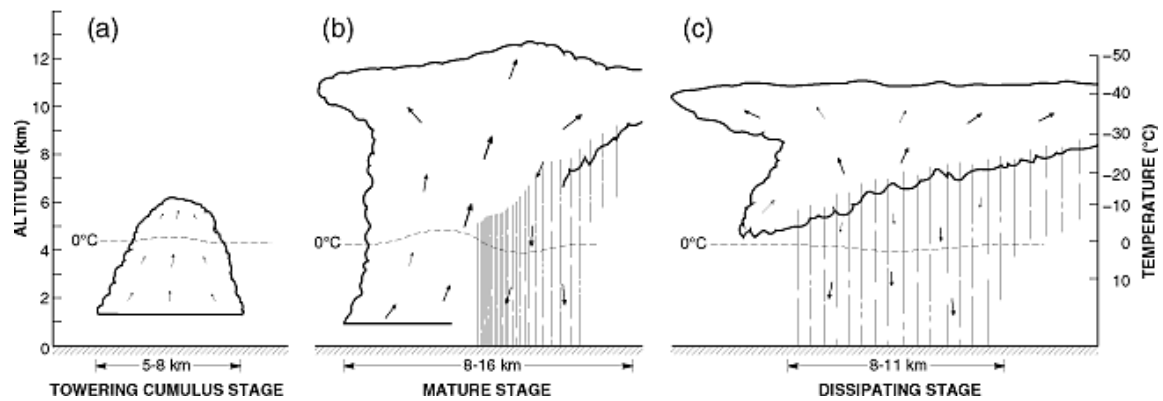
Figure 2.2   An idealized depiction of the three stages in the life cycle of an ordinary
single cellular thunderstorm, (a) cumulus or growth stage, (b) mature stage
and (c) dissipating stage. The vectors indicate the strength and general
direction of motion in the storm cell. An idealized altitude and
temperature profile of the storm is indicated on the Y-axis.
[Image credit to MacGorman and Rust, 1998, and Byers and Braham,
1949.]

2.1 Convective Development

Ordinary convective clouds, which evolve into thunderstorms develop and pass

through three stages of convection, growth, mature and dissipating as seen in Figure 2.2

(Byers and Braham 1949; MacGorman and Rust 1998; Wallace and Hobbs 2006). The

earliest growth stage (Figure 2.2a) in a storm's cellular life cycle is when the cell is

dominated by the production of an updraft. The second stage is the mature stage

(Figure 2.2b) when a cell develops a downdraft and significant precipitation in addition to

a vigorous updraft. The final stage is dissipation (Figure 2.2c), when a cell is no longer

supported by a strong updraft and the downdraft now dominates the dynamical and

microphysical processes of the cloud. This discussion will cover the stages of

development while focusing on the mature stage, the phase in which a cloud becomes significantly charged leading to first flash.

A convective cell can form by one of four general processes, thermal convection, forcing due to frontal boundaries, topographic lifting/forcing, surface convergence, or a mixture of the four previously stated (Houze 1993). Thermal convection occurs when a parcel of air heated by solar radiation to a thermal temperature that induces buoyancy is allowed to rise. Topographical forcing forms convection when a parcel of air is forced up a topographical feature, such as a mountain, forcing the air to condensate and creates a cloud. Cells in this data set are possibly formed and influenced by this method due to the mountainous nature of the region. Frontal boundary convection is another forcing mechanism that contributes to the formation of cells in this study. A frontal boundary could be the result of mesoscale features or due to local outflow boundaries produced by other cells. An outflow boundary of cool air produced by a large multicellular storm can persist for tens of kilometers, thus influencing the surrounding environment. Another form of forcing is from local surface convergence of air flow that causes an air parcel to rise. Two outflow boundaries converging may produce convection by a mixture of frontal boundary forcing and converging air. Large scale convection due to large environmental thermal boundaries, fronts, is referred to as "frontal" convection herein. Convection due to small scale boundaries, such as outflow boundaries, topographic forcing, and general thermal convection, herein is referred to as "local" convection. Ideally, the storms in this case are ordinary cells generally termed "pop-up" thunderstorms (Ahrens 2007) initiated by local convection. This form of convection is attributed to scattered thunderstorms of ordinary cells, which form uninfluenced by

frontal boundaries. Generally, ordinary convective cells are weak in comparison to supercellular and multicellular structures. The life cycle of an average single cellular storm is roughly thirty minutes (Byers and Braham 1948, 1949). The cells in this study are representative of this fact.

Once initial vertical motion is triggered and the parcel rises to a level where condensation begins, the release of latent heat into the parcel environment continues to support the vertical development of the storm (MacGorman and Rust 1998; Houze 1993). This process strengthens and aids in the continuous development of the updraft. The velocity of a well developed updraft is capable of lofting liquid condensation particles to levels above freezing while maintaining their liquid state. This provides the cloud with a supply of supercooled droplets that contribute to the production of hydrometeors such as rain, graupel and hail (Wallace and Hobbs 2006). Supercooled liquid is vital to the formation of graupel, a key ingredient in the process of electrification as discussed further on.

It is in the mature stage of the convective life cycle that a strong updraft, significant precipitation and a downdraft forms. Ice crystals play an important role in electrification and develop from the subsequent freezing of liquid droplets by homogenous and heterogeneous nucleation above the freezing level (Wallace and Hobbs 2008). Homogenous nucleation is the glaciation of pure water droplets, and heterogeneous nucleation is the freezing of droplets by interaction with environmental particles that serve as ice nuclei, such as clay. Ice hydrometeors called graupel form by riming, the contact freezing of supercooled drops on a snow or ice aggregate embryo. The formation of these hydrometeors, as well as rain, contributes to the formation of the

8

downdraft (MacGorman and Rust 1998; Houze 1993). The effects of gravity on the mass

of these growing particles overcome the resisting force of the updraft, and they descend.

Drier atmospheric air that is entrained, or the intake and mixing, evaporates some

precipitation thus cooling the air. The cooler air, less buoyant than the internal storm

environment, descends. The force of drag of the descending hydrometeors and the less

buoyant air develops into a downdraft, thus bringing the cell to full maturity. After the

formation of precipitation, there is an updraft and a downdraft during the mature phase of

convective development. This development is observable by radar. As represented in the

cross section image Figure 2.3c, higher reflectivity values observed by the radar are

indicative of the precipitation core. The formation of the downdraft can be observed in

the decent of the precipitation core, Figure 2.3d. The influence of precipitation loading

on downdraft development associated with lightning activity has been the reason for

many researchers, as conducted in this study, to observe radar signatures of the formation

of a precipitation core as first flash indicators.
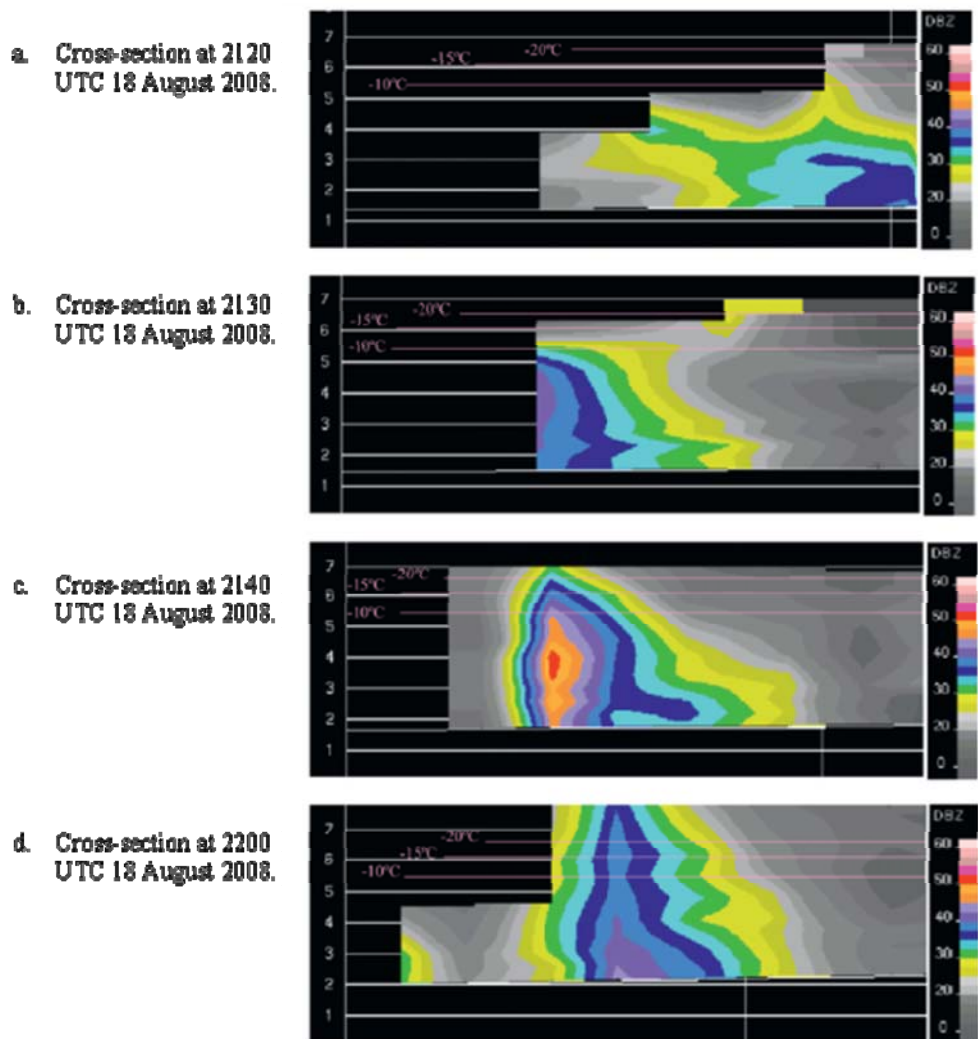
Figure 2.3   Radar reflectivity cross section of a developing convective cell. The thermal levels for -10, -15, and -20°C level are indicated. a) Radar cross section of a convective cell in the growth phase. b) Cross section of a cell nearing the mature phase. c) Cross section of a mature cell with a precipitation core and downdraft as indicated by high reflectivity values. d) Cross section after the decent of the precipitation core.
[Image credit to Yang and King, 2010.]

Furthermore, the structure of the mature cell and precipitation is also important to first flash forecasting. It is within the mixed phased region in which the previously stated hydrometeors develop and particle interactions lead to the generation and separation of electrical charge. This region, due to the mixture of hydrometeors that exist in both liquid and solid states, is termed the mixed phase region. The mixed phase region, as labeled mixed water and ice region in Figure 2.4, extends from the approximate location of the 0°C thermal to the -40°C thermal (MacGorman and Rust 1998; Houze 1993). This study focuses on the lower boundary of the mixed phase region ranging from -10°C to -20°C, a region also related to significant charging as addressed later. The upper range of the mixed phase region exists at -40°C where homogenous freezing occurs. Homogenous freezing is the subsequent freezing of any cloud particulate, meaning all liquid freezes at -40°C and below. The region between 0°C and below -10°C is typically a mixture of lofted liquid precipitation and freezing hydrometeors. The lower half of the mixed phase region is the focus of the following section.
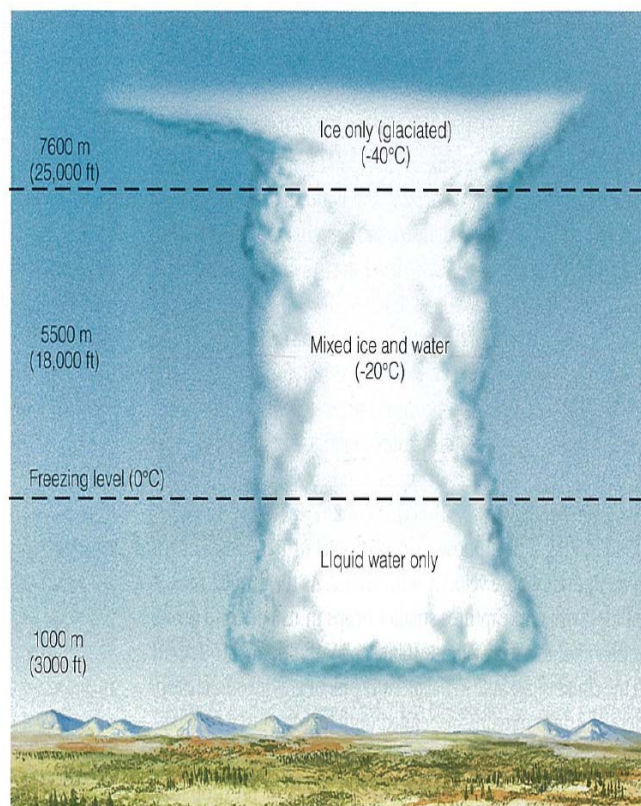
Figure 2.4   An idealized profile of a mature convective cell indicating the bulk
              precipitation phases at generalized thermal levels. At thermal
              temperatures above freezing, precipitation is ideally liquid only. In
              regions below freezing temperatures, water and ice exists together in the
              mixed phase region. All water phase hydrometeors freeze at temperatures
              below -40°C, thus this region is dominated by ice forms only.
              [Image credit to Ahrens, 2007.]

In conclusion, the dissipation stage of the convective lifecycle is when the updraft is no longer supported due to environmental conditions or the dominance of the downdraft. When the updraft subsides, it reduces the storm cell's supply of moisture and consequently latent heat energy. The lack of these two ingredients critically reduces the growth process of the cell. It should be noted that even in this stage, the remaining cloud is still potentially electrified (MacGorman and Rust 1998), and is still a threat to operations (Roeder et al. 2005).

2.2 Charging

Previous studies (Elster and Geitel 1888; Reynolds et al. 1957; Saunders 1993) have found that there are two possible charging mechanisms leading to charge accumulation in a cumulus cloud, inductive and non-inductive. Of these two concepts, there are several mechanisms of charging theorized to contribute to the electrification process of a thunderstorm, such as particle-to-particle interactions or ion capture. In the inductive method, charging mechanisms occur under the influence of an electric field. Studies (Latham and Mason 1962; Jennings 1975) show that inductive charging does not occur on a scale capable of supporting the verified measurable charges of a mature thunderstorm. The most widely accepted theory of charging leading to sufficient charge accumulation that is supported by laboratory, modeling, and in situ studies (Workman and Reynolds 1949; Reynolds et al. 1957; Church 1966; Takahashi 1978; Dye et al. 1986, 1988, 1992; Goodman et al. 1988; Keith and Saunders 1990; Saunders et al. 1991; Rutledge and Petersen 1994; Carey and Rutledge 1996, 2000) is the non-inductive particle-to-particle charging mechanism, commonly referred to as the NIC mechanism.

This process is not reliant on the induction or polarization of particles due to an environmental electric field. Instead, this process relies on the physical processes that exist within the cloud. There are two steps to this process, charge separation at the precipitation scale and charge separation on the scale of the storm.

Charging by the NIC mechanism on the precipitation scale occurs when two hydrometeors collide and a charge is transferred from one particle to the other. The transfer creates a positively charged particle and a negatively charged particle. Ideally, particle-to-particle charging occurs between graupel and ice crystals in the presence of supercooled water. This process is depicted in Figure 2.5, in which the interactions of two differently sized ice precipitants exchange charges. It is proposed that it is possible to occur between liquid and ice hydrometeors; however, graupel and ice collisions were proven more effective (Reynolds et al. 1957). Laboratory studies (Church 1966; Takahashi 1978; Jayaratne et al. 1983; Saunders et al 1991; Brooks and Saunders 1995) have found that the charge amount and sign is controlled by the liquid water content and temperature of the thunderstorm cloud environment. The charge exchanged was found by Church (1966) to reverse depending on the environmental temperature; higher temperatures resulted in a positively charged graupel and negatively for lower temperatures. Takahashi (1978) added to this research with his findings of the influence of liquid water on charge reversal for temperatures below -10°C. Saunders et al. (1991) and Brooks and Saunders (1995) found that the difference in liquid water concentrations (LWC) present in the local environment of the particle interactions is also a determination for the charge exchanged. A relatively large amount of LWC leads to a general positively charged graupel. Reversely, at lower LWC graupel is generally found

to contain a negative charge. For this reason, liquid water content of the cloud plays a

vital role in the charging process.
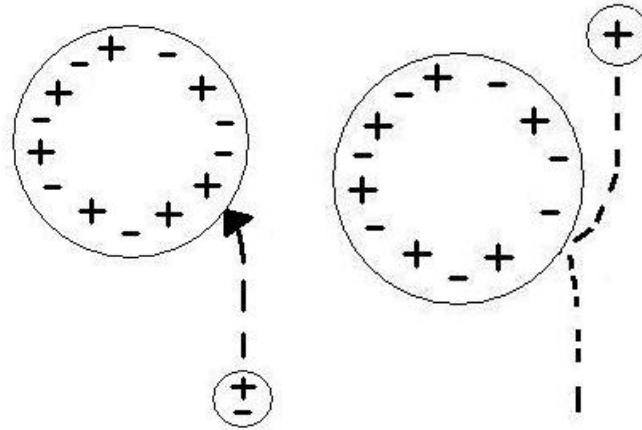
Figure 2.5   Example of negative non-inductive charging mechanism between
               two hydrometeors, such as graupel and ice crystal. The two particles
               collide momentarily exchanging a charge, then separate carrying opposite
               charges.

The second stage of the NIC process occurs on the storm scale. The

two oppositely charged hydrometeors continue to separate vertically to form the tripole

structure of the thunderstorm. This process occurs by way of one of three mechanisms,

sedimentation by the force of gravity acting on both particles, convection of the updraft,

and a combination of the two (MacGorman and Rust 1998). The first process,

sedimentation, occurs when the particles falling by the force of gravity reach terminal

velocity. Terminal velocity is different for each particle depending on their density, size,

and shape as affected by drag and gravity. This determines the difference in fall speeds

between a large graupel particle and a small ice crystal.   The second process involving

the influence of the updraft lofting the particles is similar to that of gravity. A smaller,

less dense, ice crystal is likely to be lofted with less drag force than that of a large dense

graupel particle. The updraft lofts the smaller ice crystal while the force of gravity on the

15

graupel particle overcomes the updraft force causing the graupel particle to descend. These mechanisms lead to the charge separation of particles that creates the tripole charge structure of the thunderstorm. This study focuses on the detection of hydrometeors related to charging, such as graupel and small ice crystals, in the cloud and supercooled drops in support of the physical process of charging.

On the storm scale, the processes of charge separation lead to the formation of the tripole structure of the thunderstorm. This electrical structure of the thunderstorm has long been studied (Simpson and Scrase 1937; Simpson and Robinson 1941; Marshall and Rust 1991; Ziegler and MacGorman 1994) via airborne and ground instruments. This tripole structure is widely supported (Williams 1989; Marshall and Rust 1991; Ziegler and MacGorman 1994; Bringi et al. 1997; MacGorman and Rust 1998; etc.) theory of the charge structure of thunderstorms. This structure consists of a main positive charge center over a main negative charge center that exists over a smaller positive charge center (Marshall and Rust 1991; Ziegler and MacGorman 1994; MacGorman and Rust 1998), as shown in Figure 2.6. The upper main positive charge center is created by the lofting of the positively charged ice crystals, while the negative charge region is developed by the falling negatively charged graupel. In agreement with the NIC method at temperatures $< -10°C$, graupel particles are predominately negatively charged. The lower positive charge region is created by the decent of positively charged precipitation and is occasionally not present in the charge structure of some storms (Marshall and Winn 1982; Marshall and Rust 1991). In accordance to the NIC mechanism, the lower positive charge region is also attributed to the presence of positively charged graupel particles as a result of charge reversal microphysics (Jayaratne et al. 1983). As previously noted, the

occurrence of CG lightning is well correlated with the decent of the precipitation core. This is related to sedimentation of negatively charged graupel, which charge positively in the presence of greater temperatures and LWC and subsequently switch sign, aiding in the development of the lower positive charge region. The approximate region of the main negative charge, between -10 and -20°C is the main charging region (Workman and Reynolds 1949; Krehbiel et al. 1979; Dye et al. 1986, 1988; William 1989; MacGorman and Rust 1998; Carey and Rutledge 2000; Wallace and Hobbs 2006), a key focus in this study. This is consistent with the location of CG lightning initiation, which for a negative lightning flash, extends from the approximate location of the main negative charge center to the ground (Wallace and Hobbs 2006). The process of a lighting stroke will be discussed in the next section. The tripole structure is important for the building of an electric field difference in the atmosphere that is capable of breaking down the surrounding atmosphere thus leading to a lighting flash.
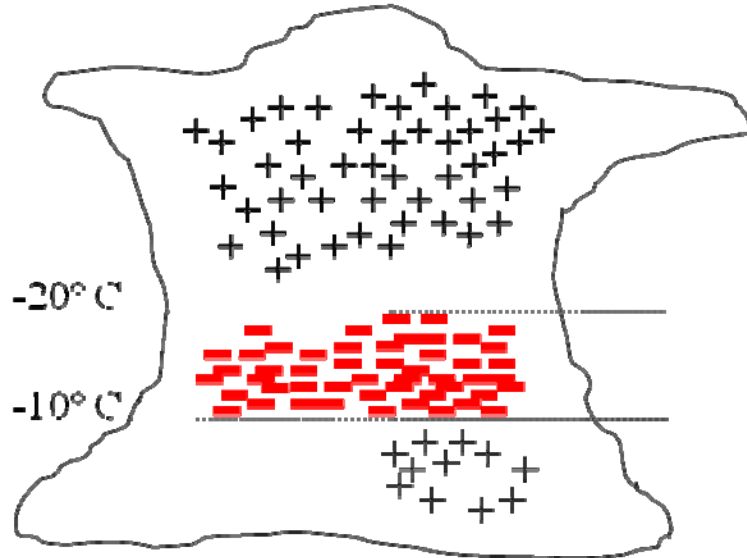
Figure 2.6   The idealized tripole structure of a mature thunderstorm consists of a lower positive charge existing at levels below -10°C, a main negative charge extending from approximately -10 to -20°C and the upper region of the cloud hosts the upper main positive charge which extends from -20°C and above. The region roughly between -10 and -20°C is the approximate location of the main processes of charging.

The approximate location of these charge centers are typically located at an altitude of four kilometers, or around 0°C, for the lower positive charge, four to ten kilometers, about -10 to -20°C, for the main negative charge and eight to sixteen kilometers, approximately -20°C and lower, for the main positive charge (MacGorman and Rust 1998; Wallace and Hobbs 2006). Figure 2.6 is an idealized depiction of the thunderstorm tripole; however it can be more complex than that. The electrical structure of a cloud can contain multiple charge layers at levels lower or higher than those idealized in the Figure 2.6, such as those shown in Figure 2.7 (Ziegler and MacGorman 1994).
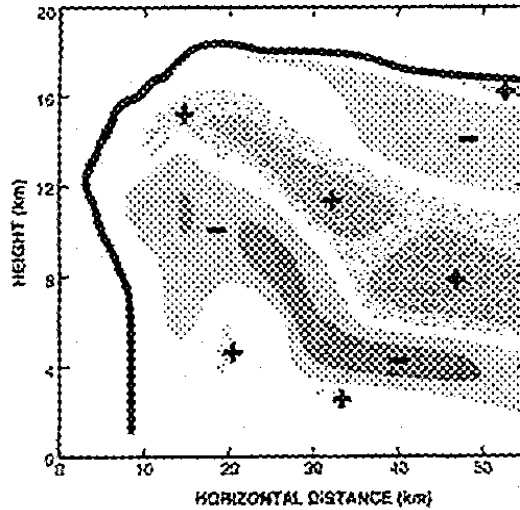
Figure 2.7   A more accurate idealization of the charge structure of a thunderstorm. The charge accumulations in a thunderstorm are not perfectly vertically separated. This image though still an idealization of the charge centers depicts the distribution of charge centers throughout the convective cell. [Image credits to Ziegler and MacGorman, 1994.]
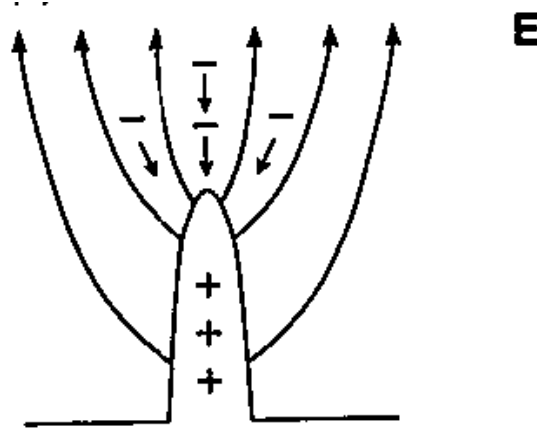
Figure 2.8   Positive corona is a positively charged point in an enhanced electric field that attracts positive ions which initiates an electron avalanche. This is the beginning of a streamer leading to the development of a flash of lightning.
[Image credit to McGorman and Rust, 1998.]

2.3 Flash

Charge accumulation in the tripole structure leads to the formation of a flash of lightning. A lightning flash is comprised of a series of pulsed strokes of energy through an electric channel. This channel forms in the atmosphere through a process that breaks down the atmosphere, altering its conductivity. This makes the atmosphere conducive to the transport of electric current. This section will discuss the processes that develop the initial flash and different flash types.

The first part of the lightning flash is the initial breakdown of the atmosphere that leads to the formation of the first stroke of lightning. This occurrence is assisted by a strong electric field, called the break down field, capable of turning the local environment of air from being an isolator into a conductor. It is theorized to exist in a localized region through the formation of an electron avalanche (MacGorman and Rust 1998). This electron avalanche is started by hydrometeors or pointed objects with positively charged pointed edges that then attract space charge ions. Figure 2.8 is an example of a positively charged point with an enhanced electric field leading to the attraction of ions. Space charge ions occur in the atmosphere due to natural radioactive decay, cosmic rays, and discharge from other electrical flashes. The electron avalanche starts with the attraction of a single space charge that rushes into the region of the charged point (MacGorman and Rust 1998). The object becomes electrically charged due to the presence of an electric field created by the buildup of charged particles in the cloud. When the space charge ion collides with another particle, if it is traveling at a velocity capable of breaking even, it will dislodge another ion. Breaking even is the term for the ability of the ion to collide with a particle in a way that it is capable of separation after collision (MacGorman and

Rust 1998). This process is made possible by the breakeven field, an electric field

enhanced by the pointed conductor capable of accelerating a particle to the velocity

needed to breakeven and then accelerating the ion again to this velocity. The electron

avalanche process occurs over and over again, each time doubling the amount of space

charges. This process soon develops an electric field capable of breaking down the

surrounding environment and developing the first electric streamer called corona. It is

also theorized that this process can occur without a charged point (MacGorman and Rust

1998). Instead the electric field between two charge regions and a space charge ion begin

the electron avalanche leading to the development of a streamer. The process of corona

is the beginning of a similar process that occurs over and over again as the electric

streamer progresses through the atmosphere photoionizing the atmosphere creating a

channel for lightning.
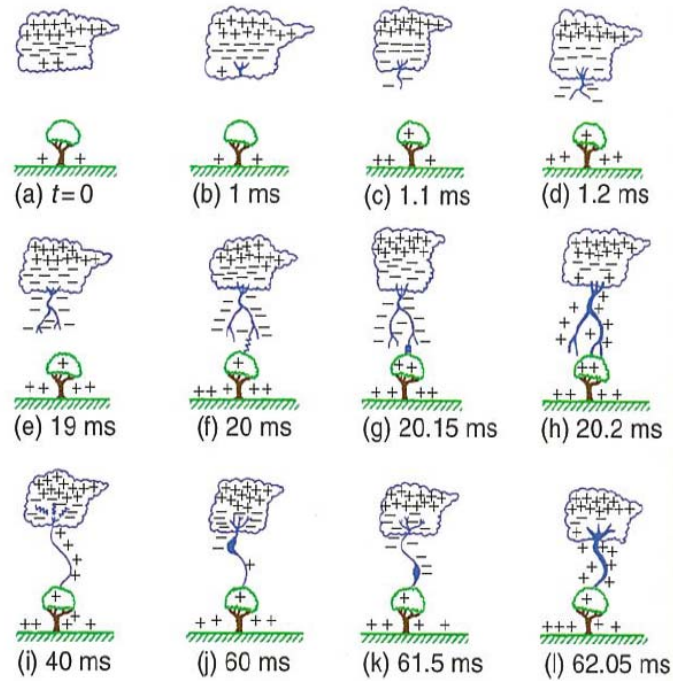
Figure 2.9   Evolution of a negative CG flash. Starting from top left: a) The tripole structure of the storm, b) The initial break down and discharge between the charge layers, c-e) The formation of the stepped leader, f) Corona streamer from the ground connects with the stepped leader, g) Negative charge current, h) First return stroke, i) K and j streamers, j-k) Formation of the dart leader, l) The second return stroke.
[Image credits to Wallace and Hobbs, 2006, and Uman, 1987.]

The electric field induced by the charge centers in the cloud assists the initial

discharge of a lighting flash. There are two main forms of lightning, intracloud (IC) and

cloud-to-ground (CG). IC lighting can occur within a single cloud, cloud to air, or

between two clouds. CG lighting can produce either a positive flash or negative flash,

depending on the charge of the initial stroke. A lightning flash occurs in several stages as

seen in Figure 2.9 (MacGorman and Rust 1998). The initial discharge in the cloud occurs

influenced by an electric field between the charge centers in the cloud. For a CG flash,

initial discharge is found to occur commonly between a lower positive charge region and

a negative charge region (Coleman et al. 2003).   This field then initiates the breakdown

of the atmosphere, allowing the air to conduct an electrical current. The initial streamer,

called a stepped leader, forges a channel from the cloud towards the ground. If the source

of the streamer originates from the negative charge center, then the flash is negative.

Corona, or point discharge, from the ground (positive for a negative flash) connects with

the stepped leader to form a complete electrical channel. This process is the slowest in

the formation of the first return stoke, occurring in about 20 ms. After connection

between the streamer from the cloud and corona from the ground, then negative charge

forges the formed channel. It is the subsequent return stroke of positive electrons that is

visible (MacGorman and Rust 1998). A lightning flash typically consists of about

three return strokes (Wallace and Hobbs 1998). After the initial return stroke, a dart

leader of negative ions (if supported by the charge in the cloud) flows through the

channel, cloud to ground, initiating a subsequent return stroke. This process will occur

repeatedly until the charge center from which the flash originated has been neutralized.

IC lightning occurs much like CG lighting, however instead of striking the ground, the

lightning is found to progress across the length of a single cloud or multiple clouds in a multicellular structure neutralizing pockets of charge.

Generally, IC flashes precede CG flashes (Williams et al. 1989; MacGorman 2011). It is important to be able to forecast the onset of both total lightning and CG to match the consumer's needs. CG forecasting is important because this is the most dangerous situation for the average consumer concerned about the effects of ground events such as sporting events or outdoor activities. These outdoor activities are the leading activities associated with lightning related fatalities (NWS 2011b). Other consumers, such as KSC/CCAFS who are concerned with flights of airplanes and space shuttle launches, would be concerned with forecasting total lightning. For these reasons, this study examines forecasting for both situations.

Lightning flashes are measured by very high frequency (VHF) detector networks and low frequency (LF) detector networks. Lightning flashes are not just detectable by light, but also by radio frequency. Lighting flashes radiate electromagnetic waves of low and very high frequencies in pulses as the electric field breaks down the atmosphere with the progression of each stroke. Each lightning flash contains multiple pulses, thus the use of LF and VHF instruments for the detection of lightning. The point source of the LF and VHF signal pulse is referred to as a "source" and is used in lightning detection and location. These instruments will be discussed in the following chapter.

The following section will discuss how the processes discussed up to now have been utilized for research. Some of the research methods to be discussed include the use of radar reflectivity to detect signatures of hydrometeors significant to charging in developing thunderstorms.

2.4 Previous Radar-based First Flash Forecasting and Observations

Lightning initiation has a rich research history; many studies (Larson and Stansburty 1974; Dye et al. 1986, 1988, 1989; Buechler and Goodman 1990; Michimoto 1991; Hondl and Eilts 1994; Bringi et al. 1990; Jameson et al. 1996; Petersen et al. 1996; Gremillion and Orville 1999; Carey and Rutledge 2000; Vincent et al. 2003;Wolf 2006; Yang and King 2010) have looked at the mechanics leading up to first flash based upon charging mechanisms and the microphysical processes of thunderstorms. These studies have used radar signatures and environmental profiles to study the dynamics and microphysics of thunderstorms leading up to first flash. Such research conducted has discovered the association of significant radar reflectivity signatures associated with first flash and charging mechanisms. These signatures include high values of horizontal radar reflectivity at significant thermal altitudes (Dye et al. 1986, 1989; Buechler and Goodman 1990; Zipser and Lutz 1994; Petersen et al. 1996; Roeder and Pinder 1998; Gremillion and Orville 1999; Vincent et al. 2003; Wolf 2006; Yang and King 2010), as well as the use of polarimetric radar parameters, such as differential reflectivity paired with horizontal reflectivity at significant thermal altitudes (Jameson et al. 1996; Carey and Rutledge 1996, 2000; Bringi et al. 1997; Lund et al. 2009). The research conducted in these areas will be discussed in further detail in this section.

 The use of horizontal radar reflectivity signatures at specific thermal levels continues to be a key focus in lightning initiation studies and forecasting. This method focuses on the detection of significant precipitation at temperature levels likely associated with charging by the NIC mechanism. High radar reflectivity values located at thermal

levels below freezing are indicative of the presence of large ice hydrometeors, such as

graupel and hail. This is due to the difference of the dielectric constant and the larger

particle size of these ice hydrometeors, as discussed in Chapter III. Most studies (Dye et

al. 1989; Buechler and Goodman 1990; Gremillion and Orville 1999; Vincent et al. 2003;

Wolf 2006; Yang and King 2010) found the 40 dBZ radar signature at approximately

-10°C to be the best indicator of the onset of electrification. These studies were

conducted at different geographical and climatological locations, such as Florida, New

Mexico, North Carolina, Ontario, etc. Other studies have found lower reflectivity values

and higher altitudes better associated to first flash and charging. Michimoto (1991) found

30 dBZ at -20°C, while Hondl and Eilts (1994) determined 10 dBZ near the freezing

level has the greatest advantage in forecasting the occurrence of thunderstorms.   Hondl

and Eitls concluded that this threshold is associated with a high false alarm, meaning that

many non-thunderstorms developed past this threshold value. Jameson et al. (1996)

found 40 dBZ at about -7°C was the best indicator leading to first flash. This threshold is

very close to the results of other studies previously stated. The most recent research

conducted by Mosier et al. (2011) found 30 dBZ at -15 to -20°C to hold the greatest

advantage in Houston. Petersen et al. (1996) found a correlation in lightning initiation

and 30 dBZ at -10°C or colder in oceanic convective storms. Furthermore, these studies

(Dye et al. 1989; Buechler and Goodman 1990; Gremillion and Orville 1999; Yang and

King 2010) found the vertical extent of the convective structure of the thunderstorm as

determined by radar must reach above 7 km at minimum for significant electrification to

occur. Significant radar reflectivity values indicate vertical development capable of

charge separation and the development of an updraft capable of supplying supercooled

drops and supporting particles necessary for electrification.

Table 2.1   Results of previous research related to threshold values of Z_h at significant
temperature levels related to charging.

Researcher	Thresholds	Associated echo top height	Location	Cell number
Dye et al. 1989	40 dBZ at 6 km	8 km	New Mexico	20
Buechler and Goodman 1990	40 dBZ at -10°C	9 km		15
Michimoto 1991	30 dBZ at -20°C			
Hondl and Eilts 1994	10 dBZ near 0°C		KSC, Fl	33
Gremillion and Orville 1999	40 dBZ at -10°C	9.5 km	KSC, Fl	47
Vincent et al. 2003	40 dBZ at -10°C		North Carolina	50
Wolf 2006	40 dBZ at -10°C	6.7 km	Florida	11164
Mosier et al. 2011	30 dBZ at -15 to -20°C		Houston, TX	67,000+

With the recent introduction and wide availability of dual-polarization (DP) radar,

the use of DP radar data has also become a tool in lightning initiation studies. These

studies primarily use differential reflectivity values to observe the approximate location

of hydrometeors associated with charging mechanisms in thunderstorms. Differential

reflectivity, or Z_{DR}, is the reflectivity weighted measure of axis ratio or approximate

shape (e.g., oblateness) of hydrometeors as described in greater detail in chapter three.

Z_{DR} is commonly paired with high reflectivity values in regions above freezing to assist

in the discrimination of ice particles and rain due to the difference in oblate shape of the

two hydrometeors. A Z_{DR} column is characterized by supercooled rain drops lofted to

heights below freezing while still maintaining their liquid state. Thus the radar signature

of these drops would appear to be values of 1dB or greater for Z_{DR} (Herzegh and Jameson

1992). For example, Figure 2.10 is an example of the Z_{DR} column from a cell in this

study.   As seen in the Figure 2.10, the occurrence of $Z_{DR} > 1$dB and $Z_h > 40$ dBZ at

temperatures below freezing indicates the Z_{DR} column of supercooled rain drops.
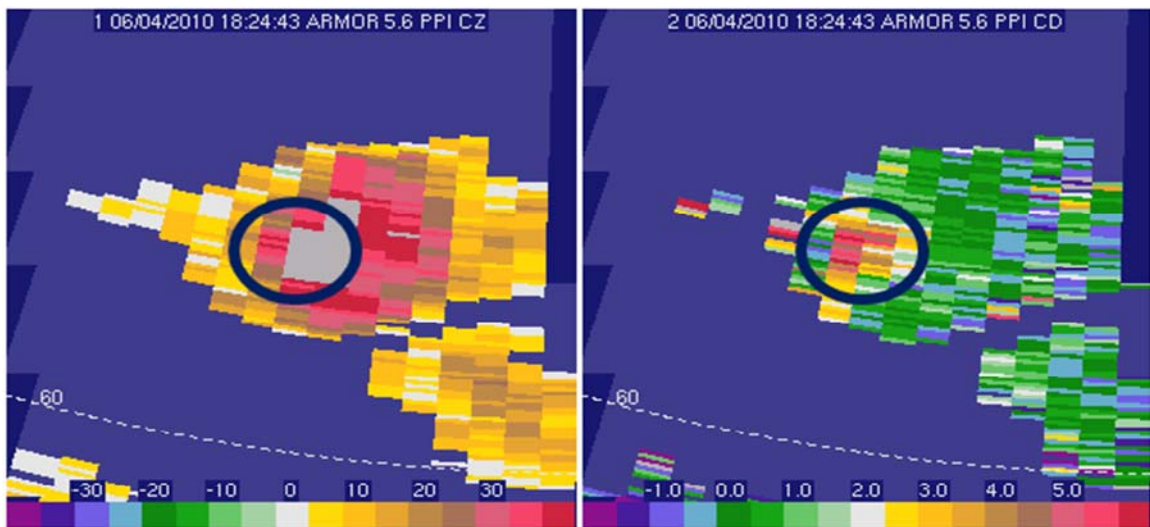
Figure 2.10   Radar values Z_h and Z_{DR}, the indicated area is an example of a Z_{DR}
column. The enhanced values of Z_{DR}, ≥ 1dB, associated with high values
of Z_h, ≥ 40 dBZ, indicate oblique liquid particles at temperatures below
freezing. The altitude of the radar scan is approximately 5.64 km at an
environmental temperature of approximately -8.5°C.

As discussed previously, hydrometeors such as hail form by the coalescence of

liquid rain drops that subsequently freeze. Using DP variables, Z_h and Z_{DR}, and

temperature the process of freezing can be observed. Z_{DR} signatures as a means of

hydrometer identification has been greatly studied (Hall et al. 1984; Aydin et al. 1986;

Goodman et al. 1988; Herzegh and Jameson 1992; Carey and Rutledge 1996, 2000;

Bringi et al 1997; Vivekanandan et al. 1999; Liu and Chandrasekar 2000; Straka et al.

2000; Brandes and Ryzhkov 2004; Lim et al. 2005; Deierling et al. 2005, 2008; Anderson

et al. 2009). However the application of Z_{DR} columns to the study of lightning initiation

(e.g., Goodman et al. 1988; Herzegh and Jameson 1992; Bringi et al. 1997; Carey and

Rutledge 2000; Lund et al. 2009) is not as extensive as that of reflectivity and thermal

threshold studies. Z_{DR} is utilized to differentiate between rain and ice due to differences

in size and dielectric constants. In regions of mixed precipitation phases, Z_{DR} becomes

dominated by the largest return signals thus masking smaller precipitation signatures in

the radar volume. A small amount of hail stones could dominate a radar return of a

volume consisting of mostly smaller graupel and droplets. Goodman et al. (1988) found

a 4-6 minute lead time after the first detection of a hail signature as indicated by radar

Z_{DR} values less than 0.5 collocated with reflectivity values of 50 dBZ or more at heights

of 6.5-7.5 km or about -10 to -15°C. Furthermore, Jameson et al. (1996) found "the onset

of electrification coincides with the appearance of a significant volume of Z_{DR} above the

-7°C level." Jameson et al. concluded that though this method of electrification detection

could be useful in forecasting lighting, the current basic reflectivity technique is

sufficient for first flash predictions. Carey and Rutledge (2000) confirmed a correlation

of hydrometeors associated with the NIC process as determined by Z_h and Z_{DR}. This

correlation is evident in the lofting of rain drops, indicated by enhanced Z_{DR} and Z_h, and

the freezing and formation of hail and graupel, as indicated by the reduction of Z_{DR}. This

indicates the presence of hydrometeors required for significant charging. In a general

polarimetric study of the development of a thunderstorm, Lund et al. (2009) found Z_{DR}

columns of Z_h 37.5-57.5dBZ and Z_{DR} 0.375-1.623dB associated with lightning initiation.

Bringi et al. (1997) noted the occurrence of the first lightning flash six minutes after the

disappearance of the Z_{DR} column, which was associated with the freezing of supercooled rain drops. Supercooled rain drops are one of the hydrometeor types identified by the NCAR particle identification (PID) algorithm (Deierling et al. 2008; Vivekanandan et al. 1999) used in this study. PID is clearly useful in determination of hydrometeors related to NIC.

From the first formation of a convective storm, to the first flash, the development of a convective cell can be tracked and observed by radar. This process has allowed the study of the physical processes of charge accumulation in thunderstorms. By detecting specific hydrometeors significant to charging, such as graupel, hail and supercooled rain drops, it is possible to forecast the onset of electrification by relation to the presence of these particles. The purpose of this study is to determine if the utilization of DP variables provide a significant advantage relative to reflectivity alone in first flash forecasting. *Our hypothesis is that the use of DP variables provides significant improvements to first flash forecast skill and lead time compared to the radar reflectivity based algorithms currently employed, because of DP radar's ability to differentiate hydrometeor types necessary for NIC, significant electrification and lightning.* More specifically, we are investigating the following questions:

Does the use of DP variables increase forecasting lead time?

Does the use of DP variables significantly reduce forecasting false alarm?

Is there a significant skill difference in forecasting using different methods of DP variable first flash forecasting?

Are different methods more advantageous in forecasting CG lighting than forecasting total lightning?

CHAPTER III

DATA AND METHODOLOGY

On average, north Alabama has 120 days of measurable precipitation

(precipitation >0.01, including snow and rain) per year according to the National Climatic

Data Center (NCDC 2011). Of these precipitation days, about fifty of them are

thunderstorm days (NWS 2011a). The data in this study are comprised of eight case

dates from two years, 2008 and 2010, containing thirty-one pulse-type thunderstorms,

twenty-seven of which produce CG flashes, and nineteen non-lightning producing storms.

Table 3.1 breaks down the different case dates and number of cells associated with each

case. This table explains the convective situation, local or frontal, for each case date.

Pulse-type storms are typically small in size, about five kilometers radius, and exhibit

rapid development with a short life span, approximately thirty minutes. Pulse-type

thunderstorms are single cellular storms that develop by local convective mechanisms

and are spatially distinctive from other cells. These cells occasionally merge together.

Independent storm cells merging together before first flash are included and counted

independently if initiation is forecasted before merging. Of the seven cells within the

data set that merge with another cell, only two do not demonstrate convective thresholds

required by the test algorithms discussed in this chapter. These storm types are desirable

for this study so that the life cycle and evolution of the storm cell's precipitation

development relative to charging can be observed. The following sections will describe

the tools used for data collection and the data processes and algorithms implemented in

this study.

Table 3.1   Analysis of the 8 case dates analyzed in this study. The first column
             indicates the date (year,month,day), the second column is the total number
             of cells selected from the case for examination, the next two columns
             break down the number of non-thunderstorm (NT) cells and cloud-to-
             ground (CG) cells, the final column indicates the general atmospheric
             forcing mechanism for the weather events.

Casedate	Total Cells	NT cells	CG cells	Convection
20100528	8	2	4	Local
20100601	6	2	4	Local
20100602	22	9	13	Local
20100604	1	0	1	Local
20100729	5	2	1	Local
20080411	3	2	1	Frontal
20080625	1	0	1	Local
20080708	4	2	1	Local

Table 3.2   Specifications of ARMOR, C-Band DP radar (Petersen et al. 2005, 2007).

Transmit Frequency	5625 MHz
Beam Width	1.0°
Wavelength	5 cm (C-band)
Maximum rotation rate	36 Degrees/second
Pulse Length	0.4-2.0 μs
Pulse Repetition Frequency (PRF)	250 -2000 Hz
Transmitted Polarization	Simultaneous H and V (STAR)
Received Polarization	H and V
Maximum Range	150 km
Radar Gate/Spacing	75 – 1000 m/125 m
Variables	P, Z, V, W, Z_{DR}, ρ_{hv}, Φ_{DP}

3.1 Instruments

3.1.1 Radar: ARMOR

The data from the eight case dates were retrieved using the C-band dual-polarimetric radar, UAHuntsville's Advanced Radar for Meteorological and Operational Research (ARMOR) (Petersen et al. 2005, 2007). ARMOR is located in northern Alabama at the Huntsville International Airport just outside of Huntsville.   ARMOR sends and receives a pulsed 5 cm, one degree, STAR (simultaneous transmit and receive) microwave signal. STAR is the process by which the radar sends and receives both vertical and horizontal signal in the same pulse. The beam width is determined by the angle of the main lobe as related to the axis center of the radar signal. The 3 dB beam width of AMOR is 1°.   Five centimeters defines the wavelength of the signal. The wavelength is important in radar measurements due to scattering properties. At C-band, an object sensed or measured by the radar signal that is less than approximately 5 mm in diameter along the measured axis will be Rayleigh scatters (Rinehart 2010). Those particles larger than 5 mm are Mie scatters and could cause errors in C-band radar assumptions and ambiguities in data interpretation. Further radar properties related to error mitigation includes the radar range. The maximum range of the radar coverage is approximately 150 km as depicted in Figure 3.1. The maximum radar range is the maximum distance from the radar at which data quality begins to reduce due to characteristics such as beam spreading (Rinehart 2010). The radar signal is transmitted in a cone, and the further from the radar the beam travels, the larger the cone becomes, an effect called beam spreading. Beam spreading errors can bias DP variables and thus affect the determination of hydrometeors based on DP variables (Ryzhkov 2007). Beam

spreading also reduces the resolution of the radar data, which could thus cause errors in analysis. Another constraint on the maximum range of the radar is the maximum unambiguous range of the radar. This is the range at which a radar signal can travel, and return, before the next signal pulse is sent. Radars sample the atmosphere by sending multiple pulses to one target volume, a pulse volume. ARMOR is capable of sending 250 to 2000 pulses per second; this is called the Pulse Repetition Frequency (PRF). The PRF of this study is 1200 pulses per second resulting in a maximum unambiguous range of 125 km. A radar pulse volume is a sample volume that is defined by the radar 3-dB beam width, the range of the sample volume, and the gate spacing. The gate spacing of these samples is 125 m (Petersen 2007). Now that the basic characteristics of the radar signal are known, next the basics of how radar measures precipitation will be discussed.
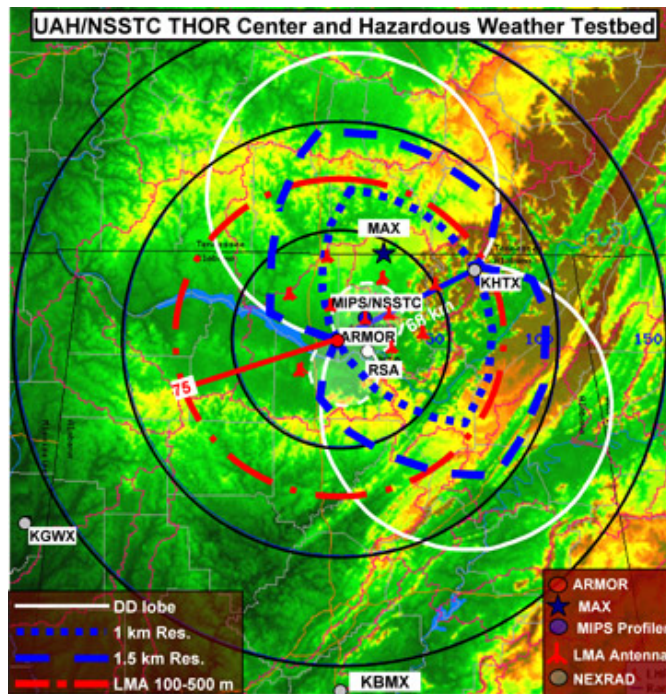
Figure 3.1   Map of the range and location of ARMOR. ARMOR has a range of approximately 150 km which overlaps the coverage area for KHTX radar. [Image credit to ARMOR, 2011.]

Radar reflectivity (Z) is a theoretically based value dependent on the size and concentration of the hydrometeors. This theory assumes all the hydrometeors are spherical and small relative to the radar signal's wavelength, thus conforming to Rayleigh scattering assumptions. The radar reflectivity is then defined as the 6th moment of the particle size distribution as follows:

$$Z = \int_0^\infty N(D)\, D^6\, dD \quad [mm^6 m^{-3}],$$

where N(D) is the particle concentration per unit volume and D is the particle diameter. If the hydrometeors in the radar resolution volume conform to the previously stated criteria (i.e., they are small relative to the radar signal wavelength) and are liquid water drops, then $Z = Z_e$ (Smith 1984). Z_e is the effective radar reflectivity factor, an estimation that can be derived from the radar range equation:

$$P_r = \frac{C\,|K_w|^2\,Z_e}{R^2}.$$

P_r is the received power of the return signal scattered by the hydrometeors in a radar pulse volume at a range, R. C is a set of constants that are representative of the radar characteristics, such as the power transmitted by the radar, antenna gain and wave length. $|K_w|^2$ is the dielectric function of liquid water.

Differential reflectivity (Z_{DR}) is the ratio of reflectivity as measured in horizontal and vertical polarizations. The equation is as follows:

$$Z_{DR} = 10\log_{10}\left(\frac{z_h}{z_v}\right) \quad [dB].$$

The Z_{DR} equation consists of z_h, the reflectivity measured in the horizontal plane, and z_v, the reflectivity measured in the vertical plane where the units of both reflectivity factors are $mm^6 m^{-3}$. Z_{DR} provides a measure of the reflectivity-weighted oblateness of

hydrometeors in a radar volume (Rinehart 2010). This means, that if the reflectivity

factor is mostly attributed to large hydrometeors, such as graupel, in a volume, then that

is what will be similar in Z_{DR}. The volume likely contains various other hydrometeors of

smaller sizes but they do not exert same impact due to the D^6 dependency. A highly

oblique hydrometeor, such as a large raindrop, will have a high Z_{DR} value of

approximately 0.5dB to 4dB due to the larger horizontal axis versus the vertical axis

(Bringi and Chandrasekhar 2001; Rinehart 2010). As a rain drop grows in size, it

becomes more oblate due to forces, such as surface tension and gravity, enacting upon the

drop. Thus larger drops (> 3 mm) generally have larger Z_{DR} values opposed to smaller

drops (< 3 mm). A tumbling hail or graupel stone will have a Z_{DR} value near zero due to

the averaged orientation of the nearly spherical hydrometeors (Bringi and Chandrasekhar

2001; Rinehart 2010).
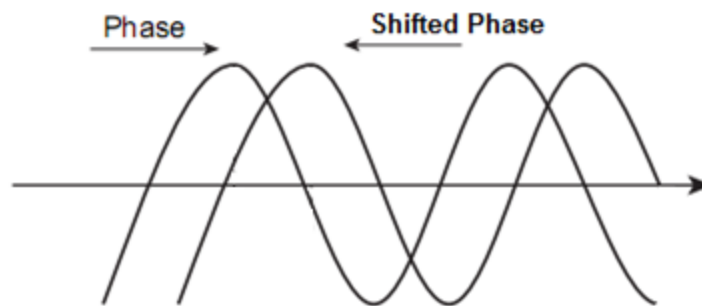
Figure 3.2   Depiction of the phase shift of a wave. The first wave is the original wave
               and phase. The second wave is an example of a phase shift to a wave
               form.

Differential phase shift (Φ_{DP}) is a difference of the phase shift (e.g., Figure 3.2) of

the horizontal and vertical signal as perceived by the radar upon signal return as seen in

the following equation:

$$\Phi_{DP} = \Phi_{HH} - \Phi_{VV} \quad [°].$$

Φ_{HH} is the phase shift of the horizontally transmitted and horizontally received signal. Φ_{VV} is the phase shift of the vertically transmitted and vertically received signal. This phase shift is caused by the signal propagation through mediums of different temperatures and water content (i.e., refractive index) that alters the speed at which the wave travels (Rinehart 2010). This occurs both on the transmitted wave and the returned signal. This phase shift will increase with range as the signal travels through the different precipitation water content and thermodynamic phases. To estimate the phase shift at a specific range, a range derivative of Φ_{DP}, called specific differential phase shift (K_{DP}), can be estimated by the following equation:

$$K_{DP} = \frac{\Phi_{DP}(r_2) - \Phi_{DP}(r_1)}{2(r_2 - r_1)} \quad °/\text{km.}$$

The difference of Φ_{DP} at two different ranges of interest is divided by half the distance to achieve an estimated value of phase shift for a single trip. K_{DP} is dependent on orientation, shape, size, number concentration and phase of the hydrometeors. K_{DP} assists in determination of the physical phase of the hydrometeors present in a radar volume due to phase dependent propagation speeds, since this value is unaffected by spherical hydrometeors, such as hail (Bringi and Chandrasekhar 2001; Rinehart 2010). Φ_{DP} is the difference of the phase shift of both polarities, and an accordingly a spherical hydrometeor will return the same phase shift in both polarities, thus resulting in no differential phase shift. As discussed later, K_{DP} is also useful in attenuation correction.

Correlation coefficient (ρ_{HV}) is the determination of the correlation, or similarity, between the horizontal and vertical pulse signals as received by the radar with zero lag.

Radar transmits an electromagnetic signal that travels at the speed of light. This enables the radar to transmit several signal pulses at the same target volume, allowing the radar to take several samples of the same volume. The correlation between returned horizontal and vertical signals in a pulse is calculated in the following equation:

$$\rho_{HV} = \frac{|V_{signal}||H_{signal}|}{\left(|H_{signal}|^2 |V_{signal}|^2\right)^{1/2}}$$,

V_{signal} and H_{signal} are the radar received pulse signals of the vertical and horizontal polarizations, respectively. This variable depends on the scattering properties of the medium and assists in determination of hydrometeors. This variable is useful in the determination of meteorological and non-meteorological objects in a radar volume. A volume of raindrops which have a general uniform shape, orientation, and phase is characterized by values of ρ_{HV} near 1 due to the well correlated pulse signals (Rinehart 2010). Non-hydrometeor objects, such as insects which shapes are variable depending on the angle of orientation to the signal, will produce a lower ρ_{HV} values, such as 0.8 or less, due to less correlated signals. A volume of mixed phase particles will also produce a less correlated signal due to the difference in hydrometeor shape, sizes, and phase in the volume. A large hail stone, with a diameter on the order of or larger than the signal wavelength, will scatter the incident signal in the Mie regime thus producing a lower ρ_{HV} value. ρ_{HV} is useful for data quality determination because it is unaffected by calibration errors and effects of propagation such as attenuation and ability to differentiate non-meteorological targets and signal noise.

The final characteristic of ARMOR to discuss in this section is the method by which it scans the atmosphere to collect the data as previously described. ARMOR is

capable of scanning the atmosphere in two planes: azimuth and elevation. The

elevational method of scanning is called Range Height Indicator (RHI). In this

technique, the radar takes a vertical cross-section of the atmosphere by scanning at

varying elevation angles at a fixed azimuth angle. The azimutal method of radar

scanning is called Planned Position Indicator (PPI) in which the radar revolves in the

azimuth at a fixed elevation angle. The radar can scan at different PPI elevation angles,

thus allowing the radar to scan the upper and lower levels of a storm. This scanning

method allows the radar to scan a volume of the atmosphere. Two different PPI radar

scan strategies were employed in the data collection process in this study. The scan

strategy used in 2008 is a fixed scan strategy in which each elevation angle of the radar

scan was predetermined and not based upon the current weather development. For

example, the radar would scan at elevation angles in increments of every 0.7° starting at

0.5°. The scan strategy implemented in 2010 optimizes the volume elevation scan levels

based upon a targeted range from the radar and environmental temperature profile. This

scan strategy was developed in support of Patrick AFB, Fl, and the 45th Weather

Squadron (Carey et al. 2009). The goal of the scan strategy is to produce high resolution

data coverage of the significant charge region, 0 to -20°C. Zero to negative

twenty degrees Celsius of a mature cumulus cloud is the mixed phase region in which

charging occurs. It is desired to have the greatest data resolution in this region. As seen

in Figure 3.3, the beam of a radar projected at some elevation angle gradually increases in

height the further in range it extends. This is due to the projection of the beam as well as

the natural curvature of the Earth. To determine the actual height of an object of interest

based on the elevation angle of the scan and range of the object from the radar, the

4/3^{rds} Earth radius equation is used (Rinehart 2010):

$$H(r, e_a) = \sqrt{r^2 + \left(\frac{4}{3}R\right)^2 + \left(2\,r\frac{4}{3}R\sin\left(\frac{\pi}{180}e_a\right)\right)} - \frac{4}{3}R + a$$,

where H is the height in kilometers of the radar target at some range from the radar. The

range from the radar in kilometers is r. The elevation angle at which the radar is scanning

the target is e_a. R is the radius of the Earth, approximately 6374 km. This equation was

inverted to determine the closest elevation angle at which a radar scan strategy would

bisect a cell of interest at some range.
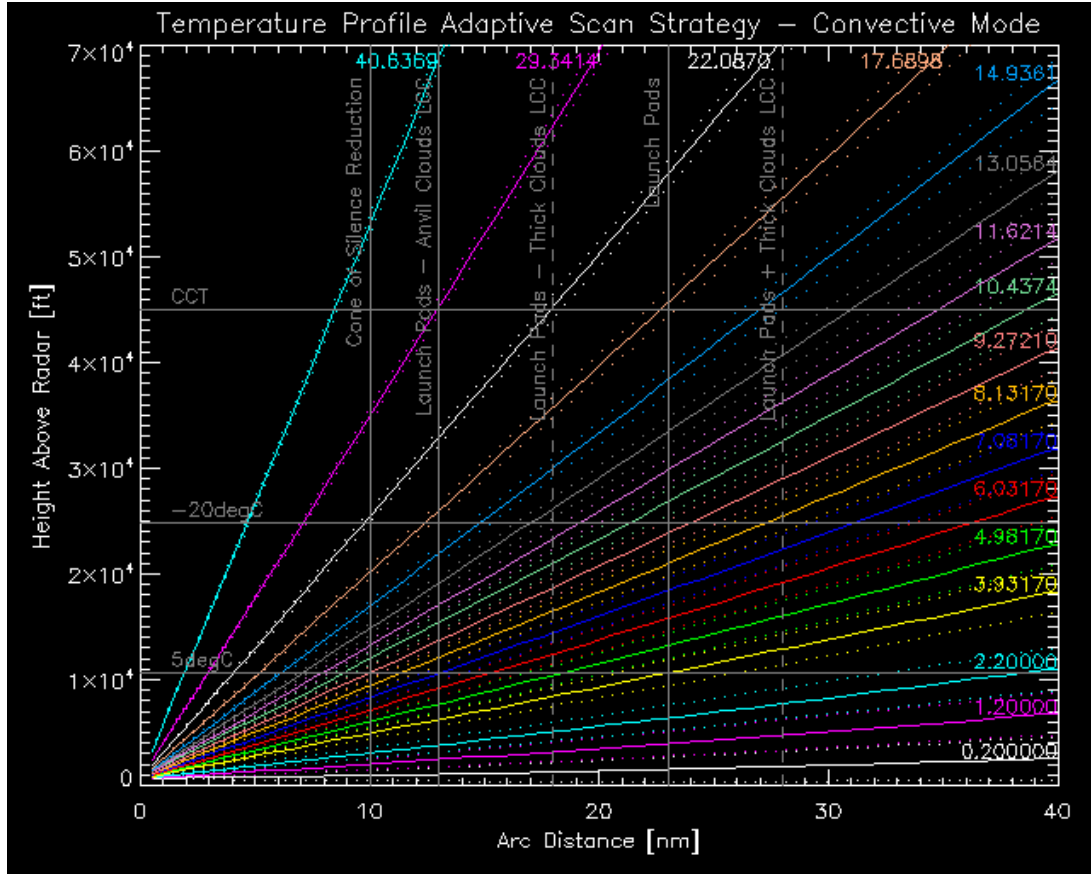
Figure 3.3   Cross-section of radar scan strategy with range height relation. Optimized
             radar scan strategy for 20100601. The solid lines indicate the center of the
             beam, while the dashed lines indicate the area covered by the 3 dB beam
             width.

Further evaluation of the radar scan strategy was conducted to ensure data quality, based on the employed scan strategies. Based on the desired data coverage of the thermal heights of interest, -10 to -20°C, by the radar scan strategy in each case, an analysis range limit was determined based on the distance between beam height centers of the scan strategy. The thermal levels of interest have a vertical difference of about one to two kilometers in profile, no more than 700 meters (0.7 km) vertical distance may be between scan centers to ensure high vertical resolution. A scan strategy with more than 0.7 km range between scan centers results in gaps in the vertical data coverage leading to errors in lead time estimates and lower accuracy confidence. To further ensure temporal resolution of microphysical events, the maximum time between radar scans is five minutes. A scan strategy with a time lag greater than five minutes could miss important microphysical events such as the occurrence of a Z_{DR} column and lead to errors in lead time estimates. Furthermore, each storm cell of interest must be covered by the radar scan sector from initial formation to either first flash or dissipation. First flash is defined as the first occurrence of a single flash as detected by the Northern Alabama Lightning Mapping Array (NALMA) or the National Lightning Detection Network (NLDN). As discussed in Chapter Two, a cell is considered to enter the dissipating stage of cellular life cycle when the cell no longer supports development and the radar reflectivity values no longer indicate the location of a significant precipitation core for a series of at least two volume scans.
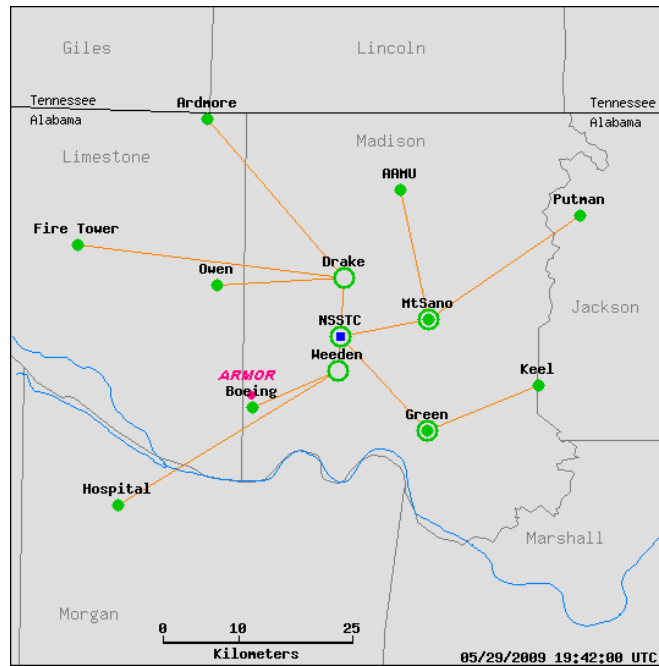
Figure 3.4   Map of the North Alabama Lightning Mapping Array, the NALMA
             consists of 11 TOA VHF sensors centered on the NSSTC. Locations of
             the sensors are indicated by green dots, green circles indicate locations of
             relay centers, the base station is indicated with the blue square, and the
             pink dot indicates the location of ARMOR relative to the array.
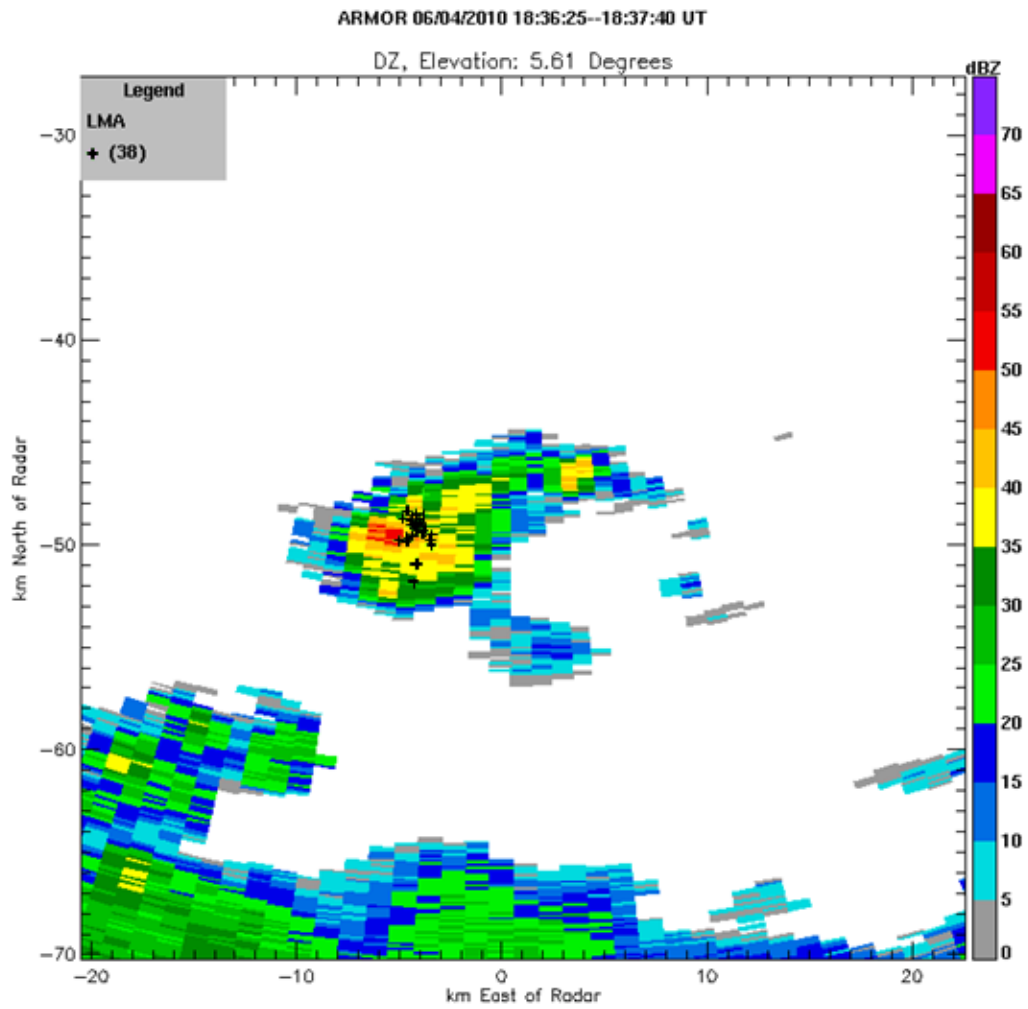
Figure 3.5   LMA sources and radar reflectivity of cell 1 from case 20100604 at
              approximately -10°C. The LMA source data of one flash from 1837 UTC
              over lays radar reflectivity, Z_h. Each black plus indicates a source
              location.
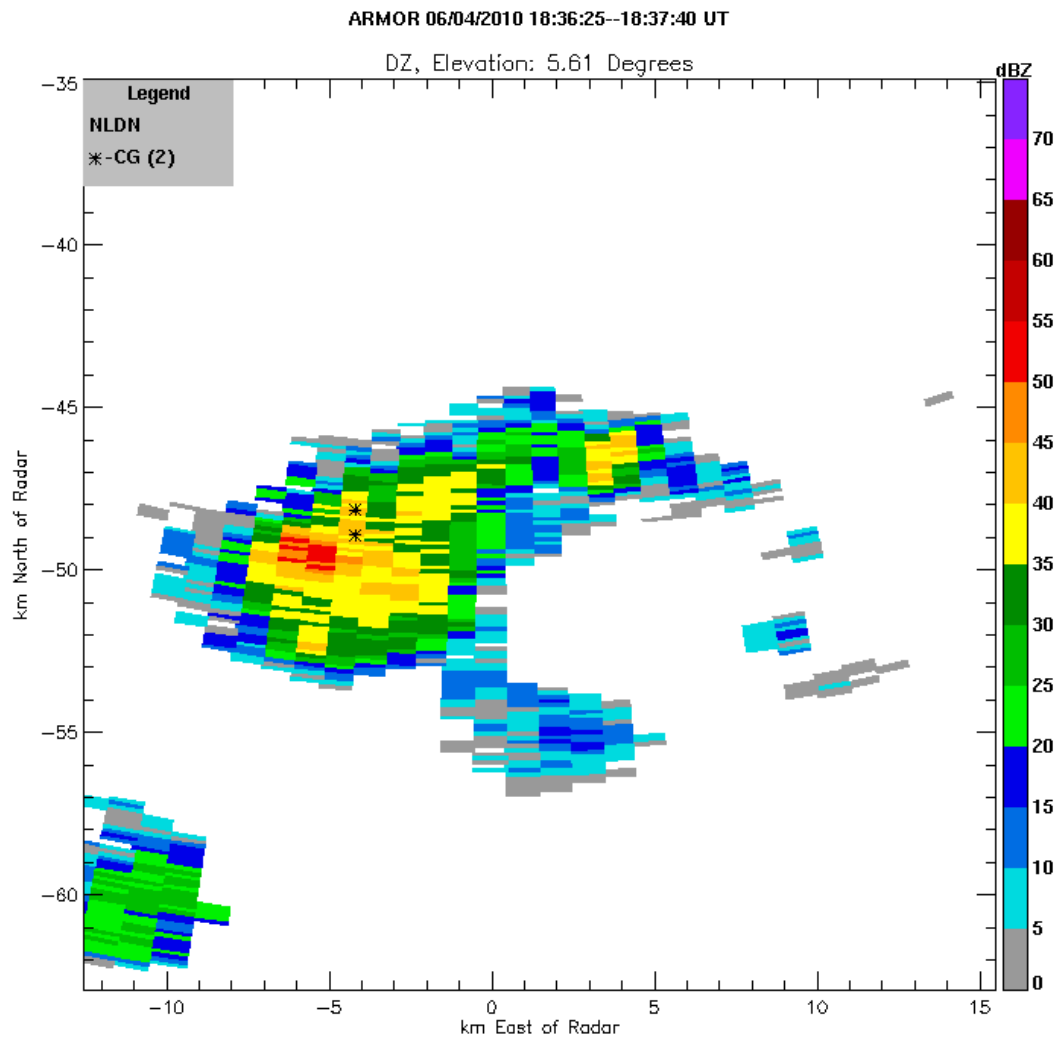
Figure 3.6   NLDN flash location of two CG flashes over laying radar reflectivity of cell 1 from case 20100604 at 1837 to 1842 UTC at approximately -10°C. Each black asterisk indicates a CG flash.

3.1.2 NALMA and NLDN

In addition to the radar, other vital tools to this study are the Northern Alabama Lightning Mapping Array (NALMA) and National Lightning Detection Network (NLDN). NALMA is a network of eleven time of arrive (TOA) very high frequency (VHF) sensors (Krehbiel et al. 2000; Koshak et al. 2004; Thomas et al. 2004; Goodman et al. 2005). See Figure 3.4 for map and sensor location reference. These sensors detect VHF radio waves associated with both CG and IC lightning. The sensors record the times of the peaks in the radiation signals indicative of a pulse from lightning. Determination of the 3-D location of the source is based upon the time of the signal's arrival at the sensor's location in relation to the signal received by other sensors in the array (Proctor 1971). This method of detection gives the geographical location and altitude of the signal's source. As discussed in Chapter II, a flash of lighting is comprised of multiple VHF sources. Using a graphical interface, the location of the first flash was determined by the location of more than five sources that occur nearly simultaneously, less 0.1 seconds, to constitute as an initial flash location (Figure 3.5). To ensure the accuracy of the sources related to first flash location, a flash construction algorithm that groups sources to create a lightning flash (McCaul et al. 2005) was used. This algorithm is designed to filter signal noise (Koshak et al. 2004) out of the data and locate the first source associated with each flash. The algorithm determines the association of each source to a flash due to the sources' related time and location. The source must occur within 0.3 s and 0.05 azimuth radians of the previous source. This means, if the source occurs at an approximate distance of 60 km from the NALMA center, then the following source must occur within 0.3 s and a 3 km radius to be categorized as an associated

source. There is no limit to the number of sources associated to a single flash. The first source of the first flash is considered the location and time of the initiation of thunderstorm activity for the purposes of first flash algorithm testing.

The NLDN is used for determination of the first CG flash. NLDN is a network of over 100 LF sensors located throughout the continental United States and is owned and monitored by Vaisala (Cummins and Murphy 2009; GSFC NASA 2011). NLDN, like NALMA, are time of arrival sensors, unlike LMA, the NLDN operates on low frequencies (LF). The NLDN network was designed to sense and report on the low frequencies emitted by the return stroke of CG flashes. The LF sensors are less sensitive to weaker pulse signals, such as those produced by IC lighting. Though the network does report on IC flashes, the detection accuracy is low and some are misclassified as CG (Cummins and Murphy 2009). The NLDN data used herein reports the data in the form of flash location, and as stated before, a flash is comprised of many strokes. Since the NLDN is reported in flash data, as seen in Figure 3.6, only one flash is required for confirmation of lightning initiation. For the purposes of this study, it is assumed perfect accuracy of CG detection.

3.2 Cell Selection

Both case date and cell selection in this study was a rigorous process. First the case date is analyzed for convective features. If a case date is dominated by a squall line, or large multicellular structure, it is not considered for analysis due to the desire to evaluate individual cellular development of convective processes. If the cells of the case date do not demonstrate individual structures from initial formation to first flash, the cells

are not selected. Each cell that is selected for evaluation is then analyzed to determine

the location and adhesion to the rule of the defined Larsen area. The concept of the

Larsen area was initially implemented by Larsen and Stansbury (1974) as a method of

radar analysis and lightning location. The Larsen area, is a region of significant radar

reflectivity at a significant thermal level. For the purposes of this study, the cells are

analyzed based on the Larsen area as defined by horizontal reflectivity threshold of

≥ 30 dBZ at -10°C, as pictured in Figure 3.7. Reflectivity ≥ 30 dBZ indicates significant

cellular development of a precipitation core based on particle-size-distribution of

hydrometeors related to charging, such a liquid water, graupel and hail. As discussed in

Section 2.2, -10°C is significant to the charge structure of a thunderstorm and the lower

level of the mixed phase region and main charging region of the main negative charge

layer. The Larsen area, or area of interest, in this study is defined by the estimated center

and radius of interest as determined by ≥ 30 dBZ reflectivity echo evaluated objectively

from a PPI scan that intersects the cell of interest closest the thermal height of -10°C. For

one case date, 20100602, the Larsen area was redefined to a threshold of ≥ 25 dBZ at

-10°C to include in this study two non-thunderstorm cells that do not reach the threshold

of 30 dBZ. An example of this reduced Larsen area is represented in Figure 3.8. This

process provides a more robust selection of cells, and is evidence to support the

assumption that a cell maintaining reflectivity less than 30 dBZ at -10°C would not

develop an electrical charge strong enough to discharge lightning. This is due to the fact

that a precipitation core above the freezing level with a low particle-size-distribution, as

determined by reflectivity value, is less likely to contain significant amounts of

precipitation key to charging. The case date of 20100602 was selected for the lowered

Larsen area threshold based upon the greater number of independent cellular structures observed in the case. The two cells of this case that were observed at the lower Larsen area threshold were selected due to their evidently cellular structure at levels lower than -10°C as seen in Figure 3.9. Their cellular life cycle never achieves significant concentrations of large ice hydrometeors in the presence of supercooled drops as is needed for sufficient charge accumulation capable of leading to lighting.
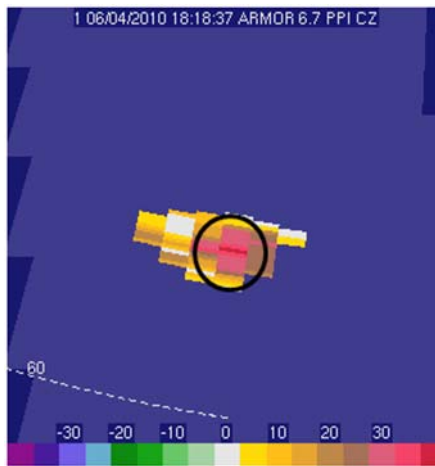
Figure 3.7   Larsen area of cell 1 of case 20100604 is indicated by the black circle. The Larsen area is defined as the reflectivity threshold ($\geq$ 30dBZ) at thermal threshold (-10°C). The area is determined by the estimated center of the reflectivity echo and radius determined by the estimated radius required to encompass the majority of the threshold reflectivity gates. The altitude of the radar scan is approximately 5.64 km at approximately -10°C.
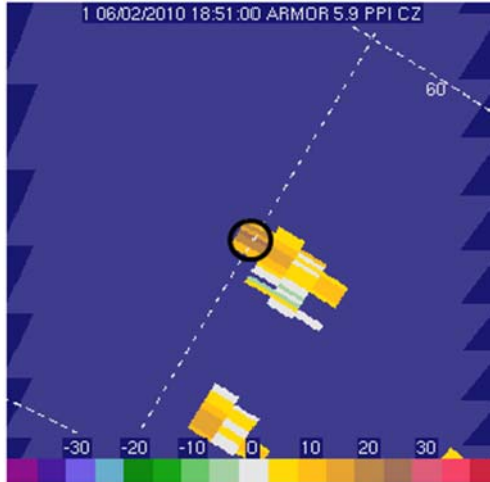
Figure 3.8   Larsen area of a non-thunderstorm cell with lowered requirements for the
             Larsen area, cell 20 case 20100602. The lowered requirements of the
             Larsen area are defined as the reflectivity threshold ($\geq$ 25 dBZ) at a
             thermal threshold (-10°C). The area is determined by the estimated center
             of the reflectivity echo and radius determined by the estimated radius
             required to encompass the majority of the threshold reflectivity gates. The
             altitude of the radar scan is approximately 5.83 km at approximately
             -10°C.
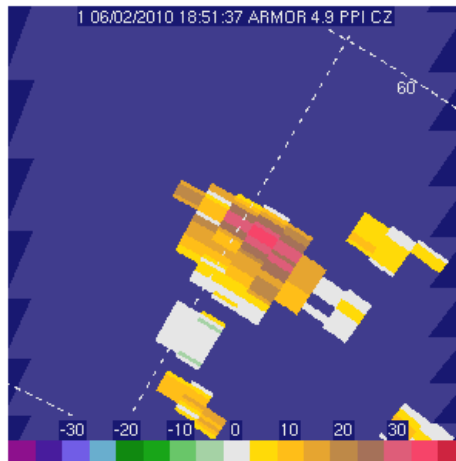
Figure 3.9   Radar reflectivity of cell 20 case 20100602 below the Larsen area at
             approximately 4.91 km. Enhanced reflectivity values below the Larsen
             area are indicative of cellular development.

3.3 Atmospheric Sounding

Determination of thermal levels in this study was achieved using environmental soundings collected in two manners. For dates after May 2010, the environmental sounding was provided by the Redstone Arsenal Meteorological team, Huntsville, AL, a distance of 13.6 km, about 8.5 miles, east of ARMOR. The team launched balloon sounding daily at 12Z during the course of this study. Any date prior to May 2010, the sounding is a linear average of the sounding data from the Birmingham, AL, NWS office and the Nashville, TN, NWS office at the nearest time to the weather event. This method is an approximation of the Huntsville environmental profile.

3.4 Radar Data Analysis Methodology

3.4.1 Z_h and Z_{DR} Calibration

Radars, like many instruments, require constant monitoring to ensure accurate calibration. This section will discuss the methods used for Z_h and Z_{DR} calibration. Z_{DR} calibrations are conducted by sampling a volume of approximately spherical hydrometeors (Bringi and Chandrasekar 2001a; Ryzhkov et al. 2005). Ideally, accurately calibrated radar Z_{DR} of approximately spherical hydrometeors, such as small drops in drizzle or light rain, would be near zero. Any amount off zero results in the bias related to the polarized signal. The method of calibration of ARMOR is conducted by azimuthally scanning 360° at 90° elevation angle in the presence of light rain or drizzle. This scan method is referred to as a "birdbath", because the vertically pointed radar

resembles one (Gorgucci et al. 1999). ARMOR Z_{DR} is routinely calibrated to ensure data quality.

A bias in Z_h can occur due to drifting of the engineering variables associated with the radar constant due to instrumental variations that naturally occur. The Z_h calibration method employed with ARMOR is the self consistency method which uses Z_h, Z_{DR}, and K_{DP} (Ryzhkov et al. 2005). A computed Z derived from Z_{DR} and K_{DP}, is compared to the measured Z_h to determine the bias. It is assumed in this process that Z_{DR} is unbiased, thus a need for accurate Z_{DR} calibration. Z can be obtained by following equation:

$$Z = a + b \log (K_{DP}) + c \, Z_{DR} \quad ,$$

where Z is the calculated reflectivity factor, K_{DP} and Z_{DR} are the radar derived variables. The coefficients, a, b and c, are dependent on radar wavelength and raindrop shape, and are "supported to be relatively insensitive to the [drop-size-distribution] variations" (Ryzhkov et al. 2005). This method utilizes the assumption that in the presence of rain, void of ice and non-hydrometeor scattering targets, Z_h, Z_{DR} and K_{DP} are dependently related. Thus this method was conducted on a radar sample consisting purely of rain as can be estimated by a combination of DP variables, such as Z_h, Z_{DR}, K_{DP}, ρ_{HV}, and the environmental sounding.

3.4.2 Attenuation Correction

C-band dual-polarimetric Z_h and Z_{DR} are prone to differential attenuation and attenuation, respectively, in precipitation. Precipitation attenuation is due to intense rainfall in which the transmitted signal is absorbed or scattered by hydrometeors in the path reducing the received signal power. This then produces weaker received signal

power. Differential attenuation is attenuation differences between the horizontal and vertical signal caused by the differences in hydrometeor shapes in the vertical and horizontal planes. Volumes of oblate raindrop will attenuate the signal more in the horizontal plane than in the vertical due to the greater mass in the horizontal plane than the vertical.   Errors such as these negatively affect rain estimations and accuracy of PID. Φ_{DP} is used in attenuation correction because it is unaffected by calibration and attenuation issues, and, as described previously, demonstrates the phase difference between horizontal and vertical (Zrnic and Ryzhkov 1996; Carey et al. 2000). The method employed by ARMOR for attenuation correction accomplished using a Z_{DR} constrained "ZPHI" approach suggested by Bringi et al. (2001). This methodology adds onto previous methods (Hitschfeld and Bordan 1954; Testud et al. 2000) with a self-consistent method. This process uses the ratio of radar measured Z_h (or Z_{DR}) difference at two reference gates and Φ_{DP} difference at two reference ranges, the max range set at some distance beyond the attenuation (Bringi et al. 2001), to determine the correction coefficient for two way attenuation correction. This method derives from the relation of specific attenuation correction, A_h, and specific differential attenuation, A_{hv}, to K_{DP}. This linearly proportional relationship yields the following equations as related to attenuation correction coefficients, a and b:

$$A_h = aK_{DP}$$
$$A_{hv} = bK_{DP} \quad .$$

The derived method of attenuation correction is employed to mitigate the issue of large errors caused by variability in hydrometeors and temperatures related to a set correction coefficient.

3.4.3 PID

Particle identification by way of radar signatures has been greatly studied (Hall et al. 1984; Goodman et al. 1988; Carey and Rutledge 1996, 2000; Bringi et al. 1997; Vivekanandan et al. 1999; Zrnic et al. 2000, 2001; Brandes and Ryzhkov 2004; Lim et al. 2005; Deierling et al. 2008). These studies use the radar derived variables and the physical meaning of each signature to determine the approximate bulk hydrometeor in a radar volume. Different hydrometeors respond differently to the radar signal, such as the use of Z_h and Z_{DR} used to determine the relative shape of hydrometeors. For example, studies have used variables such as Z_h and Z_{DR} to identify the difference between ice hydrometeors and liquid at levels above freezing, such as the research conducted by Carey and Rutledge (1996). Carey and Rutledge found a correlation of Z_h values of 45-60 dBZ and Z_{DR} -0.5 - 0.5dB to the location of graupel and small hail in a precipitation core at temperatures below freezing. The relation of radar values to hydrometeor type is not perfectly unique for each variable, such as Figure 3.10 shows for the relation of Z_h and Z_{DR} to hydrometeor type. Based upon association of different values for different variables, an estimated relationship can be assumed.
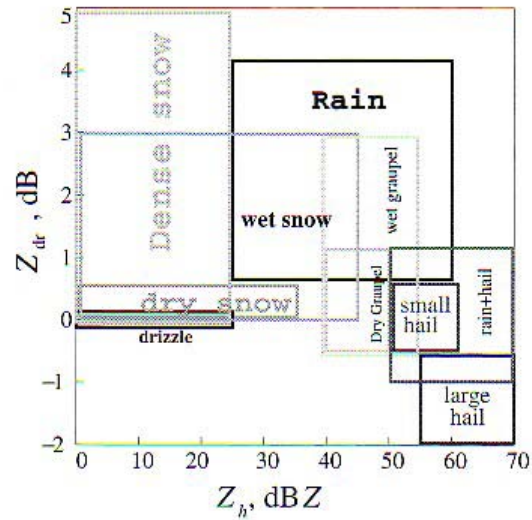
Figure 3.10   Hydrometeor classification thresholds based on association of Z_h and Z_{DR}
for S-band.
[Image credits to Bringi and Chandrasekar (2001) based on Straka and
Zrnic (1993).]

There are two methods to arrive at PID conclusions, Boolean or fuzzy logic.

Boolean logic determines the association of a hydrometeor based upon an if-then, yes-or-

no binary response for each variable and the associated value threshold. For example, if

the Z_{DR} value is 2.3 dB and 40 dBZ Z_h, it would be categorized as a yes (or one) in

association to rain and no (zero) in association to hail as in Figure 3.10. This method

results in errors due to the overlapping values. The NCAR PID algorithm conducts this

process through a fuzzy logic system. Unlike a Boolean logic system, a membership

function, much like a percentage, is assigned to each variable indicating the likelihood of

the value fitting a category (Vivekanandan et al. 1999). This method assists in

accounting for the fact that there is no hard line in variable thresholds associated to

hydrometeor types. Figure 3.11 demonstrates the beta function associated with a general

membership function. Each DP variable has a membership function for each

hydrometeor. These membership functions are then weighted and added together. The weighting of the functions is done in accordance to the importance of the variable's ability to determine the hydrometeor. The modified NCAR PID weights Z_h, Z_{DR}, and temperature the most. Weightings can be different between different PID programs, as can be the method of aggregation. NCAR PID aggregates the values by addition. Another possible method is multiplication. This aggregated value is used to "defuzzify." The maximum value corresponds to the maximum likelihood of association to a hydrometeor category. These categories are seen in Table 3.3. The National Center for Atmospheric Research (NCAR) Particle Identification (PID) algorithm (Vivekanandan et al. 1999) was originally designed to estimate the bulk, or average, hydrometeor type present in a radar volume as derived from polarimetric data of a S-band (10 cm) radar. The difference between S-band radar and C-band radar (5 cm) is the wavelength of the radar. ARMOR operates with a 5 cm wavelength radar signal; this difference is significant to the radar detection of Rayleigh and Mie scattering according to hydrometeor size compared to the signal's wavelength. Thus the PID algorithm was altered for compatibility with C-band radar (Deierling et al. 2008).
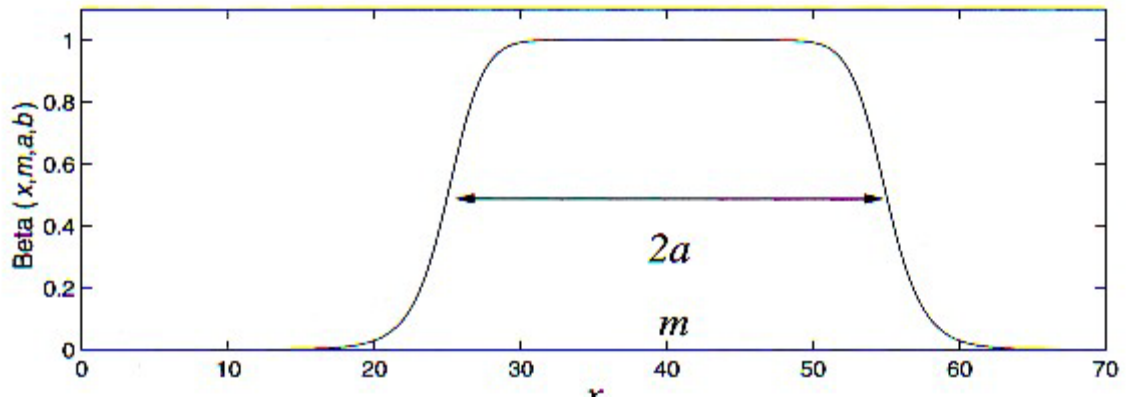
Figure 3.11   Example of a beta membership function for fuzzy logic PID. This
function is for membership of Z_h of rain. The x-axis represents values,
such as Z_h. The width is 2a, while m is the middle value. The probability
of association is b.
[Image credit to Bringi and Chandrasekar, 2001.]

Table 3.3   List of the modified NCAR PID algorithm categories, which contain 17 bulk hydrometeor categories including the indication of insects, clutter and second trip signals.

Category	Color	NCAR PID
1		Cloud
2		Drizzle
3		Light Rain
4		Moderate Rain
5		Heavy Rain
6		Hail
7		Rain and Hail
8		Graupel and Small Hail
9		Graupel and Rain
10		Dry Snow
11		Wet Snow
12		Ice Crystals
13		Irregular Ice Crystals
14		Supercooled Liquid
15		Flying Insects
16		Second Trip
17		Ground Clutter

The PID algorithm utilized the radar variables of reflectivity, differential reflectivity (Z_{DR}), specific differential phase shift (K_{DP}), and correlation coefficient (ρ_{HV}). Each one of these variables contributes to the determination of the associated hydrometeor category. Z_h is one of the variables weighted highest due the influence of particle-size-distribution of the radar volume on the value, assisting in determination between such categories as light rain and hail. $Z_{DR,}$ as described previously, is used to determine the relative oblate shape of a hydrometeor, thus differentiation between large rain drops and hail. K_{DP} assist in determination of the phase and shape of the hydrometeor, such as rain and hail. ρ_{HV} is advantageous in the differentiation of rain and hail and a mixture of the two, due to its response to the phase, size as related to scattering regime, and canting.

The modified fuzzy logic NCAR PID algorithm was utilized in this study for the determination of hydrometeor based on the use of DP variables. The following section will discuss how the PID variables are utilized to forecast lighting initiation. It will cover the development and motivation of the test algorithms implemented and the process of analysis.

Table 3.4   Table of lightning initiation algorithms tested on radar data from the Larsen area of cells of interest. The test column indicates the variables used for the test. The second column contains the various parameters used to compose the algorithms. Each parameter is then paired with each threshold level found in the third column.

Test	Threshold Parameters	Threshold Levels
Z_h and temperature	35, 40, 45 dBZ	-10, -15, -20 °C
Z_h and temperature 2nd Level	15, 20, 25 dBZ (combined with Larsen area requirement)	8 km
Z_{DR} and Z_h with temperature ($Z_h > 40$ dBZ)	> 0.5 dB, > 1 dB, > 4 dB	-10, -15, -20 °C
PID and temperature	$6 < PID > 9$ (any large ice) PID = 8,9 (graupel) $10 < PID > 13$ (small ice) PID = 7, 9, 14 (supercooled drops) PID Small and Large ice	-10, -15, -20 °C

3.5 Test Algorithms

The final step of processing data in this study is to apply the test algorithms. The list of test algorithms can be found in Table 3.4. Each threshold parameter is tested at each threshold level listed in the table to develop thirty-six different test algorithms such as, the first instance of the PID indication of graupel (PID value 8 or 9 as seen in Table 3.3) occurring at -15°C. The test algorithms are derived to be representative of the physical processes involved in the NIC mechanism.   The -10 to -20°C thermal levels are representative of the main charging region in the mixed-phase region as noted in Figure 2.4. The use of 35-45 dBZ radar reflectivity value is used in this study for comparison of results to previous studies conducted (Dye et al. 1986, 1989; Buechler and Goodman 1990; Zipser and Lutz 1994; Roeder and Pinder 1998; Gremillion and Orville

1999; Vincent et al. 2003; Wolf 2006; Yang and King 2010). These values are representative of larger hydrometeors, as suggested by the D^6 weighting of radar reflectivity. The secondary, upper level, threshold was developed as a comparison of previous research and support of the structural development of the thunderstorms (e.g., Dye et al. 1989). The vertical development is indicative of the strength of the updraft and supporting evidence of the ability of cloud scale charge separation. The added requirement of increased reflectivity values is to assist in reducing the false alarm of this test method. It provides evidence of the cell's vertical structure and updraft development (Lhermitte and Krehbiel 1979; Dye et al. 1989; Petersen et al. 1996). It generally accepted and observed that small, weak, warm clouds do not produce significant precipitation required for charge developement leading to first flash (Lhermitte and Krehbiel 1979; Dye et al. 1986, 1989; Williams 1989; Petersen et al. 1996; Gremillion and Orville 1999; Carey and Rutledge 2000; Vincent et al. 2003). Z_{DR} columns, indicative of supercooled drops related to charging, have also been extensively studied in relation to cloud electrification and formation of hydrometers significant to electrification. A Z_{DR} column is a location of enhanced Z_{DR} values (values of Z_{DR} greater than 0.5 dB) associated with high reflectivity values (such as 40-50 dBZ) in the mixed phase region (Jameson et al. 1996; Bringi et al. 1997; Lund et al. 2009). Z_{DR} signatures greater than 0.5 dB are indicative of oblique spheres as is characterized by rain drops, an important ingredient leading to electrification in warm based clouds. As previously discussed, liquid drops lofted or formed above the freezing level will subsequently freeze and form graupel and hail, requirements of NIC particle-to-particle charging. This can be seen in Figure 3.12. Figure 3.12b is an example of a Z_{DR} column of lofted oblate rain

drops, also indicated by PID graupel and rain signature. The freezing of the Z_{DR} column

is seen in Figure 3.12c in the decreased Z_{DR} values and the PID indicates the presence of

graupel and small hail. This test was designed to detect the presence of liquid water in

the mixed phase region of the cloud. The use of 40 dBZ as an associated reflectivity

value is supported by previous research (Carey and Rutledge 2000), as indicative of the

presence of large ice hydrometeors when observed at temperatures below freezing. The

previous methods of first flash forecasting have been previously studied; the use of DP

variables in a comparison has yet to be studied. The PID utilizes and represents the

polarimetric variables in a product that assists the operator in the identification of

hydrometeors. Large and small ice in the presence of liquid water in the mixed-phase

region is required for electrification to occur (MacGorman and Rust 1998). PID is

utilized to determine the presence of significant hydrometeors associated with charging

prior to first lightning flash. The PID categories are grouped into bulk categories

representative of the key hydrometeors they identify related to NIC. For example,

graupel rain mixture and graupel hail mixture PID are grouped to identify "graupel."

Based on the fuzzy logic method of the PID, this grouping aids in decreasing the

ambiguity associated with the hydrometeor categorization, and hence should improve the

accuracy of first flash forecasting with radar.

a) Initial development and first Larsen area signature
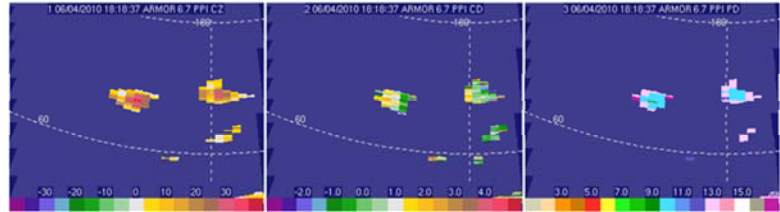
b) Formation of significant precipitation, note graupel and rain indicated in the PID, and the enhanced values of Zdr associated with enhanced Zh values
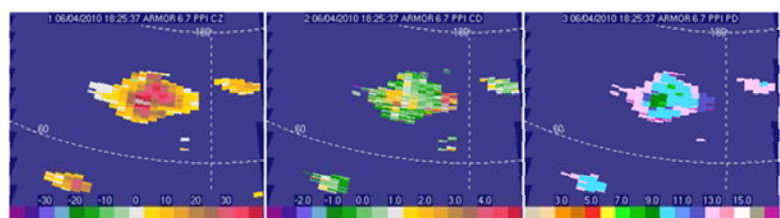
c) The freezing of the Z_{dr} column seen in the decreased Z_{dr} values, PID indicates the presence of graupel and small hail.
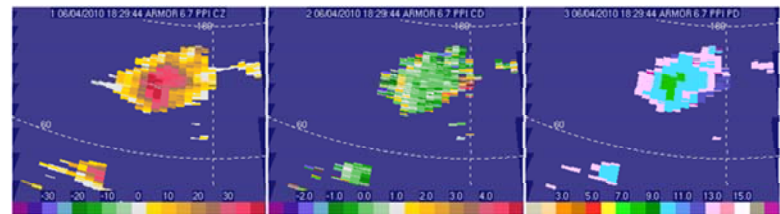
d) A CG flash occurs before the first IC strike at approximately 1837UTC
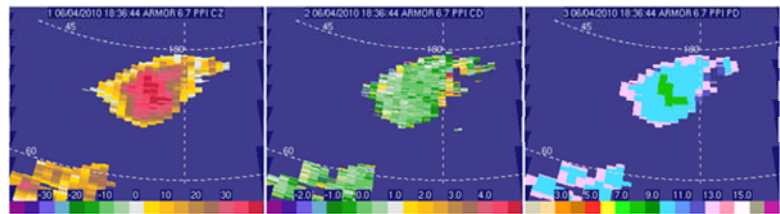
Figure 3.12 Z_h, Z_{DR} and PID evolution of perceptible growth in the thunderstorm cell 1 of case 20100604 at approximately -10°C thermal level. UTC time of each scan: a) 181837, b) 182537, c) 182944, and d) 183644. From left to right, Z_h, Z_{DR} and PID of cell 1 from initial detection of the Larsen Area to first flash. Enhanced Z_h values indicate perceptible sized particles key to the formation of the down draft. Z_{DR} indicates the presence of oblique spheres such as liquid droplets that contribute to precipitation growth. The PID confirms the presence of rain and graupel. See Table 3.3 for PID key.

63

The complete list of algorithms was written into a Fortran 77 program. This program was run against the data sets, outputting polarimetric radar values of Z_h, Z_{DR}, K_{DP} and ρ_{HV} from each cell's defined Larsen area for each test. The program locates the Larsen area of the convective cell and retrieves the data within a .75 km vertical radius of the desired thermal level. The thermal levels in this study are approximately one to two kilometers apart, thus a vertical collection radius ensures the collection of data above and below the thermal levels without excessively over or under sampling the data that could lead to errors in analysis.

The output of the Larsen area data is then analyzed. Analysis of Z_h is based on the maximum value above and below the thermal line (closest height value to the thermal line), then the estimated maximum value of the thermal line is linearly interpolated from these two values. PID analysis is also based on the first instance, or the first occurrence, of the PID signature at the scan level that intersects the thermal height threshold, within reason. This method is also subjected to interpolation. Since PID is based on the bulk, or dominant, hydrometeor signature in the radar volume, care was taken to ensure that the value is representative of the data and not overly sensitive to the presence of noise in the data. Thus, if only one or two PID signatures of interest are located at a height greater than .4 km below the thermal line, then the value is considered to be unrepresentative unless the same PID signature is located in the scan above the thermal line. Z_{DR} is also interpolated within reason in a similar fashion. These values subjected to interpolation were allotted a margin of error as representative of acceptable calibration and attenuation error deviation, $Z_{DR} < 0.2$ dB and $Z_h < 1$dBZ (Ryzhkov et al. 2005).

3.6 Skill Scores

Table 3.5   A contingency table for forecast statistical skill score analysis. For each algorithm result a tally is give to one of four categories, Hit, Miss, False Alarm, or Correct Negative. If a correct forecast is made, then a tally for yes under observed and forecast is added achieving a Hit. If the event is observed but not forecasted, then a tally is marked for observed and no forecast resulting in a Miss.

		Observed	
		Yes	No
Forecasted	Yes	Hit	False Alarm
	No	Miss	Correct Negative

Forecast verification is commonly done through the use of a skill score, or rather a statistical analysis of the ability of a forecast algorithm to correctly forecast or reject the occurrence of an event (Jolliffe and Stephenson 2003). These skill scores are derived from a "yes" or "no" contingency table of four squares. An example of this table is in Table 3.5. For each forecast algorithm, it is determined if the requirements of the algorithm are met for each case. For example, when evaluating a thunderstorm cell, if the algorithm thresholds are met before first flash occurs, it is marked as a positive forecast. If a similar situation occurs with a non-thunderstorm cell, it is tallied as a false alarm. Each skill score has its own strengths and disadvantages (Jolliffe and Stephenson 2003). In this study there are 8 skill scores that were implemented, probability of detection (POD), probability of false alarm (PFA), false alarm ratio (FAR), true skill score (TSS), critical success index (CSI), Heidke skill score (HSS), and operational utility index (OUI). The mean, median and mode lead times were also determined for each test algorithm. The goal of this project is to determine the best operational algorithm for first flash forecasting that would provide significant lead time. The significance of lead time versus skill depends on the desired requirements of a customer. For purposes of this

65

study, mean lead time is considered to be a leading factor in determination of the

optimum algorithm along with POD and PFA in the interest of users such as the NWS.

This section will discuss each skill score, as defined in Jolliffe and Stephenson (2003),

and the importance to this study.

Probability of detection is (POD) a widely used statistic that determines the

likelihood of an event being correctly forecasted. This is determined by the number of

correctly forecasted events, divided by the number of positively occurring events in the

data sample, as in the following equation:

$$POD = \frac{Hit}{Hit + Miss}$$

This number can be deceiving when applied to a small sample number of positive events.

If the sample size is too small, and all events are a miss in forecasting, then the skill

would be zero, and oppositely so for all correct forecasts.

False alarm ratio (FAR) is another commonly used skill score to determine the

accuracy of a forecasting algorithm. FAR is the ratio of falsely forecasted nonevents to

the total number of forecasted events.

$$FAR = \frac{False\ Alarm}{Hit + False\ Alarm}$$

This value is commonly confused with false alarm rate, thus this value is not used for

evaluation purposes in this study. This ratio is used in other skill score values, thus the

inclusion in this study. This value, too, can be skewed for some sample sizes. If the

study consists of many forecasted events with few nonevents, however, all of which were

falsely forecasted, then this value will appear to be small even through the tendency to

forecast a nonevent incorrectly is high.

Probability of false alarm (PFA) is similar to POD. This statistic is usually replaced in many studies by FAR. PFA is the ratio of falsely forecasted thunderstorm events to the total number of non-thunderstorm events.

$$PFA = \frac{False\ Alarm}{False\ Alarm + Correct\ Negative}$$

Much like POD, this ratio can be misleading for a small sample size. Compared to FAR, this compares the accuracy of correctly determining a negative event purely based on the forecasting negative events. This is significant to users who are concerned with the accuracy of non-event forecasting, such as airport forecasters. The excessive forecasting of non-events at an airport can disrupt operations unnecessarily.

True skill score is a value derived to compare the difference of the probability of detection to false alarm rate.

$$TSS = \frac{(FA * CN) - (FA * Miss)}{(FA + Miss) * (FA + CN)}$$

This score was originally derived by C.S. Peirce in 1884 and has since been derived and renamed by other statisticians (Jolliffe and Stephenson, 2003). This value can either be positive or negative with the ideal score of one. If the value is negative one, that is a perfect score for the opposite detection. Such as, if this study calculated the probability of correctly forecasting an event and TSS is -1, then the real conclusion for the algorithm is that it is a perfect predictor for determining the occurrence of non-thunderstorms.

Critical success index measures the skill associated with the correct forecast of an observed event. An event is considered to be observed if it was either forecasted or not forecasted but the event still occurred. Such as, all thunderstorms both correctly and falsely forecasted, plus any occurrence of thunderstorms not forecasted.

$$CSI = \frac{Hit}{(Hit + FA + Miss)}$$

This score takes no value in a correctly forecasted negative event, for this reason it is favored in skill determination of forecasting rare phenomenon. CSI is commonly used by the National Weather Service for forecast verifications, thus the inclusion of this score in this study and discussion.

Heidke Skill Score was originally derived for a contingency table greater than the four binary categories that is applied now. It was not until years later that Doolittle in 1885 converted the score to the four binary categories that is used commonly today (Jolliffe and Stephenson 2003). This skill score considers the difference between correctly forecasted events and the total forecasted events for both observed events and non-observed.

$$HSS = \frac{2[(Hit * CN) - (FA * Miss)]}{[(Hit + Miss)(Miss + CN) + (Hit + FA)(FA + CN)]}$$

This value is ideal for a sample size that contains nearly equally occurring events and nonevents.

Operational utility index is a skill score derived for use by the 45th Weather Squadron at Kennedy Space Center, FL (Roeder 2011, personal communication). This score utilizes a weighted average of POD, FAR, and TSS, each weighted in accordance to their significance to operations at KSC.

$$OUI = \frac{[(3 * POD) + (2 * TSS) + (-1 * FAR)]}{6}$$

An ideal score is 0.83, with a failing score of zero or less.

The mean, median and mode lead times were calculated based upon the time the event was forecasted and the time of the first flash evaluated. The time of the forecast

was determined as the time of the radar sector scan at the elevational angle evaluated for the forecast. If two elevational angle scans were used to evaluate the cell, then the time of the last scan evaluated is the declared forecast time. The lead times are based on all accurately forecasted events.

In conclusion, after the data has been processed and the algorithms applied, the results can be determined. Several steps in the process of evaluating the data are conducted objectively by the operator. This however can still lead to human errors in the process. That in mind, the process of analyzing the data was developed with the thought of a forecast operator conducting similar steps to determine a forecast outcome. Thus, similar errors would be inherent in the operational use of the tool as well.

CHAPTER IV

RESULTS AND DISCUSSION

The onset of lightning occurs in the mature phase of a thunderstorm's cellular

development. This process is seen in the formation of a vigorous updraft with a

downdraft as indicated by enhanced radar reflectivity echo indicative of mm-sized

particles in quantities likely sufficient for significant electrification and lightning as seen

in Figure 4.1. Precipitation loading contributes to the strengthening of the downdraft,

which coupled with the strong updraft, contributes to electrification by charge separation

associated with the NIC mechanism. Z_h values greater than 30 dBZ in Figure 4.1 indicate

mm-sized precipitation of a thunderstorm cell observed in this study capable of

contributing to strengthen a downdraft. Z_{DR} values greater than 0.5 dB in Figure 4.1b

indicate the presence of oblate liquid particles lofted by the updraft, also confirmed by

the PID output. As supported by Figure 4.1, the onset of electrical activity occurs after

the development of significant precipitation lofted to levels above freezing by the updraft,

leading to the development of a significant downdraft.

a) Initial development and first Larsen area signature
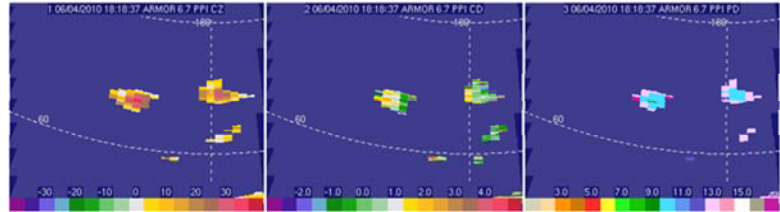
b) Formation of significant precipitation, note graupel and rain indicated in the PID, and the enhanced values of Zdr associated with enhanced Zh values
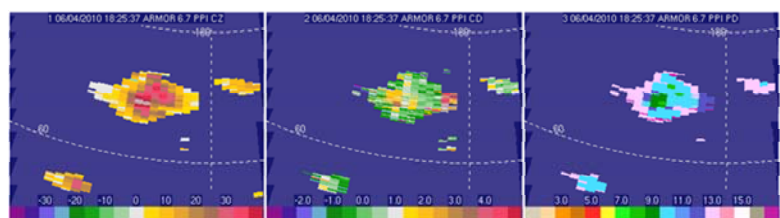
c) The freezing of the Z_{dr} column seen in the decreased Z_{dr} values, PID indicates the presence of graupel and small hail.
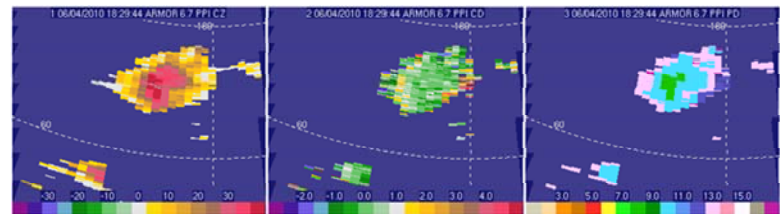
d) A CG flash occurs before the first IC strike at approximately 1837UTC
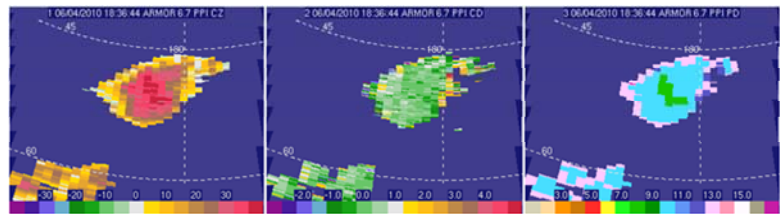
Figure 4.1 Z_h, Z_{DR} and PID evolution of growth in the thunderstorm cell 1 of case 20100604 at approximately -10°C thermal level. UTC time of each scan: a) 181837, b) 182537, c) 182944, and d) 183644. From left to right, Z_h, Z_{DR} and PID of cell 1 from initial detection of the Larsen Area to first flash. Enhanced Z_h values indicate mm-sized particles key to the formation of the down draft. Z_{DR} indicates the presence of oblique spheres such as liquid droplets that contribute to precipitation growth. The PID indicates the presence of rain and graupel. See Table 3.3 for PID key.

a) Initial development and first Larsen area signature
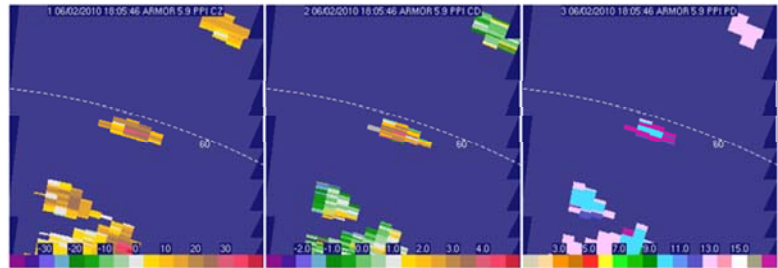
b) Note the lack of significant precipitation formation
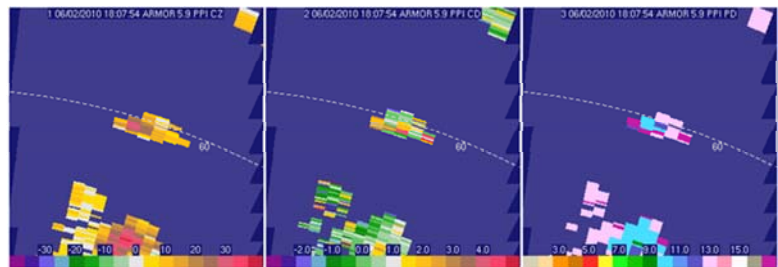
c) The dissipation of the cell, now under the Larsen area signature
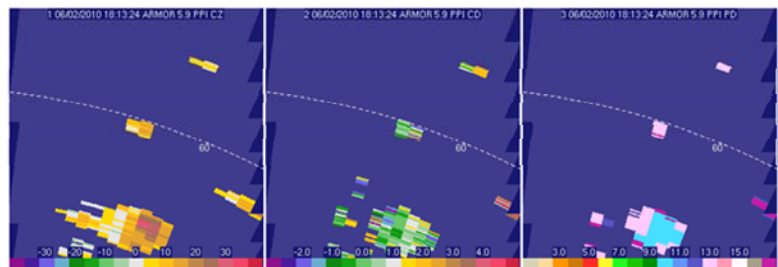
Figure 4.2 Z_h, Z_{DR} and PID evolution of perceptible growth in the non-thunderstorm cell 20 (the cell in the center of the image) of case 20100602 at approximately -10°C thermal level. UTC time of each scan: a) 180546, b) 180754, and c) 181324. From left to right, Z_h, Z_{DR} and PID of cell 20 from initial detection of the Larsen Area to first flash. Lower Z_h values indicate the lack of significant mm-sized particles key to the formation of the down draft. Z_{DR} indicates the lack of significant large charging particles. The PID indicates the lack of graupel or hail particles. See Table 3.3 for PID key.

Based on prior research reviewed earlier, it is assumed cells that do not exhibit

significant development above the freezing level would not achieve first flash.

Observation of non-thunderstorm cells that do not achieve development supporting

Larsen area thresholds supports this assumption. This can be observed in the two non-

thunderstorm cells evaluated from 25 dBZ at -10°C. The evolution of a non-

thunderstorm cell's development is seen in Figure 4.2. As seen in the images, the cell

never achieves precipitation formation supportive of significant charging above the

freezing level. This is seen in the Z_h and PID values. The lack of higher radar

reflectivity values implies the lack of quantities of mm-sized precipitation ice

hydrometeors, such as graupel and hail, and the lack of large quantities of liquid

precipitation that could lead to the formation of precipitation ice. Both of these

observations are confirmed by the PID output values. Unlike the cellular development of

an active thunderstorm as seen in Figure 4.1, this cell does not develop a prominent

precipitation core at levels significant to the NIC mechanism of charging (-10 to -20°C).

In the interest of the operational users concerned in forecasting the first CG flash

only, the algorithms of this study were tested on both the onset of the first flash (either

CG or IC) using NALMA and the first ground flash using the NLDN. The first CG flash

is of interest to operations, such as the NWS, concerned with alerting the general public

about possible lightning hazards. On the other hand, space launch, aviation and airport

operations would be concerned with any possible atmospheric lightning type (IC or CG).

Thunderstorms are indicative of vigorous convection and related hazards, such as

turbulence, icing, hail, lightning, etc., while the concern of CG affects safety of crew and

operations on the ground. Determination of the location and time of the first flash for a

thunderstorm was by graphical analysis of NALMA source data overlaying radar

reflectivity images and confirmed by reference to output from the VHF source to flash

algorithm. The first flash, as indicated by the NALMA, is seen in Figure 3.5. The

multiple sources support the indication of a flash opposed to environmental noise, as

confirmed by reference to time and location in NALMA flash algorithm output. As

discussed in further detail in Chapter Three, the VHF source to flash algorithm outputs

the time and location of the first source in a flash while filtering noise from the NALMA

source data. Indication of CG initiation is based upon NLDN flash data. CG lightning

location is displayed in Figure 3.6 as indicated by the asterisks. The first ground flash

typically occurs some time after the onset of thunderstorm activity. MacGorman et al.

(2011) found in the High Plains, Oklahoma, and north Texas regions that a thunderstorm

produces a CG flash thirty minutes after the first onset of IC activity about 50% of the

time. The average time difference between an IC flash and a CG flash in this study is

approximately three and half minutes. Only four of the thirty-one thunderstorm cells (or

13%) never produce a ground flash.

      For ease of progression, the results will be discussed by section, thunderstorm

forecasting and CG forecasting. Within these sections, the test algorithms too will be

reduced to sections discussing the bench mark algorithm, tests of basic radar reflectivity,

Z_h and Z_{DR} techniques, the utilization of PID, and concluded with a section that compares

the best of each test category. The chapter will culminate with a section that discusses

the difference in performance of the algorithms tested for forecasting thunderstorms and

CG events.

4.1 Thunderstorm Forecasting

4.1.1 The Bench Mark

Based on previous studies, the control test algorithm is 40dBZ at -10°C (Dye

et al. 1989; Buechler and Goodman 1990; Gremillion and Orville 1999; Vincent et al.

2003; Wolf 2006; Yang and King 2010). The benchmark algorithm is used to determine

if another algorithm proves to be more advantageous than that which is typically

implemented. The results for basic radar reflectivity at thermal thresholds in forecasting

thunderstorms can be seen in Table 4.1. The bench mark results in a perfect 100% POD,

meaning that the use of this algorithm will detect the onset of lightning with high

precision. It is possible, if this test was ran on a larger sample size the POD would be

less. However, Buechler and Goodman (1990) also found their radar reflectivity based

lightning detection algorithm of 40dBZ at -10°C to have a perfect POD for the data set of

20 cells they tested. The PFA is also high, over 0.40. The FAR of thunderstorm

detection is about 0.20, which is comparative to similar studies (Buechler and Goodman

1990). Some may find this acceptable accounting for the moderately high lead time of

ten and a half minutes for the first lighting flash. However, in comparison to the other Z_h

based thunderstorm algorithms in this study, the larger PFA (e.g., > 0.20) leads to a lower

confidence in accurately forecasting a nonoccurrence of the event. This becomes a cost

to benefit concern. A perfect score in OUI is 0.83, and the bench mark achieves a lower

skill of 0.66. The CSI of about 0.80 is considered to be acceptable skill and is

comparable to other studies concluding the bench mark to be the ideal algorithm

(Buechler and Goodman 1990; Gremillion and Orville 1999; Wolf 2007).

Table 4.1   Radar reflectivity and thermal threshold algorithm skill scores for 31 thunderstorm cases and 19 non-thunderstorm cases from 8 case dates. Skill scores include, probability of detection (POD), probability of false alarm (PFA), false alarm ratio (FAR), true skill score (TSS), operational utility index (OUI), critical success index (CSI), Heidke skill score (HSS), and lead time (LT) mean, median and mode. The first column indicates the forecasting algorithm associated with each score set.

	POD	PFA	FAR	TSS	OUI	CSI	HSS	LT Mean	LT Med.	LT Mode
35 dbz at -10°C	1	0.526	0.244	0.474	0.617	0.756	0.527	12.50	9	9
40 dbz at -10°C	1	0.421	0.205	0.579	0.659	0.795	0.630	10.50	8	7
45 dbz at -10°C	0.968	0.158	0.091	0.810	0.739	0.882	0.827	10.00	7	7
35 dbz at -15°C	1	0.105	0.061	0.895	0.788	0.939	0.913	9.50	8	11
40 dbz at -15°C	1	0	0	1	0.833	1	1	8.00	6.5	8
45 dbz at -15°C	0.903	0	0	0.903	0.753	0.903	0.876	5.00	4	4
35 dbz at -20°C	0.968	0.053	0.032	0.915	0.783	0.937	0.915	5.00	4.5	4.5
40 dbz at -20°C	0.903	0	0	0.903	0.753	0.903	0.876	4.00	4	2
45 dbz at -20°C	0.516	0	0	0.516	0.430	0.516	0.448	2.00	2	2
30 dBZ at -10°C and 15 dBZ above 8 km	0.968	0.210	0.118	0.757	0.717	0.857	0.781	10.50	7	6.5
30 dBZ at -10°C and 20dBZ above 8 km	0.968	0.158	0.091	0.810	0.739	0.882	0.827	9.00	7	4
30 dBZ at -10°C and 25dBZ above 8 km	0.968	0.105	0.062	0.862	0.761	0.909	0.871	7.50	6	4

4.1.2 Basic Radar Reflectivity, Z_h

The best method of detection of lightning initiation using classical methods of forecasting, reflectivity thresholds at a specific temperature threshold, is 40 dBZ at -15°C. The results of this algorithm are far better than that of the bench mark. Based on the sample set in this study, the algorithm results in perfect detection, 1.0 POD and 0 PFA and FAR, as seen in Table 4.1, for thunderstorm forecasting. This results in a perfect score for skill by all methods of analysis. Once again, this algorithm would likely result in a different conclusion if applied to a larger data set. However, it would likely still be a leading algorithm in skill scores. The average lead time associated with this

algorithm is eight minutes which is relatively low. The median of about 6.5 minutes lead

time is slightly off-set from the mean due to the elongated nature of the tail of the

non-Gaussian curve created by the occurrence of larger lead times. The lead time

distribution curves are examined in Appendix A, which also contains graphs of

significant algorithms. Previous research (Vincent et al. 2004) has produced lead time up

to seventeen and a half minutes, although still comparable to algorithms producing near

ten minutes lead time. The sacrifice of forecasting confidence can yield greater average

lead times. Depending on the user's requirements, another algorithm could be found in

greater favor. For the purposes of evaluation in this study, the focus of the best algorithm

is a balance between a strong average lead time and confident POD and PFA resulting in

the favor of 40 dBZ at -15°C algorithm, as discussed further below.

It is notable the general trend of decrease in POD and lead time associated with an

increase in requirements. This is an expected result. The greater the threshold required

to achieve a "hit", such as 45 dBZ, requires the cell to achieve a greater level of

development, thus decreasing lead time. Achieving a greater level of development is also

less likely to occur in the weak cells observed in this study. These expectations were

confirmed in the general trend in the results. For example, the 35 dBZ at -10°C

algorithm had the greatest lead times, an average of 12.5 and median of 9 minutes. While

these are the highest lead times of the reflectivity based algorithms, it is also associated

with the greatest PFA, 0.53.

The implementation of a secondary reflectivity threshold at a level significant to

development does provide a small margin of added confidence to an algorithm. As

discussed previously, this second level ensures the vertical development of the

thunderstorm. The best secondary level applied in this study to use is 15 dBZ above 8 km associated with the Larsen area (30 dBZ at -10°C) as seen in Table 4.1. The POD for all the algorithms requiring a secondary reflectivity threshold has a high POD of 0.97 for thunderstorm forecasting. The identical POD for all three algorithms is a result of the fact that all the thunderstorms that develop above 8 km and exhibit particle development of 15 dBZ continues to develop to at least 25 dBZ as seen in Figure 4.3. This does prove that the storms exhibit development conducive to charging. Even so, in comparison to the bench mark, the POD is less. On the other hand, the error of false detection is less than the bench mark by about half for both PFD and FAR achieving values of 0.21 and 0.12, respectively. Examining the skill associated results with OUI, attaining a score of 0.72; it is on the lower edge of acceptability. This is also true of CSI, a value of 0.86 is considered on the positive side of acceptability. The average lead time is comparable to that of the benchmark, ten and a half minutes. The mean lead time result is slightly skewed by the occurrence of outlying lead times. However, the median and modal lead times of the 15 dBZ above 8 km algorithm, 7 and 6.5 minutes respectively, are less than those of the bench mark, 8 and 7. Higher reflectivity levels, such as 20 and 25 dBZ, have a small margin of greater confidence of nonevent determination; however the added requirement reduces the average lead time with increased threshold requirements, as expected. Thus the lower requirement (i.e., 15 dBZ above 8 km) with greater average lead time is the best algorithm of this group for any lightning onset predictions. Compared to the bench mark, the secondary requirement, 15 dBZ above 8 km, provides a small improvement, only improves the PFA and matches lead time with a small reduced POD. The skill of the secondary level in comparison is also greater; this is reflective of

78

the improvement in FAR. In comparison to the best single level reflectivity threshold, 40 dBZ at -15°C, the secondary level provides two and a half more minutes in average lead time at the small exchange of confidence and skill. Some industries, such as consulting forecasters for large outdoor venue events, might find the decrease in skill an acceptable exchange for greater lead time.
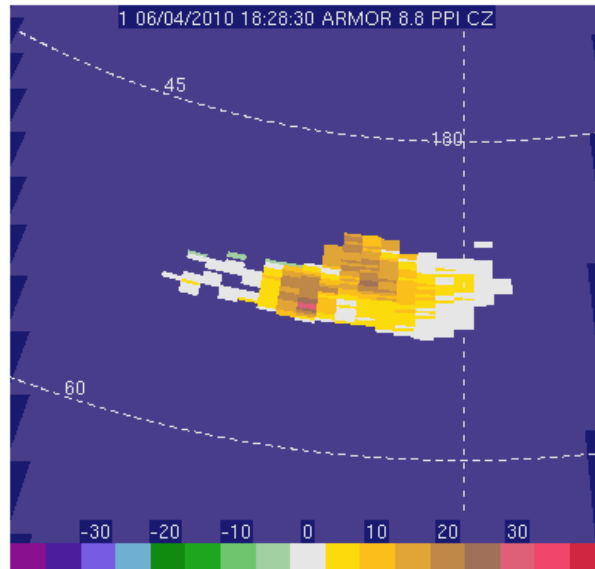
Figure 4.3   Reflectivity thresholds above 8 km for cell 1 of case 20100604. Cell's height is approximately 8.5 km.
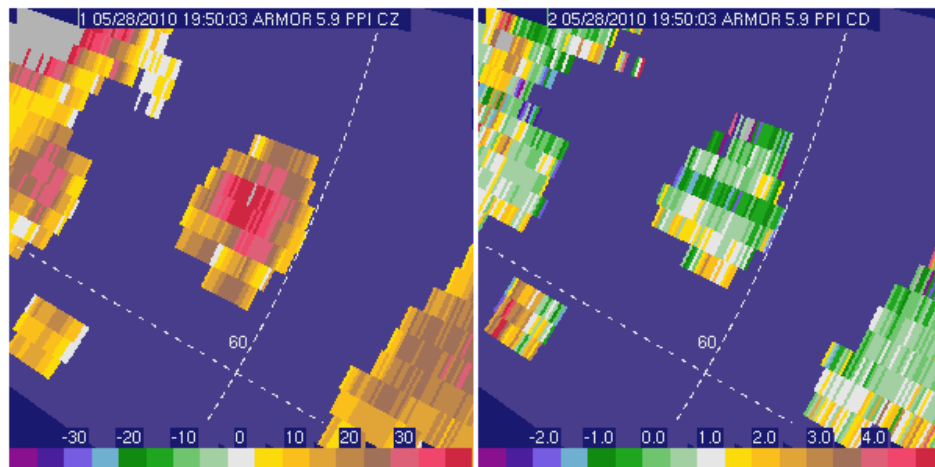
Figure 4.4   Weak Z_{DR} column of Cell 8 from case 20100528 at approximately 6.29 km, about -13°C. Z_{DR} values associated with Z_h>40 dBZ, are less than 1dB but greater than 0.5 dB.

4.1.3 Z_{DR} Column

Forecasting the onset of lightning by the determination of supercooled rain drops located in the Z_{DR} column using polarimetric variables of Z_h and Z_{DR} provides improvement in skill associated with reduced false alarm. The best algorithm for detection of a Z_{DR} column is the detection of 1dB relative oblique particles associated with 40 dBZ at -10°C; refer to Figure 2.10 for an example. The majority of thunderstorm cells containing an updraft capable of lofting liquid particles 0.5 dB in relative size at high concentrations represented in 40 dBZ echo is also capable of lofting particles over 1 dB. Only one thunderstorm cell, cell 8 from case date 20100528, was not capable of such. This cell is seen in Figure 4.4. While reflectivity values exceed 40 dBZ, associated values of Z_{DR} do not exceed 1 dB. A note of interest; this cell is one of the four cells that did not develop a CG flash as indicated by NLDN. Furthermore, the algorithm of 1 dB or greater and 40 dBZ at -10°C has an accuracy of 0.93 POD and 0.16 PFA associated with moderate values of CSI and OUI, 0.85 and 0.71 respectively. The average lead time related to this method is 11 minutes. The average is approximately three minutes greater than the median and modal lead times, offset by the occurrence of three cells with lead times greater than 30 minutes. The average lead time is a half minute more than the bench mark with a small sacrifice to POD and an increase in confidence of false alarm mitigation. If the forecasting operator is more concerned with confidence of the forecast, then the bench mark with a 1.0 POD is still a strong algorithm. Although, to allot a margin of error in POD while decreasing FAR and increasing mean lead time, the use of the Z_{DR} column 1 dB at -10°C algorithm is advantageous. As expected, the detection of

the Z_{DR} column declines the greater the altitude requirement becomes. The storm must have a strong updraft to successfully loft large rain drops to high altitudes before they freeze. The storms in this study are relatively weak storms that do not generally demonstrate such development. The detection of smaller particles 0.5 dB or greater has nearly the same lead times and a very slightly better POD, the PFA is nearly doubled also thus nearly halving scores such as HSS and OUI. Though the PFA is still small for 0.5 dB particles, the confidence difference with little sacrifice to other performance variables makes the 1 dB or greater algorithm more ideal.

Table 4.2   Bench mark and Z_{DR} column forecasting algorithm skill scores for 31 thunderstorm cases and 19 non-thunderstorm cases from 8 case dates. Skill scores include, probability of detection (POD), probability of false alarm (PFA), false alarm ratio (FAR), true skill score (TSS), operational utility index (OUI), critical success index (CSI), Heidke skill score (HSS), and lead time (LT) mean, median and mode. The first column indicates the forecasting algorithm associated with each score set.

	POD	PFA	FAR	TSS	OUI	CSI	HSS	LT Mean	LT Med.	LT Mode
40 dBZ at -10°C	1	0.421	0.205	0.579	0.659	0.795	0.630	10.50	8	7
Z_{dr} >0.5 dB and 40 dBZ at -10°C	0.968	0.316	0.167	0.65	0.673	0.811	0.687	11.00	7.5	4
Z_{dr} >0.5 dB and 40 dDB at -15°C	0.87	0	0	0.87	0.726	0.87	0.837	6.50	4	4
Z_{dr} >0.5 dB and 40 dDB at -20°C	0.742	0	0	0.742	0.618	0.742	0.686	3.00	4	5
Z_{dr} >1 dB and 40 dBZ at -10°C	0.935	0.158	0.094	0.778	0.711	0.853	0.786	11.00	7	7
Z_{dr} >1 dB and 40 dBZ at -15°C	0.806	0	0	0.806	0.67	0.806	0.76	6.50	4	4
Z_{dr} >1 dB and 40 dBZ at -20°C	0.323	0	0	0.323	0.269	0.3226	0.266	2.00	0.5	0.5
Z_{dr} >4 dB and 40 dBZ at -10°C	0.645	0.105	0.091	0.540	0.487	0.606	0.495	7.50	7	7
Z_{dr} >4 dB and 40 dBZ at -15°C	0.258	0	0	0.258	0.215	0.258	0.209	5.50	4	4
Z_{dr} >4 dB and 40 dBZ at -20°C	0	0	0	0	0	0	0	0.00	0	0
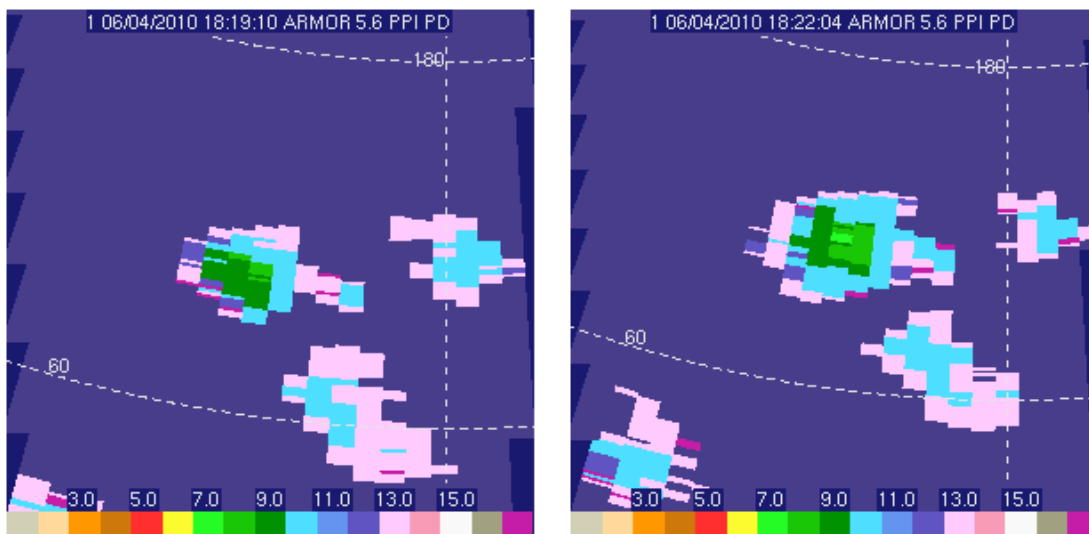
Figure 4.5   PID signatures in cell 1 of 20100604 near -10°C. This scan height is approximately 5.73 km at about -8.5°C. Left) Demonstrates the first instance of graupel. Right) Shows the occurrence of significant hail development. See Table 3.3 for PID key.

4.1.4 PID

Each PID algorithm was derived to detect the presence of precipitation related to the particle-to-particle NIC mechanism and hence the likelihood of lightning. To recap from Chapter II, this process involves the interactions of large ice hydrometeors such as graupel and hail interacting with smaller ice particles such as ice crystals in the presence of liquid cloud water at altitudes above the freezing level. The algorithms derived for the purpose of this study determine the first presence of large hydrometeors, graupel, small ice crystals, supercooled drops, and a combination of small and large ice hydrometeors simultaneously. As seen in Table 4.3, the best algorithm of all these tests is the detection of the bulk PID category of graupel. An example of the positive detection of the first instance of graupel is seen in Figure 4.5 (left). Table 4.3 shows that this algorithm has skill scores identical to the other algorithms of large ice and the simultaneous occurrence of small and large ice hydrometeors. These algorithms include the presence of graupel

which is the first large ice hydrometeor to be detected by the PID.   The bulk category of large ice consists of the PID output for hail and graupel. Hail is a larger ice form than graupel and may form by riming graupel particles. Thus, it is possible that the formation of hail would not occur until after the formation of graupel. This is seen in the data in this study. Figure 4.5 demonstrates the occurrence of graupel and the later detection of hail by the PID. Hail, a larger and heavier hydrometeor, must also be supported by a greater updraft. Thus it is further less likely to be the first large ice form detected by the PID. Unlike larger ice hydrometeors, small ice crystals do not require a significantly strong updraft to sustain the lofted particles above the freezing level. Non-thunderstorms, such as the one in Figure 4.2, are capable of this process. This is seen in the results in Table 4.3. The detection of small ice particles has a perfect POD as well as a high PFA, 1.0 to over 0.5. The increased FAR is seen in parallel to the decrease of the skill score results. The small ice PID algorithm only consistently exceeds the benchmark in mean lead time, 14.5 to 12.5 minutes. The lead time of the small ice algorithm is biased by the occurrence of greater than average lead times, evident by the median values, 12 to 9, and mode, 6.5 to 8.5. The lead time histograms examined in Appendix A shows the lead time distribution that causes this bias. The detection of small ice has a lead time mode near that of the benchmark with approximately 7 minutes except at -15°C, in which small ice exceeds the bench mark by a minute and a half. The exchange of the increased lead time for the decrease of confidence could be found by some as an acceptable exchange; however the excessive PFA and low CSI, 0.62 to 0.74, would not be considered acceptable to others, such as the NWS, concerned with both time and accuracy. Operations which repeatedly produce false alarms can become ineffective to the populace

who could grow desensitized and complacent to the notice. The first detection of supercooled drops is dominated by the occurrence of PID 9, graupel rain mix. Thus, the skill of POD and PFA are generally less than if forecasting based on the identification of bulk category graupel. The lead times between these two methods are similar as well. At -10°C, the POD for supercooled drops is 0.97 which is less than 1.0 POD for graupel. However, there is an advantage of decreased PFA, 0.26 opposed to graupel's 0.37.   At lower temperatures, graupel PID generally exceeds supercooled drops in all skill scores and average lead time. However, it does well at -10°C in comparison to the bench mark. Supercooled drops mean lead time is a minute more with reduced PFA and increased CSI and OUI skill, 0.83 and 0.69.

Table 4.3   Bench mark and PID algorithm skill scores for 31 thunderstorm cases and 19 non-thunderstorm cases from 8 case dates. Skill scores include, probability of detection (POD), probability of false alarm (PFA), false alarm ratio (FAR), true skill score (TSS), operational utility index (OUI), critical success index (CSI), Heidke skill score (HSS), and lead time (LT) mean, median and mode. The first column indicates the forecasting algorithm associated with each score set. PID between 6 and 9 are associated with large ice forms. PID 8 and 9 are associated with the presence of graupel. 10 to 13 is related to small ice in PID. Supercool drops are represented in the PID values of 7, 9 and 14. Reference Table 3.3 for PID values.

	POD	PFA	FAR	TSS	OUI	CSI	HSS	LT Mean	LT Med.	LT Mode
40 dBZ at -10°C	1	0.421	0.205	0.579	0.659	0.795	0.630	10.50	8	7
Large Ice										
6<PID>9 at -10°C	1	0.368	0.184	0.632	0.680	0.816	0.680	11.50	9	9
6<PID>9 at -15°C	0.935	0.053	0.033	0.883	0.756	0.906	0.874	9.50	7.5	3.5
6<PID>9 at -20°C	0.903	0.053	0.034	0.851	0.729	0.875	0.834	4.00	4	0.5
Graupel										
8,9 at -10°C	1	0.368	0.184	0.632	0.680	0.816	0.680	11.50	9	9
8,9 at -15°C	0.935	0.053	0.033	0.883	0.756	0.906	0.874	9.50	7.5	3.5
8,9 at -20°C	0.903	0.053	0.034	0.851	0.729	0.875	0.834	4.00	4	0.5
Small Ice										
10<PID>13 at -10°C	1	1	0.38	0	0.437	0.62	0	14.50	12	6.5
10<PID>13 at -15°C	1	0.737	0.311	0.263	0.536	0.689	0.307	13.50	9	8.5
10<PID>13 at -20°C	1	0.579	0.262	0.421	0.597	0.738	0.474	12.50	9	6.5
Supercooled Drops										
7,9,14 at -10°C	0.968	0.263	0.143	0.705	0.695	0.833	0.734	11.50	9	9
7,9,14 at -15°C	0.871	0.053	0.036	0.818	0.702	0.844	0.794	7.00	6.5	4
7,9,14 at -20°C	0.710	0	0	0.710	0.591	0.710	0.650	3.00	4	5
Small and Large Ice										
6<PID>9 and 10<PID>13 at -10°C	1	0.368	0.184	0.632	0.680	0.816	0.680	11.50	9	9
6<PID>9 and 10<PID>13 at -15°C	0.935	0.053	0.033	0.883	0.756	0.906	0.874	9.50	7.5	3.5
6<PID>9 and 10<PID>13 at -20°C	0.903	0.053	0.034	0.851	0.729	0.875	0.834	4.00	4	0.5

The best algorithm in the test category of graupel detection is the first instance of the bulk category of graupel PID at -15°C. Detection of graupel at lower heights, -10°C, produces results that are better than the bench mark; however detection at -15°C has a reduced PFA. Graupel PID at -10°C has a perfect POD, the same as the bench mark. It also results in a PFD and skill better than the bench mark, 0.37 PFD, 0.68 OUI, 0.82 CSI and 0.68 HSS. The mean lead time of graupel PID at -10°C is 11.5 minutes, a minute greater than the bench mark and two minutes more than at -15°C. The average lead time of both levels are offset from the median by the occurrence of greater lead times. Graupel PID at -15°C has a POD, 0.93, less than that of -10°C with a PFA, 0.05, which is far less as well. In comparison to the bench mark, the average lead time is only short a minute while the PFA is far less than 0.42. This improvement in forecasting confidence at the cost of a minute in average lead time would likely be found to be an acceptable exchange by many operators such as those at KSC who are concerned with lead time and accuracy, particularly POD, of forecast.

4.1.5 Comparison of Thunderstorm Forecasting Techniques

Of all the algorithms discussed in the previous sections the best algorithm is 40 dBZ at -15°C. This algorithm is statistically perfect when tested on the fairly small data set examined in this study. This test also produces a relatively low mean lead time of 8 minutes. If a marginal error in forecasting confidence is found acceptable by the operator, then the better algorithm would be found by use of the first detection of graupel at -15°C by PID algorithm due to an increase of 3.5 minutes lead time. OUI and CSI

associated to the first instance of PID graupel is 0.76 and 0.91; this is better than 0.66 and 0.79 associated with the bench mark but less than perfection of 40 dBZ at -15°C.   Thus, with the increased mean lead time, it is proven that even though the use of the PID falls short to other radar reflectivity algorithms in skill, it does improve lead time at a marginal sacrifice of skill. This demonstrates the potential value of DP radar data.

4.2 Cloud-to-Ground Forecasting

4.2.1 The Bench Mark

The bench mark for CG forecasting is the same as that used for thunderstorm forecasting, 40 dBZ at -10°C (Dye et al. 1989; Buechler and Goodman 1990; Gremillion and Orville 1999; Vincent et al. 2003; Wolf 2006; Yang and King 2010). The benchmark algorithm is used to determine if another algorithm proves to be more advantageous than that which has already been implemented. The results of the bench mark algorithm and other radar reflectivity based algorithms can be found in Table 4.4. The bench mark of CG forecasting results in 1.0 POD and a high PFA of 0.52. The FAR of 0.31 is a relatively higher value and results in skill scores just as moderate, 0.48 TSS, 0.61 OUI and 0.69 CSI. The FAR and CSI values are also consistent with the finding from previous studies, such as Vincent et al. (2003). The mean lead time of 14 minutes is comparatively just as good as previous research. This value is influenced by the occurrence of the mode at 10 minutes and a secondary lead time histogram peak at 22 minutes. As mentioned when examining the bench mark of thunderstorm forecasting, it is just as likely that a larger data set could result in a less than perfect POD.

Table 4.4   Radar reflectivity and thermal threshold algorithm skill scores for 27 thunderstorm cases producing cloud to ground flashes and 23 non-CG storm cases from 8 case dates. Skill scores include, probability of detection (POD), probability of false alarm (PFA), false alarm ratio (FAR), true skill score (TSS), operational utility index (OUI), critical success index (CSI), Heidke skill score (HSS), and lead time (LT) mean, median and mode. The first column indicates the forecasting algorithm associated with each score set.

	POD	PFA	FAR	TSS	OUI	CSI	HSS	LT Mean	LT Med.	LT Mode
35 dbz at -10°C	1	0.609	0.341	0.391	0.573	0.658	0.410	15.50	11.75	6
40 dbz at -10°C	1	0.522	0.308	0.478	0.608	0.692	0.497	14.00	10.5	10
45 dbz at -10°C	1	0.261	0.182	0.739	0.716	0.818	0.754	13.00	10.5	5
35 dbz at -15°C	1	0.261	0.182	0.739	0.716	0.818	0.754	12.50	10.5	6
40 dbz at -15°C	1	0.174	0.129	0.826	0.754	0.871	0.837	11.00	10.5	6
45 dbz at -15°C	1	0.087	0.069	0.913	0.793	0.931	0.919	7.50	6.5	7.5
35 dbz at -20°C	1	0.174	0.129	0.826	0.754	0.871	0.837	7.50	6	6
40 dbz at -20°C	0.963	0.087	0.072	0.876	0.762	0.896	0.879	7.00	6	6
45 dbz at -20°C	0.593	0.043	0.059	0.549	0.469	0.571	0.532	3.50	4	4
30 dBZ at -10°C and 15 dBZ above 8 km	0.963	0.348	0.235	0.615	0.647	0.743	0.629	14.00	9	8
30 dBZ at -10°C and 20dBZ above 8 km	0.963	0.304	0.212	0.659	0.666	0.765	0.672	13.00	9	6
30 dBZ at -10°C and 25dBZ above 8 km	0.963	0.261	0.187	0.702	0.684	0.788	0.714	10.50	9	6

4.2.2 Basic Radar Reflectivity, Z_h

Based on PFA and mean lead time, the best Z_h method of detection of CG lightning initiation implementing reflectivity thresholds at a specific temperature threshold is 40 dBZ at -15°C. The best reflectivity based CG forecasting algorithm does not have the best FAR or PFA, values of 0.13 and 0.17 respectively, which is double the values associated with the algorithm of 45 dBZ at -15°C, as can be noted in Table 4.4. These two algorithms have identical POD at 1.00. The difference that makes the use of 40 dBZ the better algorithm is the average lead time of eleven minutes. These two algorithms, 40 and 45 dBZ at -15°C, also vary in associated skill scores, CSI, OUI, HSS and TSS by 0.5 - 0.10. Although with the allowance of a marginally greater false alarm, 40 dBZ at -15°C has a greater mean lead time. The results of this algorithm are even better than that of the bench mark. The average lead time is comparable to previous studies (Gremillion and Orville 1999). The median lead time of 40 dBZ at -15°C is 10.5 minutes, nearly that of the mean lead time. However, the histogram is characterized by a non-normal distribution curve, with a slight bias caused by a single outlying value as discussed in the Appendix. The sacrifice of forecasting confidence can yield greater lead times, so depending on the user's requirements another algorithm could be found in greater favor as previous discussed.

The implementation of a secondary reflectivity threshold at a level significant to development does provide a small margin of added confidence to an algorithm. As discussed previously, this second level ensures the vertical development of the thunderstorm. The best level applied in this study to use is 15 dBZ above 8 km associated with the Larsen area (30 dBZ at -10°C). The POD for all the algorithms

requiring a secondary reflectivity threshold is 0.96. This value is less than the perfect POD of the benchmark. The PFA and FAR of the algorithm is 0.35 and 0.23, respectively, which too is less than the bench mark values of 0.52 and 0.31, respectively. The lead time is also identical to that of the benchmark with an average of 14 minutes. Higher reflectivity levels, such as 20 and 25 dBZ, have a small margin of greater confidence of nonevent determination; however, the added requirement reduces the lead time with increased requirements, as expected. Thus the lower reflectivity requirement of 15 dBZ with greater mean lead time is the best algorithm of this group for CG onset predictions. In comparison to the bench mark, it only improves the PFA, thus improving the skill scores such as OUI, CSI and HSS, and matches the average lead time with a reduced POD. At the cost of confidence, the use of a secondary level does provide a margin of three minutes average lead time. This is a result of the lower requirement for initial Z_h threshold at -10°C. As seen in the reflectivity evolution of a cell in Figure 4.6, as is typical of the cells in this study, and others, the lower reflectivity threshold at the lower level (Figure 4.6 a and b) is met before the more intense higher precipitation radar signatures are achieved at higher levels (Figure 4.6c).

a) Initial development at -10 and -15°C.

b) Continued development at -10 and -15°C, as evident by increased reflectivity at the upper level.

c) Continued development at -10 and -15°C, as evident by increased reflectivity at the upper level now exceeding 40 dBZ.
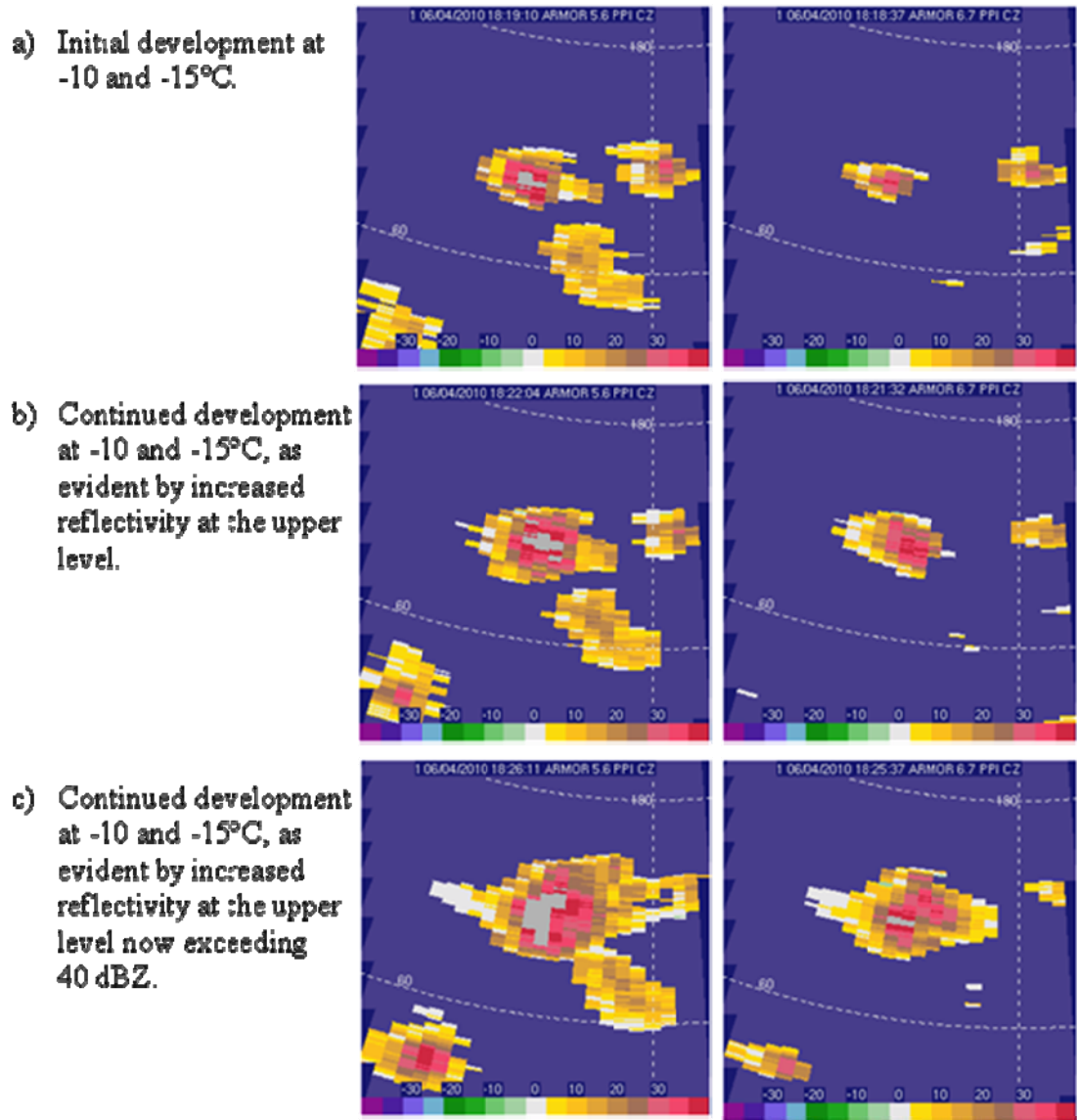
Figure 4.6   Evolution of reflectivity of cell 1 of 20100604 at approximately -10 and -15°C. The left column is the cell at approximately -10°C, and the right column is the cell at approximately -15°C. The evolution demonstrates the evolution in precipitation formation and updraft lofting.

Depending on the requirements of the user, the best radar reflectivity algorithm is 15 dBZ above 8 km associated with the Larsen area (30dBZ at -10°C) for a strong average lead time of 14 minutes at the sacrifice of some forecasting confidence. A consumer such as a baseball stadium owner might find the lack of confidence a fair exchange for greater average lead time allotting more time for weather preparations.

4.2.3 Z_{DR} Column

Forecasting CG onset by the determination of supercooled rain drops using polarimetric variables of Z_h and Z_{DR} also produce similar results for both thunderstorm onset and CG forecasting. The best algorithm for detection of a Z_{DR} column is the detection of 1dB sized particles associated with 40 dBZ at -10°C. The detection of the Z_{DR} column declines the greater the altitude requirement becomes. The storm must have a strong updraft to successfully loft large liquid particles to high altitudes before they freeze. The storms in this study are relatively weak storms that do not generally demonstrate such development. The detection of smaller particles 0.5 dB or greater has the same mean lead time and a very slightly better POD, the PFA is nearly doubled at 0.43. Z_{DR} of 0.5 dB skill scores, 0.61 OUI and 0.70 CSI, are less than those of 1 dB, 0.68 OUI and 0.79 CSI. Since there is almost no sacrifice to mean lead time in the difference between the larger and smaller rain drop, the 1 dB associated algorithm is the more ideal predictor. The median lead time values for all Z_{DR} column algorithms follow a similar trend to that of the mean lead time, decreasing with increasing requirements and are non-Gaussian with secondary modal peak times. Furthermore, it was found all cells that are capable of lofting 0.5 dB relative sized particles are capable of lofting 1 dB rain

drops in this study. The cells of this study are relatively weak, and none of the cells

included in this data set were able to loft large oblate liquid particles of 4 dB to levels

associated with -20°C, which is approximately 8 km. This was an expected result. A

4 dB particle is a rather large and oblate, and a strong updraft is needed to loft a particle

of that size well above the freezing level while maintaining a liquid state. Figure 4.7

shows a typical thunderstorm cell in this study at approximately -20°C. Even though

0.96 of the storms develop to the extent and intensity of 40 dBZ at that level, by the time

the cell develops to this intensity, the hydrometeors have frozen.
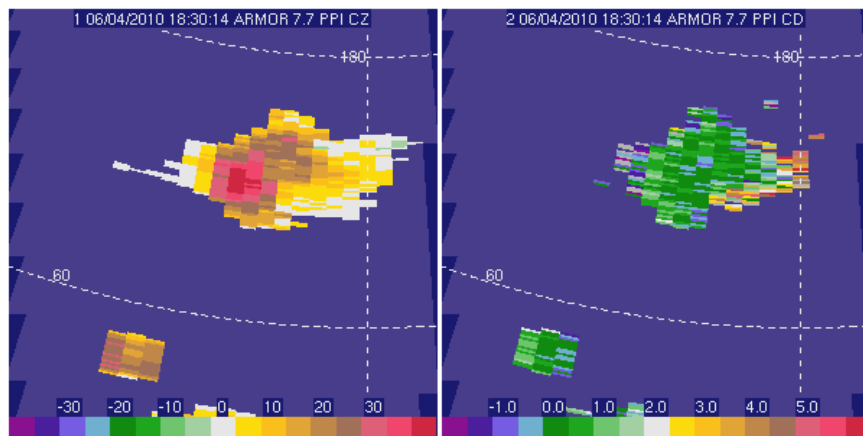
Figure 4.7 Z_{DR} and Z_h of cell 20100604 at approximately -20°C, and height of
7.4 km. The lack of large oblate hydrometeors at this level is typical and
expected for weak pulse type storms as in this study.

Table 4.5   Bench mark and Z_{DR} column forecasting algorithm skill scores for 27 thunderstorm cases producing cloud to ground flashes and 23 non-CG storm cases from 8 case dates. Skill scores include, probability of detection (POD), probability of false alarm (PFA), false alarm ratio (FAR), true skill score (TSS), operational utility index (OUI), critical success index (CSI), Heidke skill score (HSS), and lead time (LT) mean, median and mode. The first column indicates the forecasting algorithm associated with each score set.

	POD	PFA	FAR	TSS	OUI	CSI	HSS	LT Mean	LT Med.	LT Mode
40 dBZ at -10°C	1	0.522	0.308	0.478	0.608	0.692	0.497	14.00	10.5	10
Z_{dr} >0.5 dB and 40 dBZ at -10°C	0.963	0.435	0.278	0.528	0.611	0.703	0.544	14.50	11	6.5
Z_{dr} >0.5 dB and 40 dDB at -15°C	0.889	0.130	0.111	0.758	0.679	0.800	0.758	10.00	7	4.5
Z_{dr} >0.5 dB and 40 dDB at -20°C	0.741	0.130	0.130	0.610	0.552	0.667	0.602	6.00	5	5
Z_{dr} >1 dB and 40 dBZ at -10°C	0.963	0.261	0.187	0.702	0.684	0.788	0.714	14.50	11	6.5
Z_{dr} >1 dB and 40 dBZ at -15°C	0.889	0.043	0.040	0.845	0.720	0.857	0.840	10.00	7	4.5
Z_{dr} >1 dB and 40 dBZ at -20°C	0.370	0	0	0.370	0.309	0.370	0.351	3.50	4	4
Z_{dr} >4 dB and 40 dBZ at -10°C	0.667	0.174	0.182	0.493	0.467	0.581	0.485	11.00	10	6.5
Z_{dr} >4 dB and 40 dBZ at -15°C	0.259	0.043	0.125	0.216	0.181	0.250	0.203	8.50	7.5	7.5
Z_{dr} >4 dB and 40 dBZ at -20°C	0	0	0	0	0	0	0	0.00	0	0

Table 4.6   Bench mark and PID algorithm skill scores for 27 thunderstorm cases producing cloud to ground flashs and 23 non-CG storm cases from 8 case dates. Skill scores include, probability of detection (POD), probability of false alarm (PFA), false alarm ratio (FAR), true skill score (TSS), operational utility index (OUI), critical success index (CSI), Heidke skill score (HSS), and lead time (LT) mean, median and mode. The first column indicates the forecasting algorithm associated with each score set. Reference Table 3.3 for PID values.

	POD	PFA	FAR	TSS	OUI	CSI	HSS	LT Mean	LT Med.	LT Mode
40 dBZ at -10°C	1	0.522	0.308	0.478	0.608	0.692	0.497	14.00	10.5	10
Large Ice										
6<PID>9 at -10°C	1	0.478	0.289	0.522	0.626	0.710	0.541	15.00	11	6
6<PID>9 at -15°C	0.963	0.174	0.133	0.789	0.722	0.839	0.797	12.50	10.5	5
6<PID>9 at -20°C	0.926	0.174	0.138	0.752	0.691	0.806	0.757	7.00	5.5	5
Graupel										
8,9 at -10°C	1	0.478	0.289	0.522	0.626	0.710	0.541	15.00	11	6
8,9 at -15°C	0.963	0.174	0.133	0.789	0.722	0.839	0.797	12.50	10.5	5
8,9 at -20°C	0.926	0.174	0.138	0.752	0.691	0.806	0.757	7.00	5.5	5
Small Ice										
10<PID>13 at -10°C	1	1	0.460	0	0.423	0.540	0	25.50	15.5	10
10<PID>13 at -15°C	1	0.783	0.400	0.217	0.506	0.600	0.231	24.50	12	10
10<PID>13 at -20°C	1	0.652	0.357	0.348	0.556	0.643	0.365	16.00	12	10
Supercooled Drops										
7,9,14 at -10°C	0.963	0.391	0.257	0.572	0.629	0.722	0.587	15.00	11	10
7,9,14 at -15°C	0.889	0.174	0.143	0.715	0.659	0.774	0.717	10.00	9	12.5
7,9,14 at -20°C	0.704	0.130	0.136	0.573	0.520	0.633	0.564	5.50	4.5	4.5
Small and Large Ice										
6<PID>9 and 10<PID>13 at -10°C	1	0.478	0.289	0.522	0.626	0.710	0.541	15.00	11	6
6<PID>9 and 10<PID>13 at -15°C	0.963	0.174	0.133	0.789	0.722	0.839	0.797	12.50	10.5	5
6<PID>9 and 10<PID>13 at -20°C	0.926	0.174	0.138	0.752	0.691	0.806	0.757	7.00	5.5	5

4.2.4 PID

As shown in Table 4.6, the detection of small ice particles as observed in the PID has the highest average lead time of 25.5 minutes for CG onset. The modal time for this algorithm is much smaller, 10 minutes, with a median of 15.5 minutes. The mean value is biased and offset due to the occurrence of multiple secondary peaks in the lead time histogram at greater lead times. This is seen and discussed in the Appendix. The median and model are still leading values of lead time in comparison to other CG PID algorithms examined. The detection of PID small ice crystals has a 1.0 PFA. Almost any cloud existing above the freezing level, as is needed for significant electrical charging, will contain small ice particles. For accurate forecasts in operational situations, this is not a good method to utilize. Much the same as discussed in the PID section of thunderstorm forecasting, raising a false alarm too commonly can lead to failing confidence in the warning. This lack of confidence in forecasts could result in people failing to take proper precautions and could lead to serious injuries. And similarly as discussed previously, the presence of graupel PID is the dominate signature for first detection of larger ice forms. This is also seen in the data statically, as seen in Table 4.7. The detection of graupel rain mixture is also the dominate indicator for the detection of supercooled drops. The trend of comparison between the bulk category of graupel PID and supercooled drops follows the same trend in skill and lead time as found in thunderstorm forecasting.

To examine more closely the relation of the first occurrence of the PID signatures in the bulk graupel algorithm, Table 4.7 breaks down the occurrence of the PID signatures of graupel and rain mixture and graupel and small hail mixture. At -10°C graupel and small hail is detected simultaneously with graupel and rain 58% of the time,

while at -15°C graupel and small hail is the first detected signature 48% of the time. At

-20°C, graupel and rain PID is never detected, while graupel small hail signature is

dominantly the first detected at 61% of the time. The likelyhood of graupel small hail

increases with increasing height, which is likely due to the fact that the particles are more

likely to freeze at higher levels. Similarly, the opposite trend of the graupel rain mix

increasing with decreasing height is likely due to the same reason. Furthermore, hail

occurs more often at higher altitudes, which is detected at a later time than graupel at a

lower level, as can be inferred from the reduced lead time seen in Table 4.6. If a different

data set was examined in the same method, it is likely to produce different results in

statistics. Thus, it is more advantageous to group the PID categories as they have been in

this study to represent the bulk hydrometeor category. This is also a useful method to

mitigate the error that might be associated with the PID algorithm itself since it is based

on a fuzzy logic system as discussed in more details in Chapter three.

Table 4.7   Break down of percentage of the first occurrence of the hydrometeor
              categories associated with the bulk test category of graupel at each thermal
              level evaluated in this study. PID 8 is identified as Graupel and small hail
              mix. PID 9 is a mixture of graupel and rain.

	PID 8	PID 9	PID 8 and 9	Total
-10°C	12%	30%	58%	33
-15°C	48%	14%	38%	29
-20°C	61%	0%	39%	23

In comparison to the bench mark, all the PID algorithms, except the detection of

small ice forms, reduce the false alarm associated with CG forecasting. The previous

statement is also true for the increase in all skill scores, such as OUI, CSI and HSS, in

comparison to the bench mark. All of the PID algorithms examined at -10°C exceeds the

bench mark by at least one minute in average lead time, and all but the detection of

supercooled drops match the bench mark with a 100% POD. Algorithms examined at levels above -10°C have decreasing POD, from 0.96 to 0.70, however they consistently have skill, TSS, OUI, CSI and HSS, better than the bench mark. This result proves the hypothesis that the use of polarimetric variables improves first flash forecasting in comparison the benchmark, an algorithm already implemented by some forecasters.

For CG forecasting, the best algorithm implementing the use of the PID algorithm is the detection of graupel at -15°C. Even though the POD is only 0.96, lower than 1.0 POD at -10°C for the same algorithm, the skill associated is greater with an OUI of 0.72 and CSI of 0.83. The increase in skill is at the expense of two and a half minutes of mean lead time and one minute in modal time. If a forecaster is more concerned with lead times and willing to sacrifice skill accepting the greater 0.49 PFA, then the detection of the first instance of graupel by PID at a level of -10°C is the more ideal algorithm for CG forecasting.

4.2.5 Optimum CG Forecasting Technique

Overall, between all the different algorithms and results, the best for detection of hydrometeors associated with the onset of CG lightning in a thunderstorm is the detection of 40 dBZ at -15°C. The skill scores associated with this algorithm, .75 OUI and 0.87 CSI, are greater than that of the detection of graupel PID at -15°C, which has a skill of 0.72 OUI and 0.84 CSI. The POD is 1.0 for 40 dBZ at -15°C, and 0.96 for the graupel PID algorithm at -15°C. These two algorithms have identical PFA, however 40 dBZ has a slightly reduced FAR from the fact that the detection of graupel at -15°C is not indicated for a single CG cell. A comparison of the missed forecast for graupel PID and

the hit for radar reflectivity is seen in Figure 4.8. Reflectivity indicates mm-sized

particles and aided by Z_{DR} values near zero, indicates the presence of near spherical

hydrometeors, while the PID indicates dry snow. The small improvement in skill

scarifies a minute and a half in average lead time and two minutes in lead time mode. If

the operator has a greater desire for a longer lead time, then the detection of graupel

might be desirable. Even still, the results of this study prove that the use of polarimetric

variables is advantageous. Even the use of Z_{DR} proves to reduce false alarm thus

increasing skill. Z_{DR} also has the advantage of a half minute in average lead time. As

found by Zrnic et al. (2001), the PID algorithm is heavily reliant on basic horizontal

reflectivity for determination of hydrometer types as also seen in the weighting function

of the PID algorithm (not shown). Thus, it is not surprising that the lead times are not

significantly different. However, due to the advantage of processing the additional

polarimetric variables, the hypothesis was the use of the PID would significantly improve

first flash forecasting. This is supported by the results by the increase of skill, such as

CSI and OUI, due to the significant decrease of false alarm. However in general, a

decrease in false alarm was also accompanied by a decrease in POD, thus only proving a

marginal increase in skill. Furthermore, the increase of mean lead time is only marginal.

A significant increase would be found if the lead time increased by five minutes or

greater. An increase in mean lead time by 0.5 to 2 minutes is not a significant

advancement.
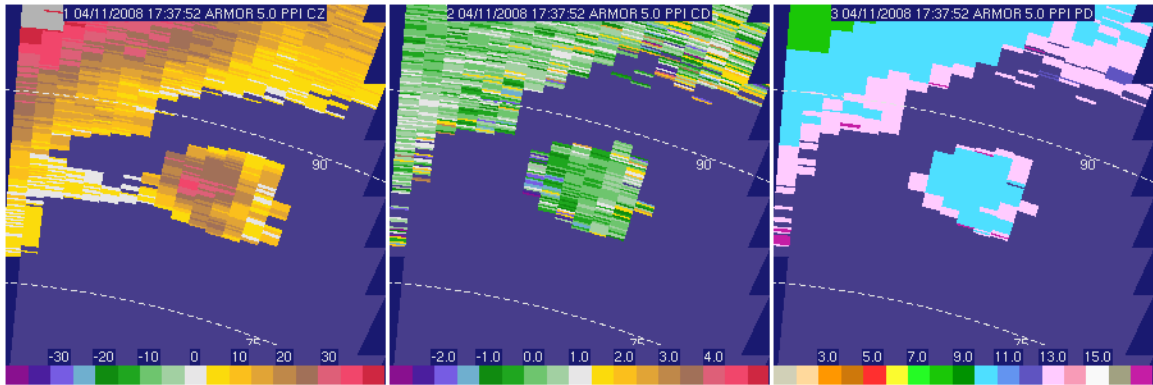
Figure 4.8   Comparison of Z_h and PID of cell 1 of 20080411 at -15°C. Radar reflectivity exceeds 40 dBZ and Z_{DR} indicates near spherical hydrometeors. PID indicates the presence of dry snow.
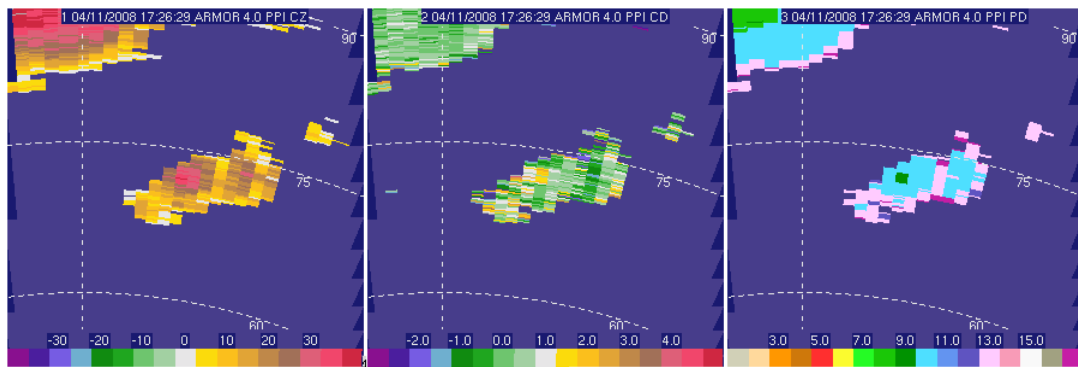
Figure 4.9   First instance of graupel PID at approximately -10°C of cell 1 case 20080411. Left to right, Z_h, Z_{DR} and PID. There was no associated "hit" forecast for Z_{DR} column due to associated Z_h values.

An instance in which the PID confirmed the location of graupel while the Z_{DR} and Z_h thresholds are not met is examined in Figure 4.9. As can be seen in the figure, there is an indication of a small region of slightly oblate drops indicated by values of > 1dB associated with the region of enhanced radar reflectivity. This is the relative region of the associated indication of graupel and rain. The Z_{DR} column algorithm fails in this case because the reflectivity threshold (> 40 dBZ) is not met. It is possible if a similar Z_{DR} column test was conducted with a reflectivity threshold of 35 dBZ that the results would be different. However, it is possible that the shift in reflectivity values would also

increase the false alarm because this would reduce the drop-size-distribution requirement to a level at which weaker updrafts, such as one associated with a non-thunderstorm, would possibly capable of meeting the criteria. This would also lead to possible error in miss representation of the hydrometeor. When comparing the use of PID to the use of Z_{DR} column, fuzzy logic PID is a more flexible algorithm which could be found more advantageous.

4.3 Comparison of CG and Thunderstorm Forecasting

As discussed previously, a CG flash is likely to occur after the first IC flash. In this data set, CG lags the first IC by an average of three and a half minutes. Four of the thunderstorm cells never produce CG flashes. In general, the best forecasting algorithm related to forecasting CG is the same as that which is the leading algorithm in forecasting thunderstorms as is related to this data set. It is seen that POD is greater and PFA is less for thunderstorm forecasting compared to CG forecasting. Thus, skill, such as CSI and OUI, related to forecasting total lightning is consistently greater than CG forecasting. This outcome is possibly an artifact of the data due to the occurrence of the four non-CG thunderstorms. These four non-CG thunderstorms contribute to the greater PFA in CG forecasting. A similar study conducted on a different, larger, data set may arrive at a different result. Generally, both CG and thunderstorm forecasting determine the same conclusion about which algorithm is more ideal, except for the instance with the detection of the first instance of graupel PID at -15°C for CG forecasting. In this case, the statistical analysis of the algorithm is very close to that of the algorithm 40 dBZ at -15°C. The difference between these algorithms is a single missed forecast by the graupel

algorithm. Otherwise, the results for forecasting CG and thunderstorms are the same. Whether forecasting for general thunderstorm threat (any lightning type) or for CG lightning flashes, the results conclusively support the hypothesis, dual-polarimetric radar is a useful tool in first flash forecasting.

CHAPTER V

SUMMARY, CONCLUSIONS, AND FUTURE WORK

5.1 Summary of Objectives and Methods

The prediction of lightning initiation is important to both air and ground

operations. Thunderstorm forecasting is relevant to operations at KSC/CCAFS and

aviation weather. CG forecasting is important for public safety at large outdoor venue

events as used by the NWS and the private weather community. CG forecasting is also

important for safety of airport and spaceport operations as forecasted by NWS and

45th WS. It has been demonstrated in the literature and in this study that the prediction of

the onset of lightning activity in a convective cloud is well correlated to radar values.

The radar values are indicative of precipitation particles supportive of the NIC

mechanism. The NIC mechanism involves the development of the tripole charge regions

in a thunderstorm by particle-to-particle interactions of large ice, such as graupel and

hail, and small ice particles. The main charging region is approximately between -10 and

-20°C. The collision and separation of the ice hydrometeors in the presence of

supercooled drops results in the exchange of charges. These charged hydrometeors are

then vertically separated by the forces of gravity and the updraft, resulting in the general

tripole structure of the thunderstorm. The accumulation of charges eventually leads to

the development of a strong electric field and the discharge of lightning.

Of the radar based lightning initiation studies conducted, none have investigated the operational utility of dual-polarimetric radar variables and first flash forecasting. The goal of this study is to develop an improved lightning initiation algorithm for use with the dual-polarimetric radar. It is hypothesized that the use of dual-polarimetric variables would lead to improvements in current techniques used, such as 40 dBZ at -10°C.

This study tested twelve different operational algorithms for forecasting lighting initiation using DP radar variables based on the NIC theory of thunderstorm electrification. Each test was evaluated at three thermal levels significant to charging mechanisms, -10, -15 and -20°C. These tests were designed to use radar variables representative of hydrometeors significant to charging such as, graupel, hail, and ice crystals and also liquid rain drops, which can subsequently freeze and participate in charging. The radar variables employed in this study included classical methods of detection using radar reflectivity at a single thermal level as well as a secondary level of 8 km as a proxy for vertical development, detection of the Z_{DR} column, and detection of bulk hydrometeors represented by output of the modified "fuzzy logic" NCAR PID algorithm. These algorithms were compared to a benchmark, 40 dBZ at -10°C to provide a bases of comparison to current radar reflectivity based forecasting algorithms in use. Development and testing of operational first flash forecasting algorithms utilizing dual-polarimetric variables has yet to be done on a scale consisting of more than a few case studies, until this study. Furthermore, this study examines the best method of forecasting both thunderstorms and specifically the first CG flash, because each type of lighting forecasting might be of interest to different communities.

These tests were conducted on data from the dual-polarimetric radar, ARMOR, located in northern Alabama.   NALMA and NLDN data were used to determine the location and time of the first flash (of any type) and the first CG flash, respectively, related to each case. NALMA and the source to flash algorithm was used in locating the first flash of a thunderstorm. NLDN data was used for its ability to detect the location of CG flashes to indicate the first occurrence as related to the cells of this case. The data of this study are comprised of eight case dates from two years, 2008 and 2010, containing thirty-one ordinary thunderstorms, twenty-seven of which produce CG flashes, and nineteen non-lightning producing storms. For each cell, an area of interest for examination was determined based upon meeting the Larsen area requirement of 30 dBZ at -10°C. This threshold is representative of mm-sized particles in the main charging region of a thunderstorm.

5.2 Results Summary, Conclusions and Future Work

It was concluded that the use of polarimetric data can improve first flash forecasting. The added information such as the relative size, shape and phase of hydrometeors as detected by the radar assists in reducing false alarm and effectively increasing skill in forecasting both CG and thunderstorm activity. The average lead time using dual-polarimetric methods, when observed at the same level, -10°C, as the bench mark, is found to increase by one minute. The POD of the benchmark is 1.0 for both thunderstorm and CG forecasting, and PFA is 0.42 and 0.52, respectively. Only a moderate skill is associated with the benchmark. Thunderstorm forecasting produces skills of 0.66 OUI and 0.79 CSI. CG forecasting results in 0.61 OUI and 0.69 CSI skills.

When examined at -10°C, Z_{DR} column forecasting produces both better skill and increased average lead time by 0.5 minutes for both lightning forecasting types. Skill of OUI and CSI increases by at least 0.02 using Z_{DR} column forecasting. PID graupel first flash forecasting also produces at least one minute gain in mean lead time and 0.02 increase in skill of OUI and CSI in comparison to the benchmark. Because of the small sample size, it is arguable as to whether these skill increases are either statistically significant or operationally meaningful. The meager increase in skill by the dual-polarimetric algorithms is due to the minor decrease of FAR. Z_{DR} column of 1 dB or greater hydrometeor forecasting has FAR values half of the benchmark FAR. Graupel PID has a marginally reduced FAR at -10°C of approximately 0.02 compared to the benchmark. DP algorithms are useful in the reduction of FAR; however, the associated lead time increase is also just as marginal as the increase in skill.

CG lightning typically occurs after the first IC lightning strike. This is seen in the data of this study in which CG has an average lead time of about three minutes more than total lightning forecasting. Comparison of CG and total lightning forecasting results in the conclusion that the best forecasting algorithms are the same for all categories of forecasting, Z_h, Z_{DR} column and PID.

The best thunderstorm and CG forecasting algorithm of all the algorithms tested in this study is 40 dBZ at -15°C. For thunderstorm forecasting, this algorithm is perfect, 1.0 POD and 0.0 PFA resulting in perfect skill as well. This is likely an artifact of the relatively small data set in this study. If the algorithms were applied to a larger data set, skill scores would likely result differently. It is likely, that even when applied to a larger data set, the use of radar reflectivity would still be a strong forecasting tool. The

associated average lead time is 8 minutes for thunderstorm forecasting and 11 for CG forecasting. For CG forecasting, 40 dBZ at -15°C produces perfect POD and only 0.17 PFA. If a margin of error in skill is allotted by the consumer for forecasting the first CG flash, then the first detection of bulk hydrometeor graupel PID is the better algorithm with an increase of average lead time by a minute and a half.   The skill of the graupel PID algorithm for CG forecasting at -15°C is 0.96 POD and 0.17 PFA. In this case, it is then the use of dual-polarimetric variables that is the better forecasting tool. For thunderstorm forecasting, graupel PID at -15°C performs with 0.93 POD and 0.05 PFA. These skill scores are less than perfect; however graupel PID does produce a greater lead time. Depending on the forecaster's needs, different algorithms were found to be to be more advantageous. Reduction of false alarm at marginal reduction to lead time is found in the use of secondary reflectivity algorithm, $Z_h > 15$ dBZ above 8 km. The associated PFA reduces by half with no increase or decrease to mean lead time. PFA is reduced to 0.21; however, the POD also reduces to 0.97. A similar result is found in CG forecasting. If the focus of the forecasting algorithm is a strong lead time, then the Z_{DR} column algorithm could be found a favorable forecasting technique. The Z_{DR} column algorithm, greater than 1 dB at -10°C, performs with the highest lead time of 11 minutes for thunderstorm forecasting and 14.5 minutes CG forecasting. The associated skills of this algorithm do not perform as well as 40 dBZ at -15°C. POD and PFA is less than perfect for thunderstorm forecasting with 0.93 and 0.16, respectively. Similarly, CG forecasting produces a skill of 0.96 POD and 0.26 PFA. For a forecaster interested in this algorithm, the increased lead time comes at the exchange of lower skill.

Through evaluation of polarimetric variables and modified PID output, it is also conclusive that the use of hydrometeor identification algorithms is a powerful tool that is still in need of further research and verification. Though the PID does not provide a significant increase in skill and lead time, they considerably decrease false alarm compared to the bench mark. It is possible with some diligent work and in situ verification of the PID output, that the algorithm could provide an even more accurate method of first flash forecasting. Possible error in this study could derive from inaccurate classification of hydrometeors by the PID due to the over lapping or improperly tuned membership functions. The membership functions could be bulked together, as conducted in this study. PID optimization might be required as well. This study examined the instance of supercooled drops as determined by PID and found that this signal is commonly classified as graupel and rain mixture. A study to further tune the PID algorithm would be advantageous if it is to be used as a primary forecasting tool. In situ confirmation of PID categories as related to radar variables could provide a more accurate result. The need to fine tune the PID algorithm is a caveat of the complexity of the algorithm. This complexity is one of the disadvantages of using DP. Other disadvantages stem from the need for data processing, such as differential attenuation correction, to get quality DP data.

As seen by the variance in conclusions of the best reflectivity based first flash algorithm of this study and previous ones, it is possible that there is variance in this due to geographical differences. The climatological differences associated with geographical location could influence the outcome for these results. Thus there might not be a widely acceptable perfect forecasting algorithm when using radar reflectivity. Instead, a separate

study for each region should be conducted to determine the best forecasting algorithm. It is possible that the use of a PID forecasting algorithm could assist in the reduction of these issues. The NIC mechanism of charge accumulation is universal. Thus, if the PID algorithm is used to determine significant hydrometeors in the climatologically located charging regions of convective storms, a general forecasting trend may be established. The PID forecasting algorithms should also be tested utilizing S-band radar to determine the best forecasting method for this radar wavelength.

It would also be advantageous to conduct a study on multicellular systems to provide a more robust conclusion. With this in mind, it is possible that conducting this test on a larger data set from a broader region may produce a result more consistent than that of radar reflectivity as has been previously studied. This would further enhance evidence of the advantages of dual-polarimetric radars to first flash forecasting. With that in mind, it should also be considered that this test be implemented on a broader data set that encompasses a wide variety of regimes, meteorological conditions, convective intensity and organization. This too may lead to different statistical conclusions due to the microphysical interactions of multicellular systems.

Due to the methodology employed in this study, there is possible human error associated with the methodology implemented. Cell selection and evaluation was all operationally conducted subjectively by the researcher to represent the process a forecasting operator would implement. An automated cell selection process is possible to increase the data set and provide a more accurate radius of interest. This process was not conducted in this study due to the desire to create a test process representative of an operational user's process of forecasting. The determination of a specific radar parameter

achieving a threshold requirement was also operationally determined. This process too is prone to human error that can be mitigated by the implementation of automated algorithms. This process would possibly require the gridding of the radar data, a choice that was once again decided against in this study for the purity of the goal in testing and determining an operational forecasting technique that could be accomplished visually by a human forecaster with real time base data.

This study was conducted to reproduce and test operational first flash forecast algorithms to discover if the use of dual-polarimetric variables increased forecast accuracy. It was found that a technique implementing the use of dual-polarimetric radar variables at a significant thermal level is useful tool in first flash forecasting. Further research in these techniques is required to support this conclusion.

LEAD TIME HISTOGRAMS, MEAN, MEDIAN AND MODE

Statistical analysis can be misleading to interpretations when examining a small data set. Outlaying maximum and minimum values can skew a numerical average if the data set is too small or the distribution of values is skewed. For example, a data set consisting of five values, 1, 6,7,6, and 22, produces a mean value of 8.4 and a mode of 6. In this case, the mode is more representative of the sample set. However, even the mode can also be misleading. For example, a data set of values, 1,7,7,22 and 22, produces a mean of 11.8 and a mode of both 7 and 22. Thus, the examination of these values should be made when considering these properties. Thus, the inclusion of lead time histograms has been included in this appendix for significant algorithms examined in the study.

Figure A.1   Lead time histogram of radar reflectivity thunderstorm forecasting. The x-axis represents the lead time value, and the y-axis is the number of cases.

Figure A.2   Lead time histogram of Z_{DR} column thunderstorm forecasting. The x-axis represents the lead time value, and the y-axis is the number of cases.
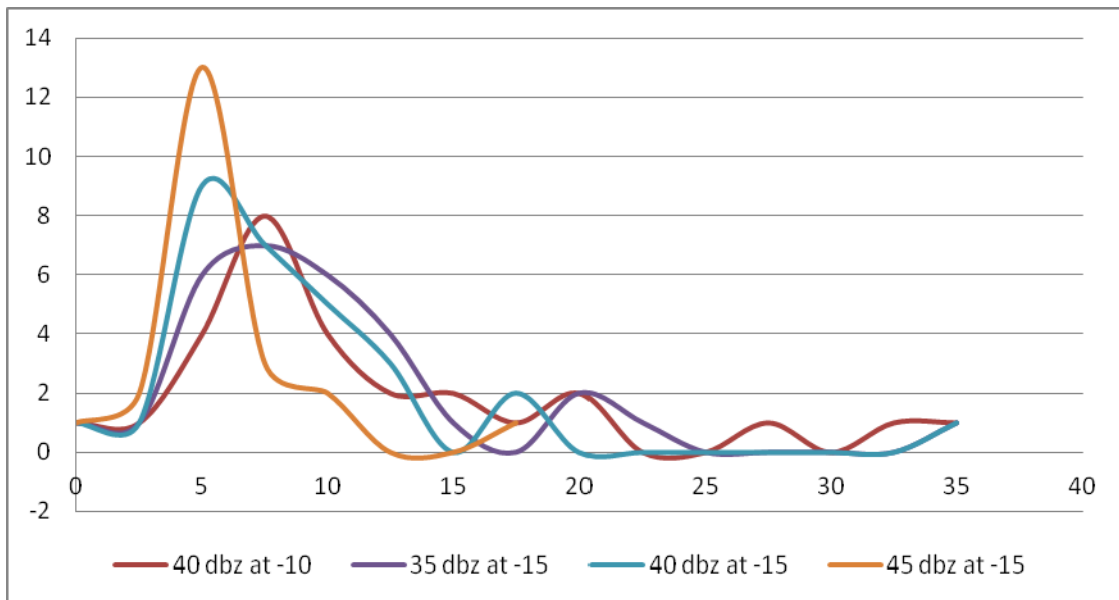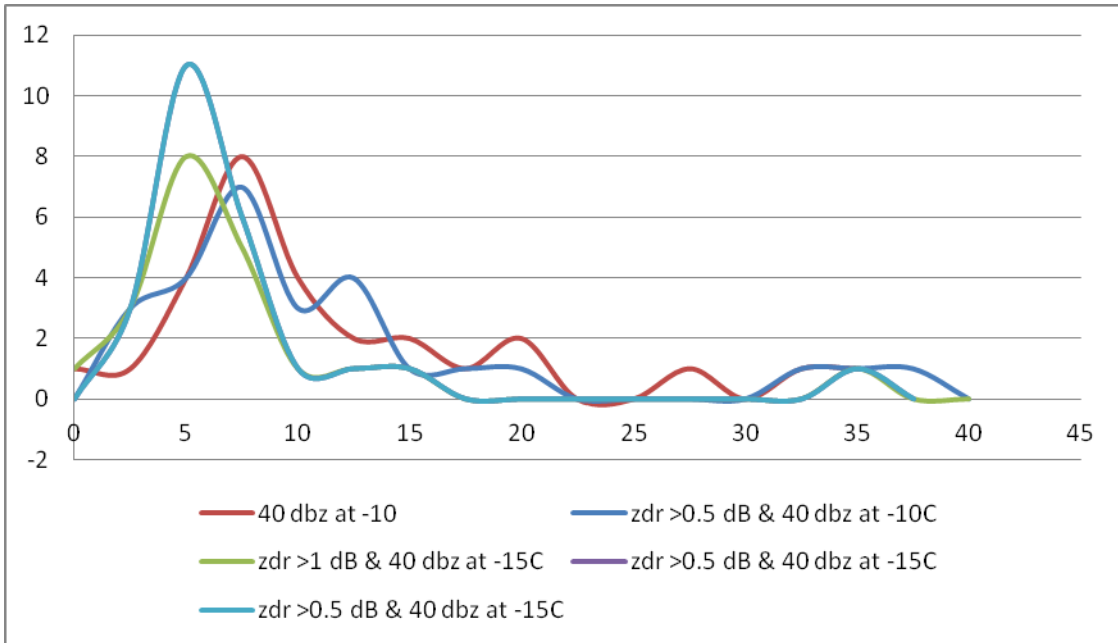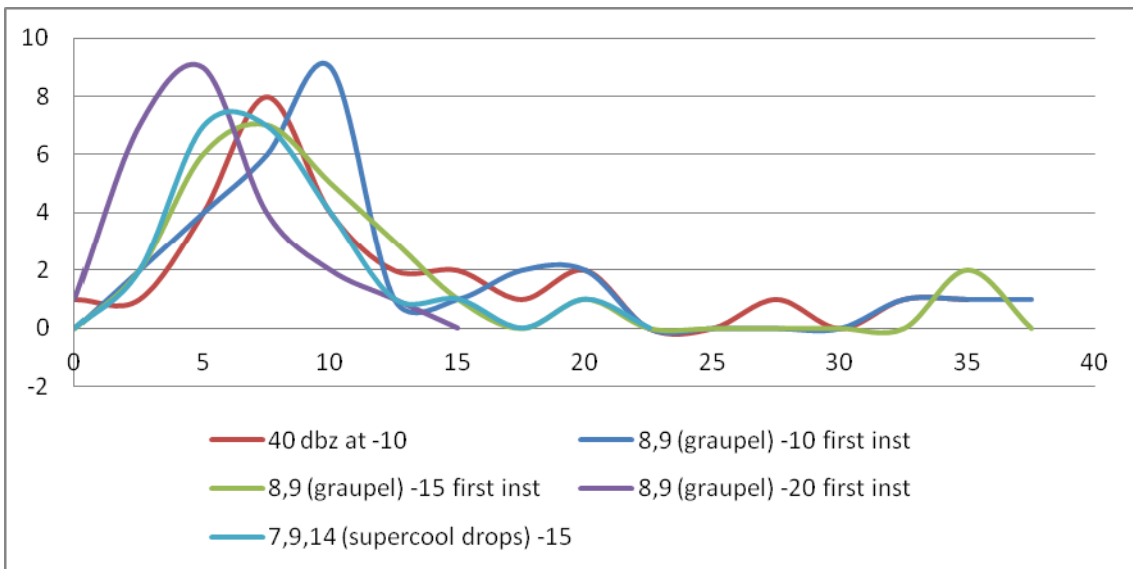

Figure A.3   Lead time histogram of PID thunderstorm forecasting. The x-axis represents the lead time value, and the y-axis is the number of cases.

As seen in Figures A.1- A.3, histogram evaluation reveals the trends of lead time values associated with each test. Previous studies discussed herein generally looked at the average lead time associated with forecasting algorithms. For that reason, the main focus of this study was on the mean lead time. Evaluating the lead time histograms reveals the trend that the benchmark has a lead time better or near the same as many of the test algorithms, such as Z_{DR} column of $Z_{DR} > 1$ dB at -15°C or $Z_h > 40$ dBZ at -15°C. The mean lead times do not perfectly match up with the median or modal lead times in this study due to the non-Gaussian nature of the histograms. This is most commonly due to the occurrence of elongated histogram tails created by outlying larger lead times. In this small data set, removal of these outlier would skew the data to be miss representative due to some cases in which there are three or more cases resulting in larger outlying lead times. For example, thunderstorm forecasting small ice PID consistently results in at least three outlying lead time values greater than 30 minutes. This offsets the mean from the median and the mode. With that in mind, the median or modal value could then be found a more ideal representation of the data. The modal data for thunderstorm forecasting could be used instead of the mean value; however, the general trend of the mode lead time is slightly more spermatic in that lead times can either increase or decrease as the forecasting requirement increases. Furthermore, when examining algorithms with fewer positive forecasts, a single modal lead time can become more difficult to determine. On the other hand, the median value can be used in exchange of the mean lead time. The mean and modal lead times follow similar trends, as can be examined in Tables 4.1- 4.3 of thunderstorm forecasting. The next paragraph will

114

examine various thunderstorm forecasting algorithm results in greater detail in respect to lead time results.

First examining the bench mark, 40 dBZ at -10°C, results in a lead time of 10.5 minutes and a median of 8 minutes. To compare the bench mark to the other leading thunderstorm forecasting algorithms, the results are still conclusively the same. 40 dBZ at -15°C has a median lead time of 6.5 minutes and a mean of 8 minutes. The difference in median lead time is the reduction of 1.5 minutes and 2.5 minutes in mean lead time. This would still result in the same conclusion that the use of 40 dBZ at -15°C is a stronger algorithm based on the marginal decrease of lead time and the associated perfect skill score. In comparison, the same goes for the determination that Z_{DR} column algorithm of 1 dB or greater at -10°C is a leading algorithm with a lead time of 11 minutes and a median of 7. In this instance, the median lead time is less than the 8 minutes of the bench mark's median lead time. Still so, in comparison of the reduced PFA associated with the algorithm, it would still be concluded to be the leading algorithm in spite of the half minute lead that Z_{DR} of 0.5 dB or greater at -10°C has with double the PFA. PID thunderstorm forecasting algorithms also produce median lead times with similar mean lead time trends. Graupel PID at -15°C median lead time follows the trend as that of the mean lead time. The graupel PID algorithm has the best skill with a median lead time of 7.5 minutes and lead time of 9.5 minutes. The lead times produce a difference of 1 minute mean lead time less compared to the bench mark and 0.5 minutes of median lead time less. If anything, this would strengthen the argument to support the utility of DP variables seeing that the difference in lead time is even more marginal. Graupel PID examined at -10°C has a greater lead of a minute in lead time when

comparing median lead times, opposed to mean lead times with a half a minute lead.

This provides further support in the utility of dual-polarimetric radar variables in

forecasting the onset of thunderstorms. Using the median as a base of lead time

evaluation drawls the same conclusions as that of mean lead time evaluation.

Figure A.4   Lead time histogram of radar reflectivity CG forecasting. The x-axis
             represents the lead time value, and the y-axis is the number of cases.

Figure A.5   Lead time histogram of Z_{DR} column CG forecasting. The x-axis represents the lead time value, and the y-axis is the number of cases.
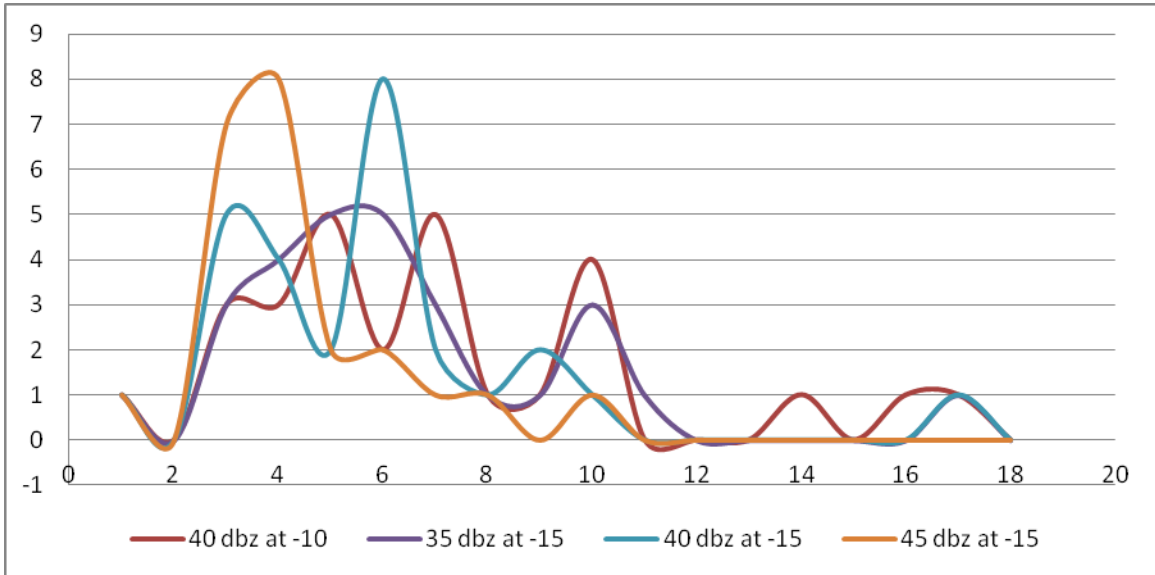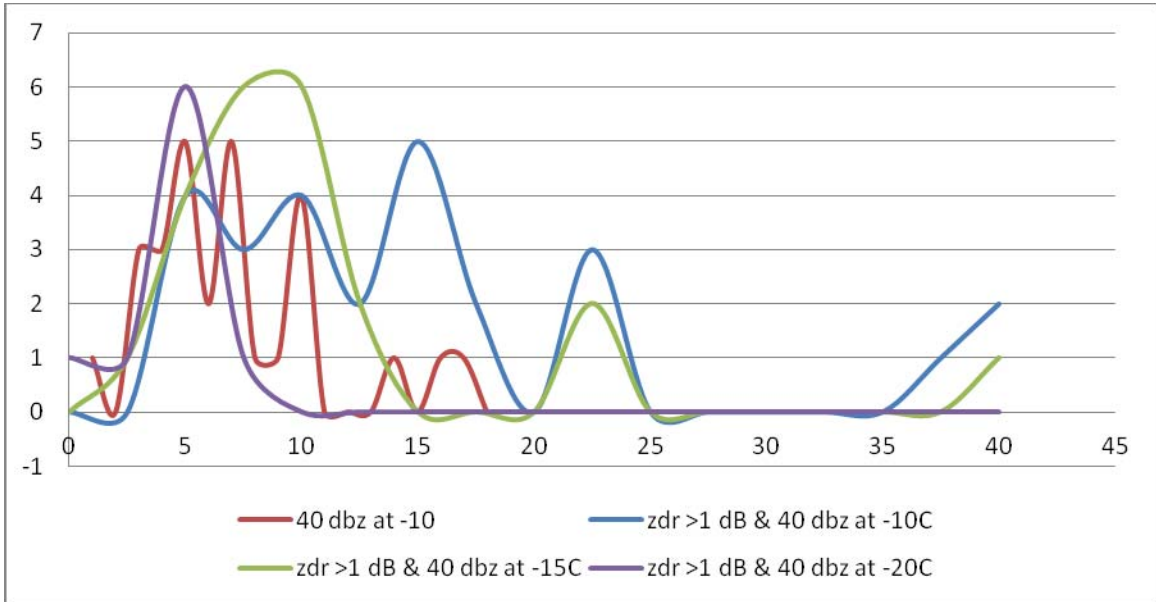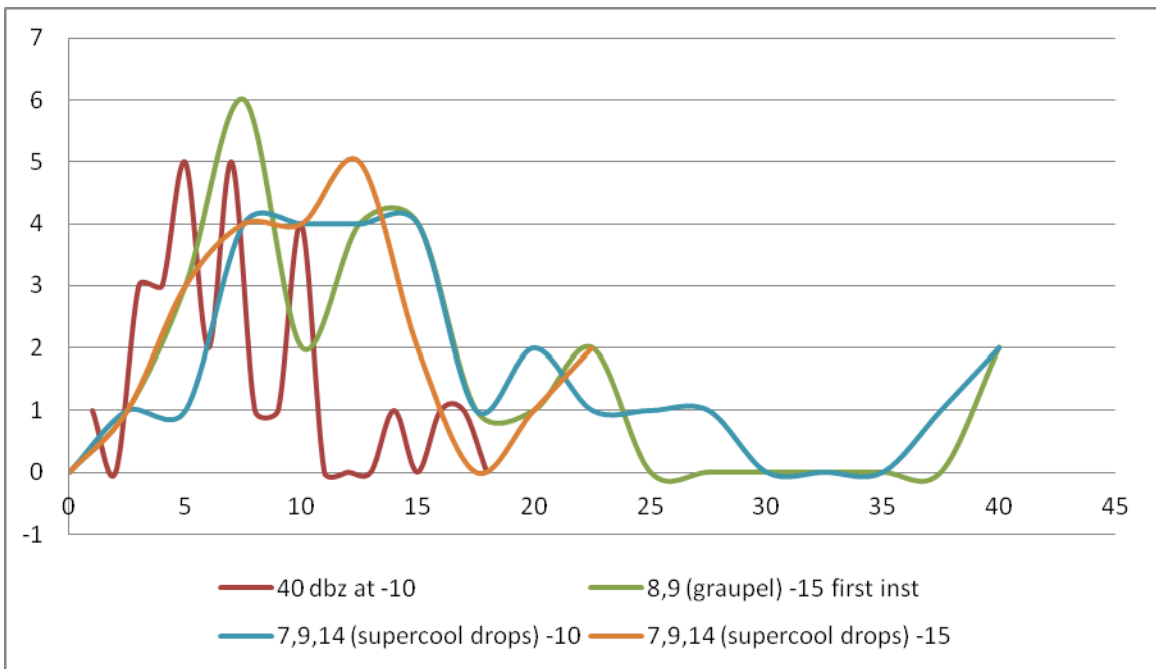

Figure A.6   Lead time histogram of PID CG forecasting. The x-axis represents the lead time value, and the y-axis is the number of cases.

Figures A.4- A.6 show the histograms of CG forecasting algorithms. The distribution of the benchmark is uneven; this is an instance in which the mode can be misleading. The long tail with secondary modal peaks offsets the mean from a normal distribution curve. More so, unlike an expected trend of naturally decreasing lead time values with increasing requirements, the bench mark modal lead time is 10 minutes. This is 4 minutes greater than that of 35 dBZ at -10°C. In general, the benchmark has a greater modal lead time than most reflectivity based forecasting algorithms. In this case the bench mark, aside from the higher PFA, would be the leading forecasting algorithm based on modal lead time alone. Z_{DR} columns of $Z_{DR} > 1$ dB at -10 and -15°C have mean lead times higher than the benchmark and modal lead times much lower, 6.5 and 4.5 minutes. This is due to the non-Gaussian form of the lead time histograms. As described previously when examining the thunderstorm histograms, multiple peaks in the histogram make determination of the modal value difficult. The sporadic nature of the modal values in this data set further provides support that the better method of evaluation may be found in median lead time evaluation.

Median lead times follow a similar trend as that of mean lead time. Comparison of algorithm median lead time results in the same conclusions as that of mean lead time examinations. The bench mark results in a mean lead time of 14 minutes and median lead time of 10.5 minutes. The best forecasting algorithm is 40 dBZ at -15°C with an 11 minute mean lead time and 10.5 median lead time. The median lead time of 40 dBZ at -15°C is identical to that of the benchmark. Combining the result of median lead time to the reduction of PFA results in the conclusion that 40 dBZ at -15°C is still the leading forecasting algorithm. The 1 dB or greater Z_{DR} column algorithm results in an increased

lead time of 0.5 minutes for both mean and median evaluation. As for PID forecasting algorithms, supercooled drops at -10°C has a histogram with a secondary modal peak near that of the first. This still produces a median lead time with a similar trend as that of the mean lead time. The supercooled drops algorithm produces a median lead time greater than the bench mark. Graupel PID at -10°C produces an identical median lead time as the bench mark. The mean lead time of graupel PID is 12.5 minutes, 1.5 minutes less than the benchmark. The resulting identical median lead time further supports the utility of DP algorithms to forecasting the first CG flash.

Histograms, median and modal lead times have been included as part of the results discussion; however, they are not a significant part of the discussion. Median lead times do not provide evidence against the utility of DP variables, nor do they provide resounding evidence supporting significant improvement to forecasting algorithms using DP variables. Thus, the mean lead time values are used primarily in the discussion and evaluation of first flash forecasting algorithms.

REFERENCES

Ahrens, C. D., 1994: *Meteorology Today: An Introduction to Weather, Climate, and the Environment.* 8th ed. West Publishing.

Anderson, M. E., L.D. Carey, K.R. Knupp, and W.A. Petersen, 2009: The ARMOR C-band radar polarimetric radar signatures of large hail: April 10, 2009 severe weather outbreak over northern Alabama. *32th Conf. on Radar Meteorology,* Williamsburg, VA.

Aydin, K., T. A. Seliga, and V. Balaji, 1986: Remote sensing of hail with a dual-linear polarization radar. *J. Climate Appl. Meteor.*, **25**, 1475–1484.

Brandes, E. A., and A. V. Ryzhkov, 2004: Hail detection with polarimetric radar. Preprints, *11th Conf. on Aviation, Range, and Aerospace Meteorology,* Hyannis, MA, Amer. Meteor. Soc., CD-ROM, P5.10.

Bringi, V. N., and V. Chandrasekar, 2001: *Polarimetric Doppler Weather Radar: Principles and Applications*. Cambridge University Press.

Bringi, V. N., K. Knupp, A. Detwiler, L. Liu, I. J. Caylor, and R. A. Black, 1997: Evolution of a Florida thunderstorm during the Convection and Precipitation/Electrification experiment: The case of 9 August 1991. *Mon. Wea. Rev.*, **125**, 2131–2160.

Bringi, V. N., T. A. Seliga, and K. Aydin, 1984: Hail detection with a differential reflectivity radar. *Science*, **225**, 1145-1157.

Bringi, V. N., T. D. Keenan, and V. Chandrasekar, 2001: Correcting C-band radar reflectivity and differential reflectivity data for rain attenuation: A self-consistent method with constraints. *IEEE Trans. Geosci. Remote Sens.*, **39**, 1906–1915.

Brooks, I. M. and C.P.R. Saunders, 1995: Thunderstorm charging: Laboratory experiments clarified. *Atmos. Res.*, **39,** 263–273.

Buechler, D. E., and S. J. Goodman, 1990: Echo size and asymmetry: Impact on NEXRAD storm identification. *J. Appl. Meteor.*, **29**, 962–969.

Byers, H. R., and R. R. Braham, 1949: *The Thunderstorm. Report of the Thunderstorm Project.* U.S. Weather Bureau, U.S. Department of Commerce Tech. Rep., 287 pp.

Carey, L. D., and S. A. Rutledge, 1996: A multiparameter radar case study of the microphysical and kinematic evolution of a lightning producing storm. *Meteor. Atmos. Phys.*, **59**, 33–64.

Carey, L. D., and S. A. Rutledge, 2000: The relationship between precipitation and lightning in tropical island convection: A C-band polarimetric radar study. *Mon. Wea. Rev.*, **128**, 2687–2710.

Carey, L. D., S. A. Rutledge, D. A. Ahijevych, and T. D. Keenan, 2000: Correcting propagation effects in C-band polarimetric radar observations of tropical convection using differential propagation phase. *J. Appl. Meteor.*, **39**, 1405-1433.

Carey, L. D., W. A. Petersen, W. Deierling, and W. P. Roeder, 2009: The new weather radar for America's space program in Florida: A temperature profile adaptive scan strategy. *34th Conference on Radar Meteorology*, 5-9 Oct 09, Paper P1.6

Christian, H. J., R. J. Blakeslee, and S. J. Goodman, 1992: Lightning Imaging Sensor (LIS) for the Earth Observing System. NASA Technical Memorandum 4350, MSFC, Huntsville, AL, Feb. 1992.

Church, C.R., 1966: The electrification of hail, Ph.D. thesis, University of Durham.

Cummins, K. L., and M. J. Murphy, 2009: An overview of lightning locating systems: History, techniques, and data uses, with an in depth look at the U.S. NLDN. *IEEE Trans. Electromag.Compat.*, **51** (3), 499–518.

D'Arcangelo, D. L., 2000: Forecasting the onset of cloud-ground lightning using layered vertically integrated liquid water, M. S. Thesis, Pennsylvania State University, 60 pp.

Deierling, W., Latham, J., W. A. Petersen, S. M. Ellis, and H. J. Christian Jr., 2005: On the relationship of thunderstorm ice hydrometeor characteristics and total lightning measurements. *Atmos. Res.*, **76**, 114-126.

Deierling, W., W. A. Petersen, J. Latham, S. Ellis, and H. J. Christian, 2008: The relationship between lightning activity and ice fluxes in thunderstorms, *J. Geophys. Res.*, **113** (D15), D15210, doi:10.1029/2007JD009700.

Dye, J. E., J. J. Jones, A. J. Weinheimer, and W. P. Winn, 1988: Observations within two regions of charge during initial thunderstorm electrification. *Quart. J. Roy. Meteor. Soc.*, **114**, 1271–1290.

Dye, J. E., J. J. Jones, W. P. Winn, T. A. Cerni, B. Gardiner, D. Lamb, R. L. Pitter, J. Hallett, and C. P. R. Saunders, 1986: Early electrification and precipitation development in a small, isolated Montana cumulonimbus. *J. Geophys. Res.*, **91**, 1231-1247.

Dye, J. E., W. P. Winn, J. J. Jones, and D. W. Breed, 1989: The electrification of New Mexico thunderstorms. Part 1: Relationship between precipitation development and the onset of electrification. *J. Geophys. Res.*, **94**, 8643–8656.

Dye, J.E., J.J. Jones, A.J. Weinheimer, and W.P. Winn, 1992: Reply to comments by C. B. Moore and B. Vonnegut: Further analysis of two regions of charge during initial thunderstorm electrification. *Quart. J. Roy. Meteor. Soc.*, **118**.

Elster, J., and H. Geitel, 1888: Über eine Methode, die elektrische Natur der atmosphärischen Niederschläge zu bestimmen (About a method for determining the electric nature of atmospheric precipitation). *Meteor. Z.,* **5***,* 95-100.

Gauthier, M. L, W. A. Petersen, L. D. Carey, and H. J. Christian, 2006: Relationship between cloud-to-ground lightning and precipitation ice mass: A radar study over Houston. *Geophys. Res. Lett.*, **33**, L20803, doi:10.1029/2006GL027244.

Goodman, S. J., and Coauthors, 2005: The North Alabama Lightning Mapping Array: Recent severe storm observations and future prospects. *Atmos. Res.,* **76**, 423-437.

Goodman, S. J., D. E. Buechler, P. D. Wright, and W. D. Rust, 1988: Lightning and precipitation history of a microburst-producing storm. *Geophys. Res. Lett.*, **15**, 1185-1188.

Gorgucci, E., G. Scarchilli, and V. Chandrasekar,1999: A procedure to calibrate multiparameter weather radar using properties of the rain medium. *IEEE Trans. Geosci. Remote Sens.*, **37**, 269–276.

Gremillion M. S., and R. E. Orville, 1999: Thunderstorm characteristics of cloud−to−ground lightning at the Kennedy Space Center, Florida: A study of lightning initiation signatures as indicated by WSR−88D. *Wea. Forecasting*, **14,** 640−649.

Hall, M. P. M., J. W. F. Goddard, and S. M. Cherry, 1984: Identification of hydrometeors and other targets by dual-polarization radar. *Radio Sci.*, **19**, 132–140.

Harris, R. J., J. R. Mecikalski, W. M. MacKenzie, P. A. Durkee, and K. E. Nielsen, 2010: The definition of GOES infrared lightning initiation interest fields. *J. Appl. Meteor. Climatol.*, **49**, 2527–2543.

Hembury, N., and R. Holle, 2011: Flash of inspiration: Latest innovations in worldwide lightning detection. *Meteor. Tech. International*, May 2011, 48-50.

Herzegh, P. H., and A. R. Jameson, 1992: Observing precipitation through dual-polarization radar measurements. *Bull. Amer. Meteor. Soc.,***73,**1365–1374.

Hitschfeld, W., and J. Bordan, 1954: Errors inherent in the radar measurements of rainfall at attenuating wavelengths. *J. Meteor*, **11,** 58–67.

Hoeth, B., D. A. Hood, M. Keehn, and M. Mosier, 2011: Vertically Integrated Ice (VII): an operational lightning forecasting tool. *5*[th] *Conference on the Meteorological Applications of Lightning Data*, Seattle, Washington.

Hondl, K. D., and M. D. Eilts, 1994: Doppler radar signatures of developing thunderstorms and their potential to indicate the onset of cloud-to-ground lightning. *Mon. Wea. Rev.*, **122**, 1818–1836. doi: 10.1175/1520-0493(1994)122<1818:DRSODT>2.0.CO;2

Jameson, A. R., M. J. Murphy, and E. P. Krider, 1996: Multiple-parameter radar observations of isolated Florida thunderstorms during the onset of electrification. *J. Appl. Meteor.,* **35,** 343–354.

Jayaratne, E. R., C. P. R. Saunders, and J. Hallett, 1983: Laboratory studies of the charging of soft-hail during ice crystal interactions. *Quart. J. Roy. Meteor. Soc*., **109**, 609–630.

Jennings, S. G., 1975: Charge separation due to water drop and cloud droplet interactions in an electric field. *Quart. J. Roy. Meteor. Soc*., **101**, 227-233.

Jolliffe, I. T., and D. B. Stephenson, 2003: *Forecast Verification: A Practitioner's Guide in Atmospheric Science*. John Wiley and Sons.

Keith, W. D., and C. P. R. Saunders. 1990: Further laboratory studies of the charging of graupel during ice crystal interactions. *Atmos. Res*., **25**, 445–464.

Koshak, W. J., and Coauthors, 2004: North Alabama Lightning Mapping Array (LMA): VHF source retrieval algorithm and error analyses. *J. Atmos. Oceanic Technol.*, **21**, 543–558.

Krehbiel, P. R., M. Brook, and R.A. McCrog, 1979: Analysis of the charge structure of lightning discharge to ground. *J. Geophys. Res.,* **84**, 2432–2456.

Krehbiel, P.R., R.J. Thomas, W. Rison, T. Hamlin, J. Harlin, and M. Davis, 2000: GPS-based mapping system reveals lightning inside storms. *EOS*, **81**, 21-25.

Larson, H. R., and E. J. Stansbury, 1974: Association of lightning flashes with precipitation cores extending to height 7 km. *J. Atmos. Terr. Phys*., **36**, 1547–1553.

Latham, J., and B. J. Mason, 1962: Electrical charging of hail pellets in a polarizing electric field. *Proc. Roy. Soc. London,* A266, 387–401.

Lhermitte, R., and P. R. Krehbiel, 1979: Doppler radar and radio observations of thunderstorms. *IEEE Trans. Geosci. Electron*., **GE-17**, 162–171.

Lim, S., V. Chandrasekar, and V. N. Bringi, 2005: Hydrometeor classification system using dual-polarization radar measurements: Model improvements and in situ verification. *IEEE Trans. Geosci. Remote Sens*., **43**, 792–801.

Liu, H., and V. Chandrasekar, 2000: Classification of hydrometeors based on polarimetric radar measurements: Development of a fuzzy logic and neurofuzzy systems, and in situ verification. *J. Atmos. Oceanic Technol*., **17**, 140–164.

Lund, N. R., D. R. MacGorman, T. J. Schuur, M. I. Biggerstaff, and W. D. Rust, 2009: Relationships between lightning location and polarimetric radar signatures in a small mesoscale convective system. *Mon. Wea. Rev*., **137,** 4151–4170.

MacGorman, D. R., I. R. Apostolakopoulos, N. R. Lund, N. W. S. Demetriades, M. J. Murphy, and P. R. Krehbiel, 2011: The timing of cloud-to-ground lightning relative to total lightning activity. *Mon. Wea. Rev*., early release, doi: 10.1175/MWR-D-11-00047.1.

MacGorman, D.R., and W.D. Rust, 1998: *The Electrical Nature of Storms*. Oxford University Press.

Marshall, J. S., and S. Radhakant, 1978: Radar precipitation maps as lightning indicators. *J. Appl. Meteor.*, **17,** 206–212.

Marshall, T. C., and W. D. Rust, 1991: Electric field soundings through thunderstorms, *J. Geophys. Res.*, **96**, 22,297 – 22,306.

Marshall, T. C., and W. P. Winn, 1982: Measurements of charged precipitation in a New Mexico thunderstorm: Lower positive charge centers. *J. Geophys. Res*., **87**, 7141-7157.

McCaul, E. W., Jr., J. Bailey, J. Hall, S. J. Goodman, R. J. Blakeslee, and D. E. Buechler, 2005: A flash clustering algorithm for North Alabama Lightning Mapping Array data. *Preprints, Conf. on Meteorological Applications of Lightning data*, San Diego, CA, Amer. Meteor. Soc., 5.2.

124

Mecikalski, J., S. Paech, K. Bedka, and W. Mackenzie, 2005: Geostationary satellite-based methods for nowcasting total lightning flash rates, convective initiation and convective cloud properties. *The World Weather Research Programmes symposium on nowcasting and very short range forecasting* (WSN05), WMOs World Weather Research Programme (WWRP), EUMETSAT and Mto-France, Toulouse, France, Oral presentation 2.22

Michimoto, K., 1991: A study of radar echoes and their relationship to lightning discharge of thunderclouds in the Hokuriku District. Part I: Observation and analysis of thunderclouds in summer and winter. *J. Meteor. Soc. Japan*, **69,** 327–335.

Mosier, R. M., C. Schumacher, R. E. Orville, and L. D. Carey, 2011: Radar nowcasting of cloud-to-ground lightning over Houston, Texas. *Wea. Forecasting*, **26**, 199–212.

Murphy, M. J., K. L. Cummins, N. W. S. Demetriades, and W. P. Roeder, 2008: Performance of the new Four Dimensional Lightning Surveillance System (4DLSS) at the Kennedy Space Center/Cape Canaveral Air Force Station Complex. *13th Conference on Aviation, Range, and Aerospace Meteorology*, 18 pp.

NASA, cited 2011: The U.S. National Lightning Detection Network Database (NLDN). [http://gcmd.nasa.gov/records/GCMD_NLDN.html].

National Climate and Data Center, cited 2011: Annual mean number of days with measurable precipitation. [http://hurricane.ncdc.noaa.gov/climaps/prec2613.pdf].

National Weather Service, cited 2010: Natural Hazard Statistics. [http://www.nws.noaa.gov/om/hazstats.shtml].

National Weather Service, cited 2010: Natural Hazard Statistics. [http://www.weather.gov/os/hazstats.shtml].

National Weather Service, cited 2011a: Thunderstorms: Introduction. [http://www.srh.noaa.gov/jetstream//tstorms/tstorms_intro.htm].

National Weather Service, cited 2011b: Natural Hazard Statistics. [http://www.nws.noaa.gov/om/hazstats.shtml].

National Weather Service, cited 2011c: 70-years. [http://www.nws.noaa.gov/om/hazstats/images/70-years.pdf].

NOAA and NASA, 2011: Goes-R: Geostationary Lightning Mapper (GLM). [http://www.goes-r.gov/spacesegment/glm.html].

Petersen, W. A., K. Knupp, J. Walters, W. Deierling, M. Gauthier, B. Dolan, J. P. Dice, D. Satterfield, C. Davis, R. Blakeslee, S. Goodman, S. Podgorny, J. Hall, M. Budge, and A. Wooten, 2005: The UAH-NSSTC/WHNT ARMOR C-Band dual polarimetric radar: A unique collaboration in research, education, and technology transfer. Preprints, *32nd Conference on Radar Meteorology*, Albuquerque, N. M.

Petersen, W. A., K. R. Knupp, D. J. Cecil, and J. R. Mecikalsi, 2007: The University of Alabama Huntsville THOR Center instrumentation: Research and operational collaboration. *33rd International Conference on Radar Meteorology*, American Meteorological Society, Cairns, Australia.

Petersen, W. A., R. C. Cifelli, S. A. Rutledge, B. S. Ferrier, and B. F. Smull, 1999: Shipborne dual-doppler operations during TOGA COARE: Integrated observations of storm kinematics and electrification. *Bull. Amer. Meteor. Soc*, **80,** 81–97.

Petersen, W. A., S. A. Rutledge, and R. E. Orville, 1996: Cloud-to-ground lightning observations from TOGA COARE: Selected results and lightning location algorithms. *Mon. Wea. Rev.*, **124**, 602–620.

Proctor, D. E., 1971: A hyperbolic system for obtaining VHF radio pictures of lightning. *J. Geophys. Res.*, **76**, 1478 – 1489.

Reynolds, S E., and M. Brook, 1956: Correlation of the initial electric field and the radar echo in thunderstorms. *J. Meteor.*, **13,** 376–380.

Reynolds, S. E., M. Brook, and M. F. Gourley, 1957: Thunderstorm charge separation. *J. Met*, **14**, 426–436.

Rinehart, R. E., 2010: Radar for Meteorologists. 5th ed. Rinehart.

Roeder, W. P., and C. S. Pinder, 1998: Lightning forecasting empirical techniques for central Florida in support of America's space program. *16th Conference On Weather Analysis And Forecasting*, 475-477

Roeder, W. P., and T. M. McNamara, 2011: Using temperature layered VIL as automated lightning warning guidance. *5th Conference on Meteorological Applications of Lightning Data*, Seattle, WA, Paper 688, 10 pp.

Roeder, W. P., T. M. McNamara, B. F. Boyd, and F. J. Merceret, 2009: The new weather radar for America's space program in Florida: An overview. *34th Conference on Radar Meteorology*, Paper 10B.6.

Roeder, W. P., T. M. McNamara, B. F. Boyd, J. W. Weems, and S. B. Cocks, 2005: Unique uses of weather radar for space launch. *32nd Conference on Radar Meteorology*, 13 pp.

Rutledge, S. A., and W. A. Petersen, 1994: Vertical radar reflectivity structure and cloud-to-ground lightning in the stratiform region of MCSs: Further evidence for in situ charging in the stratiform region. *Mon. Wea. Rev.*, **122**, 1760–1776.

Rutledge, S. A., E. R. Williams, and T. D. Keenan, 1992: The Down Under Doppler and Electricity Experiment (DUNDEE): Overview and preliminary results. *Bull. Amer. Meteor. Soc.,* **73,** 3–16.

Ryzhkov, A. V., 2007: The impact of beam broadening on the quality of radar polarimetric data. *J. Atmos. Oceanic Technol.*, **24**, 729–744.

Ryzhkov, A. V., S. E. Giangrande, V. M. Melnikov, and T. J. Schuur, 2005: Calibration issues of dual-polarization radar measurements. *J. Atmos. Ocean. Tech.*, **22,** 1138-1155.

Saunders, C. P. R., 1993: A review of thunderstorm electrification processes. *J. Appl. Meteorol.*, **32**, 642-655.

Saunders, C. P. R., W. D. Keith, and R. P. Mitzeva, 1991: The effect of liquid water on thunderstorm charging. *J. Geophys. Res*, **96,** 11007–11017.

Scharfenberg, K., P. T. Schlatter, and D. J. Miller, 2004: The use of the "ZDR column" signature in short-term thunderstorm forecasts. *11th Conf. on Av. Range and Aerospace Metor.*, Hyannis, MA, Amer. Meteor. Soc., P5.5.

Simpson, G. C., and F.J. Scrase, 1937: The distribution of electricity in thunderclouds. *Proc. Roy. Soc. A*, **161**, pp. 309–352.

Simpson, Sir G., and G.D. Robinson, 1941: The distribution of electricity in thunderclouds, II. *Proc. Roy. Soc. Lond., A,* **177***,* 281-328.

Smith, P., 1984: Equivalent radar reflectivity factor for snow and ice particles. *J. Climate Appl. Meteor.,* **23,** 1258–1260.

Straka, J. M., and D. S. Zrnic, 1993: An algorithm to deduce hydrometeor types and contents from multiparameter radar data. Preprints, *26th Int. Conf. on Radar Meteorology*, Norman, OK., Amer. Meteor. Soc., 513-516.

Straka, J. M., D. S. Zrnic, and A. V. Ryzhkov, 2000: Bulk hydrometeor classification and quantification using polarimetric radar data: Synthesis of relations. *J. Appl. Meteor.*, **39,** 1341–1372.

Takahashi, T., 1978: Riming electrification as a charge generation mechanism in thunderstorms. *J. Atmos. Sci*, **35,** 1536–1548.

Testud, J., E. L. Bouar, E. Obligis, and M. Ali-Mehenni, 2000: The rain profiling algorithm applied to polarimetric weather radar. *J. Atmos. Oceanic Technol.*, **17**, 322-356.

Thomas, R. J., P. R. Krehbiel, W. Rison, S. J. Hunyady, W. P. Winn, T. Hamlin, and J. Harlin , 2004: Accuracy of the Lightning Mapping Array. *J. Geophys. Res*., **109**, D14207, doi:10.1029/2004JD004549.

Uman, M.A, 1987: *The lightning discharge*. Orlando, Florida: Academic Press Inc.

Vincent, B.R, L.D. Carey, D. Schneider, K. Keeter, and R. Gonski, 2003: Using WSR-88D reflectivity data for the prediction of cloud-to-ground lightning: A North Carolina study. *Nat. Wea. Digest*, **27**, 35-44.

Vivekanandan, J., D. S. Zrnic, S. M. Ellis, R. Oye, A. V. Ryzhkov, and J. Straka, 1999: Cloud microphysics retrieval using S-band dual-polarization radar measurements. *Bull. Amer. Meteor. Soc*., **80**, 381–388.

Wallace, J. M., and P. V. Hobbs, 2006: *Atmospheric Science: an introductory survey*. Academic Press, San Diego, CA, second edition.

Weems, J. W., C. S. Pinder, W. P. Roeder, and B. F. Boyd, 2001: Lightning watch and warning support to spacelift operations. *18th Conference on Weather Analysis and Forecasting*, 301-305.

Williams, E. R., 1989: The tripole structure of thunderstorms. *J. Geophys. Res*., **94**, 13151–13167.

Williams, E.R., M. E. Webber, and R. E. Orville, 1989b: The relationship between lightning type and convective state of thunderclouds. *J. Geophys. Res*., **94**, 13213–13220.

Wolf, P., 2006: Anticipating the initiation, cessation, and frequency of cloud-to-ground lightning, utilizing WSR-88D reflectivity data. *NWA Electronic Journal of Operational Meteorology*, December 2006.

Workman, E. J., and S. E. Reynolds, 1949: Electrical activity as related to thunderstorm cell growth. *Bull. Amer. Meteor. Soc*.,**30**, 142–144.

Yang, Y.H., and P. King, 2010: Investigating the potential of using radar echo reflectivity to nowcast cloud-to-ground lightning initiation over southern Ontario. *Weather and Forecasting,* **25**:4, 1235-1248.

Zeng, Z., S. E. Yuter, R. A. Houze Jr., and D. E. Kingsmill, 2001: Microphysics of the rapid development of heavy convective precipitation. *Mon. Wea. Rev*, **129,** 1882–1904.

Ziegler, C. L., and D. R. MacGorman, 1994: Observed lightning morphology relative to modeled space charge and electric field distributions in a tornadic storm*. J. Atmos. Sci*., **51**, 833–851.

Zipser, E. J., and K. Lutz, 1994: The vertical profile of radar reflectivity of convective cells: A strong indicator of storm intensity and lightning probability? *Mon. Wea. Rev.*, **122**, 1751–1759.

Zrnic, D. S., A. V. Ryzhkov, J. M. Straka, Y. Liu, and J. Vivekanandan, 2001: Testing a procedure for automatic classification hydrometeor types. *J. Atmos. Oceanic Technol*., **18**, 892–913.

Zrnic, D. S., and A. V. Ryzhkov, 1996: Advantages of rain measurements using specific differential phase. *J. Atmos. Oceanic Technol*., **13**, 454–464.

Zrnic, D. S., T. Keenan, L. D. Carey, and P. May, 2000: Sensitivity analysis of polarimetric variables at a 5-cm wavelength in rain. *J. Appl. Meteor*., **39**, 1514–1526.